Università degli Studi di Catania
Scuola Superiore di Catania

International PhD
in
Nanoscience
XXIV cycle

Fabrication and characterisation of ZnO nanostructures: from nanoscale building blocks to hybrid nanomaterials – towards emerging technologies in sensing applications

Yana Aleeva

Coordinator of PhD
Prof. M.G. Grimaldi

Tutor
Dr. M.E. Fragalà

a.a. 2008/2011

To my grandparents

Abstract

Metal oxide nanostructures characterized by multiple morphologies and structures are at the forefront of applications driven nanotechnology research. In particular, they represent a versatile solution for performance enhancement and applications in multifunctional devices and offer distinct advantages over their bulk counterparts.

The current state in ZnO nanomaterials research and its impact in nanotechnology and modern engineering are discussed through the lens of continuing technological advances in synthetic techniques allowing to obtain the material with predefined specific set of criteria including size, functionality, and uniqueness.

Aim of this research activity is fabrication and study of the potential applications as biomolecular nanoplatforms of ZnO nanostructures obtained using different synthetic techniques ranging from vapor phase deposition (Metal-Organic Chemical Vapor Deposition) to solution growth (Chemical Bath Deposition). Moreover, hybrid synthetic approaches are used to obtain complex hierarchical ZnO structures having dual or multiple morphologies. The non-covalent interaction of these inorganic nanosystems with organic molecules, having specific chemical behavior, represents a strategy to obtain hybrid organic-inorganic nanomaterials, thus offering interesting potentiality for the design of high performance devices. In particular, it is demonstrated that integration of Metal-Organic Chemical Vapor Deposition and Chemical Bath Deposition strategies with Nanosphere Colloidal Lithography allows to define two-dimensional hybrid ZnO-SiO_2 nanoarrays having great potential as innovative fluorescence sensing substrates with individual addressability and tuning of the biomolecular detection capability.

Combination of Metal-Organic Chemical Vapor Deposition with Electrospinning leads to fabrication of core–shell Zn-doped TiO_2–ZnO nanofibers characterised by hierarchical growth of ZnO nanoneedles onto the TiO_2 nanofiber surface. XRD measurements revealed that after ZnO deposition at $T > 500$ °C, the TiO_2 nanofibers were composed of the anatase–rutile mixed phases with different fractions of rutile, modulated by the Zn dopant concentration. These composite nanomaterials may be intriguing to the future study of nanofiber photocatalysts and sensors, and functional properties based on titanium dioxide.

Keywords: Zinc oxide, MOCVD, Chemical Bath Deposition, Electrospinning, Nanosphere Colloidal Lithography, nanorods, FRAP, sensing, protein immobilization.

Contents

1. Introduction

1.1 Introduction

Nowadays, nanotechnology represents, with no doubts, a multinational priority and key direction of development supported by government policy of many countries all over the world [1]. It opens a door to tailoring materials and creating various nanostructures for use in various spheres of life, i.e. sensing [2-4], catalysis [5-7] and energy storage devices [8].

The concept of nanotechnology was first introduced by Prof. R. Feynman in 1959, when he expressed an idea - ‘‘to synthesize nanoscale building blocks with precisely controlled size and composition, and assemble them into larger structures with unique properties and functions’ [9]. Almost 40 years later, in 1998 Neal Lane, Assistant to USA President for Science and Technology stated “If I were asked for an area of science and engineering that will most likely produce the breakthroughs of tomorrow, I would point to nanoscale science and engineering” [10].

The actual converging technology philosophy, pointing at the manipulation of matter on the nanometer (10^{-9} m) scale, will deliver tremendous results. It is expected that converging technologies will bring along outstanding improvements in transforming tools, providing new products and services, enabling human personal abilities and social achievements, and reshaping societal relationships.

In general, the term “nanotechnology” [11] refers to the

- “Research and technology development at the atomic, molecular or macromolecular levels, in the length scale of approximately 1 - 100 nanometer range.
- Creating and using structures, devices and systems that have novel properties and functions because of their small and/or intermediate size.
- Ability to control or manipulate on the atomic scale.”

Nanotechnology is also a multi-disciplinary field that links together the advances of physics, engineering, molecular biology, and chemistry. Fabrication of nanostructures in a controlled way is a challenge for the development of nanoscience and nanotechnology. Controlled growth of hierarchical structures of inorganic materials opens a brand new field to not only nanomaterials synthesis but also to their applications in a variety of fields such as field emission, photovoltaics, supercapacitors, catalysts, sensors, high strength and multifunctional nanocomposites etc. [12-16].

The properties and performances of these new nanomaterials are mainly controlled by their nature, size and morphology. The nanoscale size may also affect the quantum confinement effect [17] and optical confinement [18] which enabled nanomaterials to have received considerable attention and been extensively investigated for applications in electronic, optoelectronic, photovoltaic, photocatalytic and sensing devices [19]. Metal-oxide nanostructures are ideal systems for exploring a large number of novel phenomena at the nanoscale and investigating size and dimensionality dependence of nanostructure properties for potential applications [20].

Sensing is another topic that becomes increasingly hot over the past decade. A sensor is a device, which is composed of an active sensing material with a signal transducer, allowing to transmit the signal without any amplification from a selective compound or from a change in a reaction [21]. These devices produce any one of the signals as electrical, thermal or optical output signals which could be converted into digital signals for further processing.

One of the main challenges in sensing engineering is the selection and development of an active material. The key requirement of active sensing materials is to act as a catalyst for sensing a particular analyte or a set of analytes. The recent development in the nanotechnology has paved the way for large number of new materials and devices of desirable properties which have useful functions for numerous electrochemical sensor and biosensor applications [21]. In general, accurate tailoring of nanostructured material makes it possible to control the fundamental properties of materials (on nanoscale level) remaining their chemical composition without changes. In this sense, the low dimensional systems became extremely attractive, and together with the current tendencies on the fabrication of functional nanostructured arrays could play a key role in the new trends of nanotechnology [22]. As mentioned before, nanostructures can be used for both efficient transport of electrons and optical excitation, and these two factors make them critical to the function and integration of nanoscale devices [19]. In fact, nanosystems are the smallest dimension structures that can be used for efficient transport of electrons and are thus critical to the function and integration of these nanoscale devices. Because of their high surface-to-volume ratio and tunable electron transport properties due to quantum confinement effect, their electrical properties are strongly influenced by minor perturbations [21].

Nanomaterials are advantageous in providing large surface area. Among all the nanomaterials, semiconductors occupy a central position due to the advantages they offer in terms of synthesis and manipulation.

ZnO, TiO_2, SnO_2, SiC and GaN are interesting semiconductors widely used in many field such as photovoltaic, gas sensing, catalysis, photonic and biological applications and thus the controlled fabrication of nanostructures is strongly desired [23-29]. In particular, ZnO is a unique material characterised by excellent semiconducting and piezoelectric properties combined with an excellent thermal and chemical stability and novel applications of this functional material are expected to be demonstrated in the near future [30]. Moreover, ZnO is probably the only widely studied metal oxide having the richest family of nanostructures among all materials, both in structures and properties. Growth of high quality ZnO nanowire arrays and knowledge of their physical properties are fundamental for their applications as sensors [31-33], field emitters [34-35], light-emitting diodes [36-39], photocatalysts [40,41], nanogenerators and nanopiezotronics [42,43].

So what makes ZnO one of the most prominent semiconductors in the metal-oxide family? First of all, it has a wide-band-gap of 3.37 eV and a large exciton binding energy of 60 meV. This ensures efficient excitonic ultraviolet (UV) emission at room temperature. Besides, the non-central symmetry of ZnO in wurtzite structure, combined with its large electromechanical coupling, results in strong piezoelectric and pyroelectrical properties and implies a consequent usage in actuators, piezoelectric sensors and nanogenerators. Zinc oxide is also bio-safe, biocompatible, and can be directly used for biomedical applications without coatings. As for one-dimensional (1D) ZnO nanostructures, they play the key roles in developing nanoscience and nanotechnology, as illustrated by many articles published. It is fair to state that ZnO 1D nanostructures are probably the most important metal-oxide-semiconductor 1D nanostructures in nowadays research [44].

Growing interest in the synthesis of ZnO nanostructures is stimulated due to promising applications in nanoscale technologies and devices. The motivation of this work originates in the applications of ZnO in potential bio- and chemical sensing devices, dye-sensitized solar cells, optoelectronic devices, and so on, for which ZnO is well suited.

This work aims to demonstrate how specific tailoring of ZnO nanostructures via different synthetic routes is closely related to properties and therefore to the performance of the obtained material.

Aim of the research is the fabrication and characterization of high surface area inorganic and hybrid inorganic/organic materials exploring their potential applications in the actual converging technologies such as sensing and optical appliances.

The electronic, optical and piezoelectric properties of ZnO nano/microstructures are largely dependent on their composition, crystal structure, dimension, and morphology. In particular, low-dimensional ZnO structures with controlled morphology offer great potential in efficient assembly of nanoscale devices.

Different approaches are explored in this work, including Metal-Organic Chemical Vapor Deposition (MOCVD) and Chemical Bath Deposition (CBD) in order to design different ZnO material (thin films, nanorods, nanowires) and control the location, orientation, distribution, and uniformity of nanostacks. The obtained materials are analyzed using a complete structural, morphological and optical characterization.

The deposition approach is altered depending on desired size of the resulting material. Particular attention is devoted to deposition temperature. The actual technologies, moving towards flexible and molecular electronics, need a further decrease of deposition temperature to satisfy process integration requirements. In this perspective the conventional chemical vapor deposition (CVD) approach will find an intrinsic limitation. In this sense, chemical bath deposition, which is versatile and bio-safe technique, represents a good alternative to CVD. Indeed, liquid phase deposition of materials allows the adoption of the low-cost and high-throughput patterning technologies used in the printing industry to solar cell production. Template assisted growth represents an alternative to above mentioned methods of manipulating the building blocks into a regular form for future advanced nanodevices. Various lithographic techniques, including photolithography, electron beam lithography, interference lithography, nanosphere lithography, nano-imprint lithography, micro-contact printing, and inkjet printing, are employed to control the spatial distribution of ZnO nanowires on a substrate. Nanosphere colloidal lithography (NSCL) is a bottom – up strategy which allows to design ordered arrays of the predefined shape. It offers a simple, cost-effective, and high throughput lithographical approach.

Electrospinning (ES) can be another interesting approach to shrink the size of materials features into the range of nanometers. This technique utilizes an electric field for producing non-woven fibers. It has been shown to produce “one-dimensional’’ shapes including fibers, ribbons, filled and hollow tubes, all having large specific surface areas. The electroceramic nanofibers represent the building blocks for applications at the nanoscale such as gas sensors, piezoelectric tubing for nanofluidics, and catalysts.

Herein, both NSCL and ES were merged with MOCVD or CBD approaches in order to allow the formation of porous nanopatterned arrays and hierarchical core-shell nanostructures respectively. Subsequently, the characterization methods used to study morphology, structure and optical properties are discussed.

1.2 Aim of the research

Current state of research revealed that ZnO nanostructures are equally important to carbon nanotubes and SiC nanostructures for nanotechnology. ZnO nanostructures have found application in a wide variety of areas ranging from bio- and chemical sensors to dye-sensitized solar cells. In these perspectives, the controlled synthesis of ZnO nanostructures having high surface area is a key factor for the design of high performance devices.

The present research work has involved a series of issues in attempt to advance the understanding of the following challenges in ZnO nanostructures:

- Structural, morphological and dimensionally controlled synthesis of ZnO nanostructures;
- Design of low-temperature growth of ZnO in order to get high quality reproducible material compatible with wide range of substrates and easily integrated with current device technologies;
- Large-scale, low-cost, patterned, and designed growth via bottom-up lithographic and electrospinning techniques;
- Structural, morphological and optical characterisation of as grown nanoarchitectures;
- Study of fluorescence recovery behaviour as a proof of concept of biological sensing.

1.3 Thesis organization

This dissertation comprises 9 chapters. The motivation and the current challenges for ZnO nanostructures research are briefly reviewed in Chapter 1.

With the generation of new devices, one has to understand and control the morphology of ZnO. This thesis is focused mainly on controlled fabrication and characterization of high surface area ZnO materials having various morphology, e.g. thin films, nanorods, nanowires and hierarchical core-shell nanostructures (see Fig. 1.1), providing enhancement of surface area of ZnO.

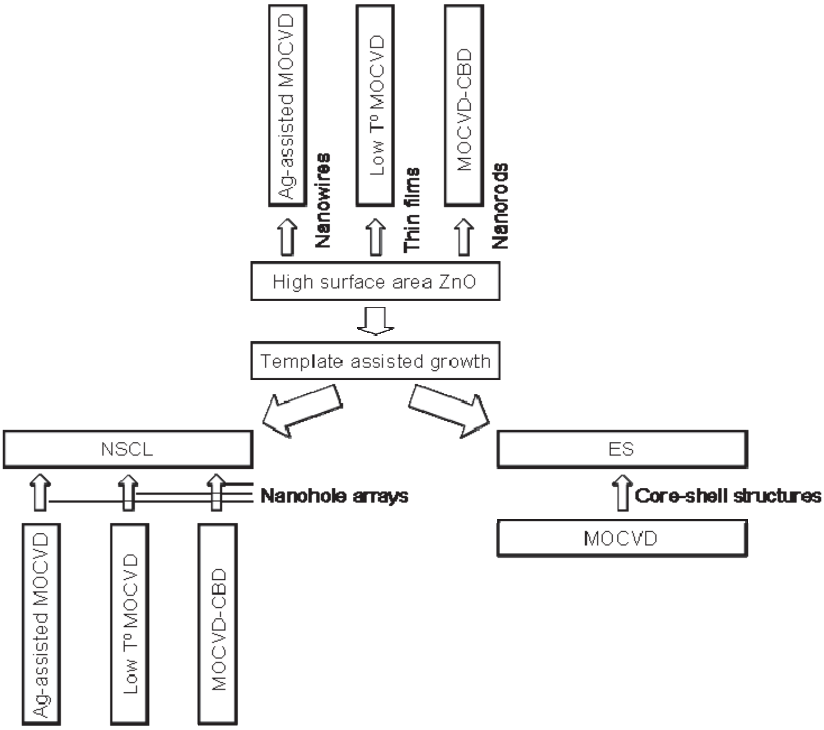

Figure 1.1: Scheme of deposition techniques applied in the present work

In Chapter 2 of this dissertation, a brief account of the current state-of-the-art in the area of history in zinc oxide research and properties of ZnO nanostructures are presented. Furthermore, the trends in ZnO synthetic methods are discussed using data currently available in the literature. Finally, based on current achievements in design and tailoring of properties and structure of ZnO, the latest advances in applications are reviewed in detail.

Chapter 3 of this dissertation focuses on the synthetic methods used to grow nanostrtuctures. Aside from the methods such as metal-organic chemical vapor deposition and chemical bath deposition, commonly used in ZnO growth, electrospinning and nanosphere colloidal lithography are presented. NSCL forming a polymeric template on surface allows to obtain patterning on the substrate. Electrospinning is employed in assistance to create fibers which are used for the growth of hierarchical nanostructures. Subsequently, characterization methods used to study morphology, structure and optical properties are discussed.

Chapter 4 establishes the choice of metal organic precursor used in this work for MOCVD deposition of ZnO. Moreover, it demonstrates the morphology resulting from deposition in the high temperature range. The role of deposition time and temperature is discussed in terms of the two-dimensional (continuous grain-like film) to one-dimensional (nanorods) evolution.

Chapter 5 covers the catalyst-assisted growth of ZnO films in the temperature range 300 - 600 ^{o}C. Ag catalyst was chosen as an alternative to commonly used catalysts as Au, Pt or Pd. Accurate tailoring of thin film growth conditions is discussed. The temperature range is attributed to the choice of catalyst to avoid unwanted oxidating leading to poor quality nanowires. Besides the general MOCVD growth parameters such as growth temperature and time, as well as catalyst concentration is also found to be critical for the ZnO growth [45]. Moreover, catalyst-assisted MOCVD growth on templates formed via NSCL in order to grow hexagonally patterned ZnO thin films is reported. A complete set up of optimal process conditions for an effective nanosphere colloidal lithography/catalyst assisted MOCVD process integration is presented. It mainly focuses on the determination of the deposition temperature threshold for ZnO MOCVD growth as well as the concentration of metal-organic silver (Ag) catalyst. Indeed, the optimization of such process parameters allows to tailor the ZnO film morphology in order to make the colloidal lithography/catalyst assisted MOCVD approach a valuable bottom up method to fabricate bi-dimensional ordered ZnO nanohole arrays [46].

Chapter 6 focuses on the low-temperature (< 400 ^{o}C) growth of ZnO thin films catalyst-free MOCVD method. Their full characterization in terms of structure is provided. MOCVD deposition below 300 ^{o}C yielded slow growth rate and poor deposition efficiency. Indeed, growth at such low temperatures is critical and hard to control. Longer growth times, however, allowed formation of smoother films and good coverage. Furthermore, successful integration of

NSCL-MOCVD approach for ZnO nanohole arrays fabrication is demonstrated. Moreover, as grown films have been studied in terms of sensitivity to model analyte proteins. Accordingly, it is suggested that protein mobility on the nanostructured ZnO film is strongly affected by topography of as deposited films. Thus, mobility is inhibited due to an enhanced friction resulting from the molecules moving inside the pore rims. On the other hand, the protein molecules which are freely moving around the laterally homogeneous ZnO substrates will experience a higher effective diffusion [47].

In Chapter 7 of this dissertation, chemical bath deposition of ZnO nanostructures as a low temperature (< 100 ^{o}C) alternative to MOCVD is discussed. Although wet chemical approaches have attracted more recent attention in ZnO research, the mechanism and role of growth parameters are still a matter of study. The current efforts are particularly devoted to the study of the ligand concentration and seed role in formation of high-quality ZnO nano-arrays. To do so, buffer layers are deposited by temperature reducing (< 200 ^{o}C) of drop-casted Zn^{2+} salts and MOCVD-grown ZnO layers at various temperature (300 - 600 ^{o}C). The growth is conducted in solution employing amine-based precursors. Ligand concentration appears to strongly affect the alignment of ZnO nanorods on the substrate, their lateral dimension and the related surface density. Length and diameter of ZnO nanorods increase upon increasing the ligand concentration, while the nanorod density decreases. Whereas, the structure and thickness of the seed layer strongly influences the final morphology and the crystal texturing of ZnO nanorods as well as the CBD growth rate. There is, in addition, a strong correlation between morphologies of CBD grown ZnO nanorods and those of the seed layer underneath. Thus, nanorods grown on drop-casted seed layers and the ones deposited over low temperature MOCVD buffer layers are less homogeneous in lateral dimensions and poorly vertically oriented. On the contrary, higher temperature nano-dimensional ZnO seeds favor the CBD growth of almost mono-dimensional homologue nanorods, with an adequate control of the lateral transport of matter [48,49]. The nanorod aspect ratio values decrease upon increasing the deposition temperatures of the seed layers. Furthermore, the current advances in low temperature solution growth of structured arrays via three step MOCVD-NSCL-CBD approach are presented. X-ray photoelectron spectroscopy (XPS) characterization suggested that patterned arrays are more hydrophilic due to the presence of polar moieties. The obtained ZnO nanoarrays appeared to be promising in sensing of proteins [50]. Successful fluorescence enhancement has been achieved. It is shown that protein exhibits reduced mobility due to high porosity and surface polarity.

Chapter 8, in turn is focused on fabrication of hierarchical ZnO nanostructures allowing drastically increase surface-to-volume ratio. In this chapter, combined electrospinning - MOCVD approach is employed to fabricate TiO_2 core nanofibers shelled with ZnO nanostrtuctures [51]. The effect of Zn doping is studied, therefore TiO_2 fibers are characterized before and after ZnO depositon. It is shown, that at current deposition conditions (600 ^{o}C) Zn - dopant initiated TiO_2 anatase - rutile transition confirmed by XRD data. The structural and optical properties of ZnO-TiO_2 core-shell nanostrtuctures were comprehensively characterized. The amount of doping and deposition time plays an important role in morphology of as grown nanoarchitectures. Thus, nanostructure with small rounded ZnO grains are observed for Zn doping < 5%, while high doping and longer deposition time (90 min) yields ZnO nanonedlees hierarchical structures. The particularly favorable surface-to-volume ratio, due in turn to the large density of ZnO single crystalline nanorods/nanoneedles on the shell surface, promotes a remarkable cathodoluminescence emission in the UV and green regions.

Finally, a separate conclusion is presented in Chapter 9, the last chapter of this dissertation.

References

1. Nanoscience and nanotechnologies: opportunities and uncertainties. The Royal Society and The Royal Academy of Engineering (2004) 116.
2. W. P.Tai and J.H.Oh, Sens. Actuators, B 85 (2002) 154-157.
3. A. Kolmakov and M.Moskovits, Ann. Rev. Mater. Res. 34 (2004) 151-180.
4. E. Comini, Anal. Chim. Acta 588 (2006) 28-40.
5. H.H. Kung and M.C. Kung, Catal. Today 97 (2004) 219-224.
6. B. Zhou, S. Hermans, G.A. Somorjai (Eds.), Nanotechnology in Catalysis, V.1-2, Springer, 2004, 555p.
7. B. Zhou, S. Han, R. Raja, G.A. Somorjai (Eds.), Nanotechnology in Catalysis, V. 3, Springer, 2007, 368p.
8. A.S. Arico, P. Bruce, B. Scrosati, J.-M. Tarascon and W.V. Schalkwijk, Nat.Mater. 4 (2005) 366-377.
9. R.P. Feynman, Caltech Eng. Sci. 23 (1960) 22-36.

10. M.C. Roco, R.S. Williams, P. Alivisators, Nanotechnology research directions: Interagency working Group on Nanoscience, Engineering and Technology (IWGN) Workshop report, Kluwer, Dordrecht, 2000.
11. U.S. Environmental Protection Agency Nanotechnology White Paper.
12. Y. Zhang, C.-T. Lee, J. Phys. Chem. C 113 (2009) 5920-5923.
13. F.Yang, M. Shtein, S.R.Forrest, Nat. Mater. 4 (2005) 37-41.
14. E. Frackowiak, K.Metenier, V. Bertagna, F. Beguin, Appl. Phys. Lett. 77 (2000) 2421-2423.
15. S. Sun; F. Jaouen, J.-P. Dodelet, Adv. Mater. 20 (2008) 3900-3904.
16. J.Y.Lao, J.G.Wen, and Z.F.Ren, Nano Lett. 2 (2002) 1287-1291.
17. Z.H.Lu, D.J. Lockwood, J.M. Baribeau, Nature 378 (1995) 258-260.
18. M. Rajalakshmi, A.K. Agora, B.S. Bendre and S. Mahamuni, J. Appl. Phys. 87 (2000) 2445-2448.
19. Q. Zhang, G. Cao, Nano Today 6 (2011) 91-109.
20. T. Zhai, X. Fang, M.Liao, X.Xu, H.Zeng, B.Yoshio, D.Goldberg, Sensors 9 (2009) 6504-6529.
21. U. Yogeswaran and S.-M. Chen, Sensors 8 (2008) 290-313.
22. M. Hernandez-Velez, Thin Solid Films 495 (2006) 51-63.
23. Y.Zhang, J.Q. Xu, Q. Xiang, H.Li, Q.Y. Pan and P.C. Xu, J. Phys. Chem. C 113 (2009) 3430-3435.
24. W.W. Wang, Y.J.Zhu, L.X. Yang, Adv.Funct. Mater. 17 (2007) 56-64.
25. X.X. Li, Y.J. Xiong, Z.Q. Li, Y. Xie, Inorg. Chem 45 (2006) 3493-3495.
26. H. Choi, A.C. Sofranco, D.D. Dionysiou, Adv. Funct. Mater. 16 (2006) 1067-1074.
27. Q. Dong, H.L. Su. D. Zhang, F.Y. Zhang, Nanotechnology 17 (2006) 39689-3972.
28. G.H. Shen, Y.Bando, D. Golberg, Cryst. Growth Des. 7 (2007) 35-38.
29. J.S. Pearton, J.C. Zolper, R.J. Shul, F.Ren, J. Appl. Phys. 86 (1999) 1-78.
30. J.S. Pearton, D.P. Norton, K. Ip, Y.W. Heo, T. Steiner, Progress Mater. Sci. 50 (2005) 293-340.
31. P. Mitra, A.P. Chatterjee, H.S. Maiti, Mater. Lett. 35 (1998) 33-38.
32. Q. Wan, Q.H. Li, Y.J. Chen, T.H. Wang, X.L. He, J.P. Li, C.L. Lin, Appl. Phys. Lett. 84 (2004) 3654-3656.
33. X.D. Wang, J.Zhou, J.H. Song, J.Liu, N.S. Xu, Z.L. Wang, Nano Lett. 6 (2006) 2768-2772.
34. Y.B. Li, Y. Bando, D. Golberg, Appl. Phys. Lett. 84 (2004) 3603-3605.

35. R.C. Wang, C. P. Liu, J.L. Huang, S.J. Chen, Y.K. Tseng, S.C. Kung, Appl. Phys. Lett. 87 (2005) 013110.
36. A. Tsukazaki, A. Ohtomo, T. Onuma, M. Ohtani, T.Makino, M. Sumiya, K. Ohtani, S.F. Chichibu, S. Fuke, Y. Segawa, H. Ohno, H. Koinuma, M. Kawasaki, Nat. Mater. 4 (2005) 42-46.
37. Y.I. Alivov, J.E. van Nostrand, D.C. Look, M.V. Chukichev, B.M. Ataev, Appl.
Phys. Lett. 83 (2003) 2943-2945.
38. A. Tsukasaki, M. Kubota, A. Ohtomo, T. Onuma, K. Ohtani, H.Ohno, S.F. Chichibu, M. Kawasaki, Jap. J. Appl. Phys. P.2 Lett. Express Lett 44 (2005) 20-23.
39. J.M. Bao, M.A. Zimmler, F.Capasso, X.W. Wang, Z.F. Ren, Nano Lett. 6 (2006) 1718-1722.
40. R. Georgekutty, M.K. Seery, S.C. Pillai, J.Phys. Chem C. 112 (2008) 13563-13570.
41. Q. Zhang, W. Fan, L. Gao, Appl. Cat. B. Environm. 76 (2007) 168-173.
42. Z.L. Wang, R.Yang, Y.Qin, C.Xu, Y.Hu, S. Xu, Mat. Sci. Eng. R 70 (2010) 320-329.
43. Z.L. Wang, Nano Today 5 (2010) 540-552.
44. T. Zhai, X. Fang, M. Liao, X. Xu, H. Zeng, B. Yoshio, D. Goldberg, Sensors 9 (2009) 6504-6529.
45. M.E.Fragala, C.Satriano, and G.Malandrino, Chem. Commun. (2009) 839-841.
46. M.E.Fragala’, C.Satriano, Y.Aleeva, G. Malandrino, Thin Solid Films 518 (2010) 4484-4488.
47. C. Satriano, M. Fragala’, Y.Aleeva, J. Col. Interf. Sci. 365 (2012) 90-96.
48. M.E.Fragala’, Y.Aleeva, G.Malandrino, Superlattices Microstruct. 48 (2010) 408-415.
49. M.E.Fragala, Y.Aleeva, G.Malandrino, Thin Solid Films 519 (2011) 7694-7701.
50. M.E.Fragala, Y.Aleeva, C.Satriano, J. Nanosci. Nanotechnol. 11 (2011) 1-5.
51. M.E.Fragala’, I.Cacciotti, Y.Aleeva, R. Lo Nigro, A. Bianco, G. Malandrino, C. Spinella, G. Pezzotti and G.Gusmano, CrystEngComm. 12 (2010) 3858-3865

2. State of the art

2.1 Introduction

This Chapter aims to demonstrate the current state in technology in ZnO research covering ZnO properties, synthetic techniques and applications. Device performance is closely related to the structure of ZnO nanomaterial, which in turn determines the properties. Therefore, a rational design of the nanostructures may lead to optimal conductivity and electron transport. Aside from the surface modification the fabrication of ZnO nanostructures is a direct way of improving the efficiency of optoelectronic and sensing devices, the tailoring of materials for a defined purpose is herein emphasized to be an important way of speeding up the development nanotechnology progress.

2.2 History of ZnO research

ZnO is playing an increasingly key role in developing Nanoscience and Nanotechnology because of its remarkable performance in electronics, optics, photonics and sensing such as protein selectivity, photocatalysis and gas sensing [1]. Figure 2.1 represents a bar chart of the last 20 years of the number of published papers (source ISI Web of Knowledge, Topic: Zinc Oxide) related to zinc oxide. Over the abovementioned period the number of publications has increased more than 17 times and keeps growing with more recent reviews published [2-6]. It is fair to state that carbon nanotubes, silicon nanowires, and ZnO nanostructures are probably the most important nanomaterials in today's research.

The first studies focusing on ZnO date back several decades when in 1935 the lattice parameters were determined [7]. Like most other wide band gap semiconductors, synthesis of ZnO thin films has been an active field because of their applications as sensors, transducers and catalysts in the late 1950s - 1960s when the extensive study of optical, electrical and structural properties of semiconducting ZnO was conducted [8]. The actual renaissance of research and growth of this material has been started in the past decade mostly attributed to the outstanding piezoelectric, optoelectronic and biocompatible properties and numerous application possibilities, especially since the study of one–dimensional (1D) materials has become a leading edge in nanoscience and nanotechnology.

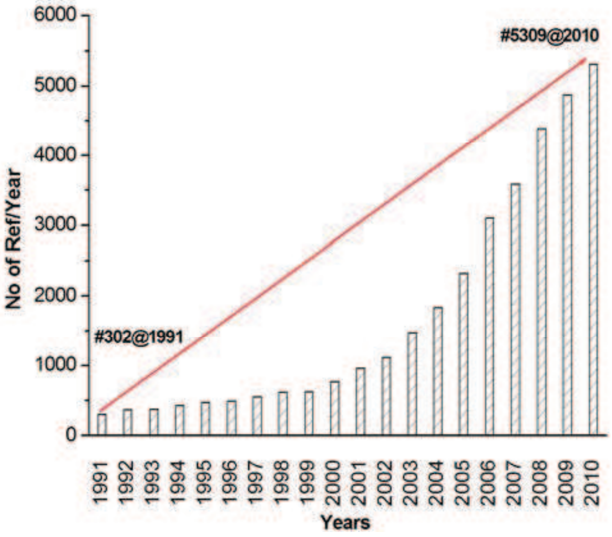

Figure 2.1: Number of ZnO related papers published by year (Source ISI Web of knowledge)

2.3 ZnO structure

Zinc oxide is an oxidic compound which exists in nature as a rare mineral called zincite having red or orangy color due to manganese impurities [2]. The ZnO crystal structure is determined by the tetrahedraly coordinated bonding geometry. The crystal structure of ZnO may vary (zinc-blende-type, hexagonal-wurtzite-type and rocksalt structure) and depends on the arrangement of the bilayers formed by neighbouring tetrahedrons consisting of zinc and oxygen layers [3,4].

Under ambient conditions, the thermodynamically stable crystal structure is the hexagonal wurtzite $P6_3mc$ with a large anisotropic property in c-axis direction and perpendicular to the c-axis. The wurtzite structure is favoured over the other phases due to high bond polarity. The considerably high degree of polarity is caused by the very strong (3.5) electronegativity of the oxygen which together with the quite low (0.91) zinc electronegativity value leads to an ionicity of 0.616 on the Philips scale [9].

A schematic representation of wurtzite structure is shown in Fig. 2.2. Simply, the Zn^{2+} cations and O^{2-} anions are tetrahedrally coordinated and the centers of the positive ions and negatives ions overlap with each other. The crystal exhibits partial polar characteristics with lattice parameters a = 0.3296 and c = 0.5207 nm [10]. The crystal lacks of center symmetry, which is the core of piezoelectricity due to the intrinsic crystallographic structure.

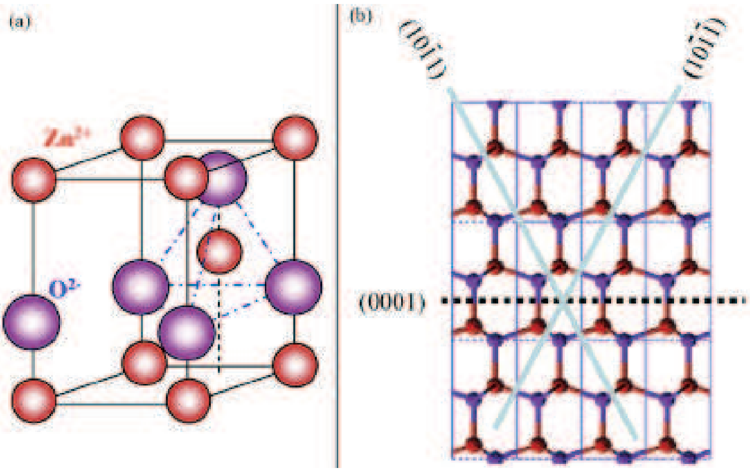

Figure 2.2: (a) Wurtzite structure model of ZnO, (b) The three types of facets of ZnO nanostructures (Reprinted from [10])

Zinc oxide crystal exhibits several typical surface orientations. The most important surfaces are the basal planes - (0001) and $(000\bar{1})$, prism planes - $(10\bar{1}0)$ and $(11\bar{2}0)$ and pyramidal plane $(11\bar{2}1)$. Another important characteristic of ZnO is polar surfaces. The most common polar surface is the basal plane (0001). One end of the basal polar plane terminates with partially positive Zn lattice sites and the other end terminates in partially negative oxygen lattice sites. The oppositely charged ions produce positively charged Zn - (0001) and negatively charged O - $(000\bar{1})$ surfaces, resulting in a normal dipole moment and spontaneous polarization along the c-axis as well as a variance in surface energy. Additionaly, these surfaces are found to be atomically flat, stable and exhibit no reconstruction [11, 12]. The other two most commonly observed facets for ZnO are $(2\bar{1}\bar{1}0)$ and $(01\bar{1}0)$, which are non-polar and have lower energy than the (0001) facets [10].

2.4 Properties of ZnO nanostructures

Fundamental understanding of the physical properties of the material is important for technological advances. Due to the diversity in morphologies and structures of ZnO the properties of individual nanostructures can have large variations. ZnO nanorods and nanowires are important because of their unique structural one-dimensionality and possible quantum confinement effects in two dimensions. They can possess novel electronic and optical properties, piezoelectric and pyroelectric properties which make them good candidates for applications in room-temperature ultraviolet (UV) lasers, field-effect transistors, photodetectors and photocatalysts, gas sensors, transducers, energy generators and solar cells (Fig. 2.3) [10]. In addition, magnetic and electrical properties can be modified by intentionally introducing impurities into the lattice. ZnO is also a "green" material that is biocompatible, biodegradable, and non-toxic for medical applications and environmental science [13].

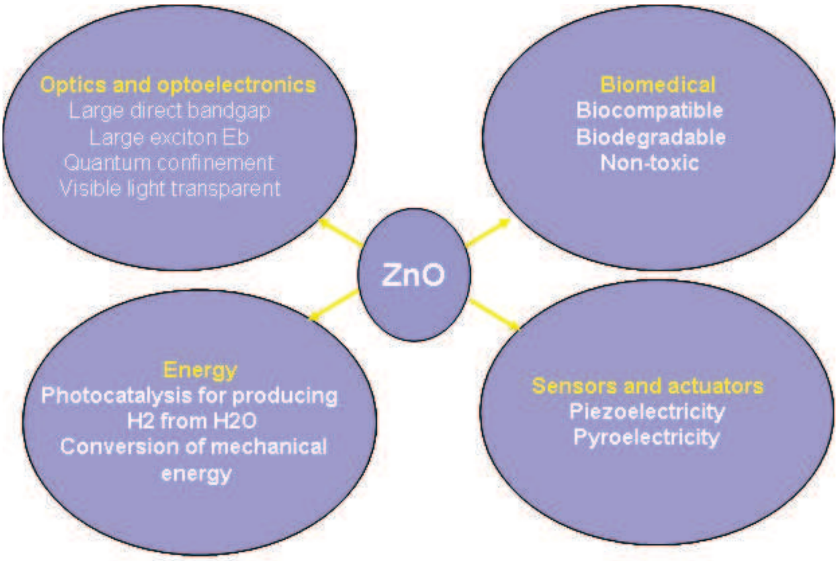

Figure 2.3: A summary of applications and properties of ZnO [10]

ZnO is a wide band gap (3.37 eV at 300 K) semiconductor with high electron hole- binding energy (60 meV) and an exciton Bohr radius in the range of 1.4-3.5 nm [14]. Basic physical parameters of ZnO and other commonly used semiconductors are presented in Table 2.1.

Table 2.1: General properties of commonly used semiconductors

Properties	ZnO	GaN	TiO_2	SnO_2
Density , g/cm3	5.61	6.15	4.23	6.95
Melting point, K	2248	2500	1843	1630
Relative dielectric constant	8.66	8.9	8.43	9.86
Gap Energy, eV	3.37	3.4	3.75	3.6
Exciton binding energy, meV	60	25	N/A	130

2.4.1 Optical properties

Optical properties of one-dimensional ZnO are important for many of their technological applications in photonic devices, LED and lasers [15-17]. Notably, ZnO has a large exciton binding energy of 60 meV, which is more than twice that of GaN (25 meV) and much greater than thermal energies at room temperature (25 meV), and high optical gain of 300 cm^{-1} (100 cm^{-1} for GaN) at room temperature [18-21]. This allows ZnO to provide stable band-edge ultra-violet (UV) emission at room temperature via an exciton recombination process as opposed to the significantly less efficient electron–hole plasma process employed in current GaN - based devices [22].

In general, ZnO shows five types of luminescence emissions [23-31]:

- Near band edge emission at around 390 nm (UV emission), attributed to free-exciton recombination;
- Blue emission at around 460 nm is because of intrinsic defects such as oxygen and zinc interstitials;
- Green emission at around 540 nm is known to be a deep level emission which is caused by impurities, a structural defects in the crystal such as oxygen vacancies, zinc interstitials, etc.;
- Yellow emission which is associated with excess oxygen;
- Red emission at around 630 nm - 680 nm due to oxygen and zinc antisites.

Therefore, the optical properties depend critically on microstructure, texture, and surface morphology, on the presence of defects which in turn depends on the deposition method, doping and surface modification.

Song et al. studied the effect of pH at hydrothermal growth of ZnO nanorods on the photoluminescence properties [31]. Fig. 2.5 shows that ZnO nanorods, synthesized at a lower pH=10.6, had a higher UV emission (I_{UV}) and a lower deep-level emission (I_{DLE}) peak. I_{UV}/I_{DLE} ratio was 1.24 and 0.18 for the ZnO nanorods synthesized at a pH of 10.6 and 13.0, respectively. XPS study suggested that such phenomena is due to oxygen deficiencies and can also be related to the fact that lower pH led to larger nanorod formation which in turn are less influenced by imperfect boundaries and stacking faults [31, 32].

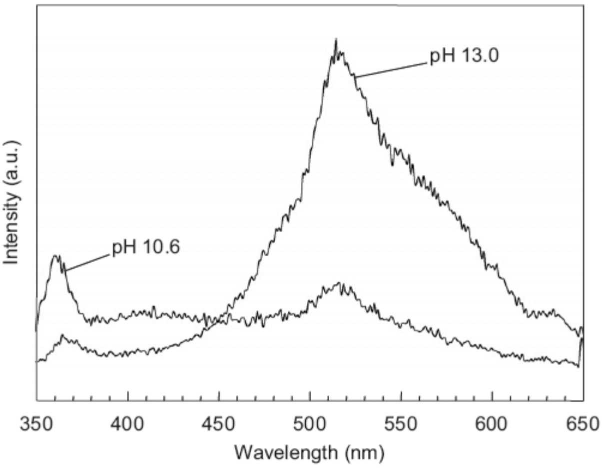

Figure 2.5: PL spectra of ZnO nanorods synthesized in the solutions with pH of 10.6 and 13.0 using zinc sulfate as a precursor (Reprinted from [31])

Singh et al. showed that surface modification of ZnO nanoparticles with various capping agents (triethanolamine and thioglycerol) has a strong effect on photoluminescence [33]. It shows that PL intensity is higher when thioglycerol is used as surfactant due to the formation of smaller ZnO nanoparticles as compared to TEA. However, no blue shift has been observed in photoluminescence spectra due to size effect as the PL emission generally comes from the ZnO nanocrystals, and the blue shift in the optical absorption spectra is due to the amorphous phase in the material [34].

The technical progress made in synthesis (bulk and nano) and epitaxial growth of thin films and the results indicate the possibility of realizing both n-type and p-type conduction in ZnO [3-6]. Making p-type ZnO is still a challenge and remains an intriguing issue. The domains of interest for compounds based on ZnO and associated heterostructures are optoelectronics and spintronics. It is obvious that there is high potential for ZnO in optoelectronic applications of

ZnO with respect to some of the competing compound semiconductors such as ZnS, GaAs, ZnSe. This also gives strong resistance to high temperature electronic degradation during operation (e.g. laser diodes). ZnO is transparent to visible light and can be made highly conductive by doping [35].

2.4.2 ZnO piezoelectric properties

Piezoelectricity is an intrinsic property of ZnO. An origin of piezoelectricity lies in its crystal structure, in which zinc atoms and oxygen atoms are tetrahedrally bonded. ZnO wurtzite crystal has a hexagonal structure with a large anisotropic property in *c*-axis direction and perpendicular to the *c*-axis. The crystal lacks of center symmetry, which is the core of piezoelectricity due to the intrinsic crystallographic structure. Therefore, the crystal shows no polarization under strain-free condition. If a stress is applied at an apex of the tetrahedron, the center of the cations and the center of anions are relatively displaced, resulting in a dipole moment (Fig. 2.6). A constructive adds up of the dipole moments created by all of the units in the crystal results in a macroscopic potential drop along the straining direction in the crystal. This is the piezoelectric potential (*piezopotential*) (Fig. 2.6). The piezopotential, an inner potential in the crystal, is created by the non-mobile, non-annihilative ionic charges, the piezopotential remains in the crystal as long as the stress remains. The magnitude of the piezopotential depends on the density of doping and the strain applied [36].

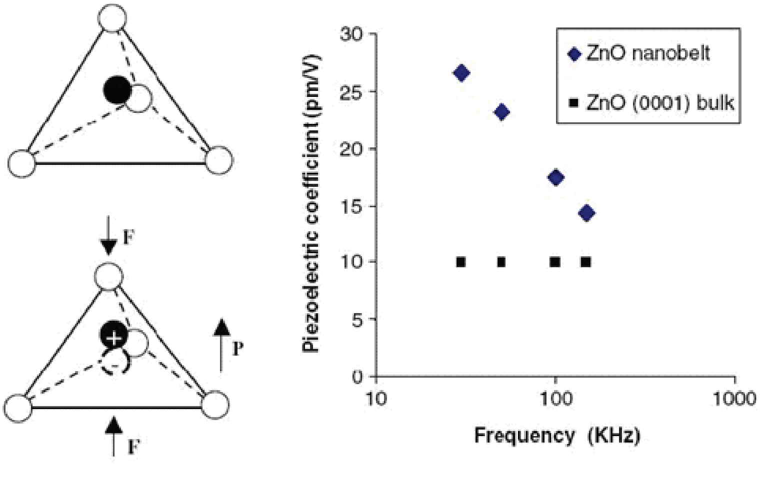

Figure 2.6: Piezopotential in wurtzite crystal. (Reprinted from [36])

Corso et al. demonstrated that ZnO piezoelectric effect results from two different contributions of opposite sign, which are reffered to as the “clamped ion” and “internal strain” [37]. Low value of clamped ion is responsible for the large piezoelectric tensor of ZnO, which is also affected by the internal relaxation of anion and cation sublattices induced by the macroscopic strain. The theoretically calculated piezoelectric coefficient for ZnO ε_{33}=0.89 C/m^2 is quite close to the experimentally measured value of ε_{33}=1.0-1.2 C/m^2 [38]. In fact, among the terahedrally bonded semiconductors, ZnO has the highest piezoelectric tensor which provide a large electro-mechanical coupling [39].

The magnitude of the piezoelectric effect depends on the growth direction and morphology of the material. Thus, thin films have lower piezoelectric tensor value than one-dimensional nanostructures. The most desirable morphology to maximize the piezoelectric effect is to create nanostructures that preserve large area (0001) polar surfaces [37]. Atomic force microscopy with conductive tips was applied to measure the piezoelectric coefficient of ZnO nanobelts [39]. Nanobelts of ZnO were deposited on a conductive Si substrate covered with the 100 nm layer of Pd. The effective piezoelectric coefficient of ZnO nanobelt was found to be frequency dependent and varied from 14.3 pm/V to 26.7 pm/V (Fig. 2.6), which is much larger than that of the bulk (0001) ZnO of 9.93 pm/V.

Due to the small thickness of nanobelts, spontaneous polarization and elasticity leads to the minimum of total energy resulting in helical growth [40]. Due to the unique combination of piezoelectric and semiconducting properties of 1D ZnO nanostructures, the latter can be used in nanopiezoelectronics for designing and fabricating electronic devices and components, such as field effect transistors, diodes, generators, sensors and actuators [10].

2.4.3 Biocompability, biodegradability and biosafety of ZnO

Fabrication of nanoscale biosensors based on ZnO nanorods, nanowires, and other nanomaterials has recently attracted enormous attention. Therefore, it is also crucial to explore their biosafety, biocompatible and bio-degradability. Several groups studied toxicity of nanostructured ZnO. ZnO nanoparticles are believed to be toxic which is related to the release of ionic zinc. Thus, it has been shown that dissolution behavior of ZnO is strongly dependant on the morphology of nanostructures. Muller et al. claimed that high aspect ratio ZnO nanowires are cytotoxic to human monocyte macrophages, indicating that toxicity is related to the Zn^{2+} release at a given pH [41]. On the other hand, George et al. reported that iron doping allows the reduction of ZnO cytotoxicity, as it provides slow Zn^{2+} release [42].

Recently, Z.L.Wang et al. shed the light on the biodegradability and biocompability of ZnO nanowires and nanobelts [13, 43]. They were the first to present a systematic study on the etching and dissolving behaviour of ZnO nanowires in various solutions with moderate pH values (e.g. water, ammonia, NaOH solution and horse blood serum). They showed that ZnO can be dissolved by deionized water (pH ≈ 4.5–5.0), ammonia (pH ≈ 7.0–7.1, 8.7–9.0) and NaOH solution (pH ≈ 7.0–7.1, 8.7–9.0). The study of the interaction of ZnO wires with horse blood serum shows that the ZnO wires can survive in the fluid for a few hours before they eventually degrade into mineral ions.

For the study of the stability of the ZnO wires in horse blood serum, a ZnO wire was fixed onto a Si substrate with Pt metal on two ends deposited by focus ion beam (FIB) microscopy. The Si substrate and the ZnO wire were immersed in the designated liquid (ca. 5 mL) for a controlled time. Subsequently, the Si substrate was taken out and washed with NaOH solution (pH ≈ 7.0–7.1) and ethanol for ca. 1 min, respectively. SEM image taken after each step to examine the morphology of the ZnO wires is shown in Fig. 2.7 (a-d).

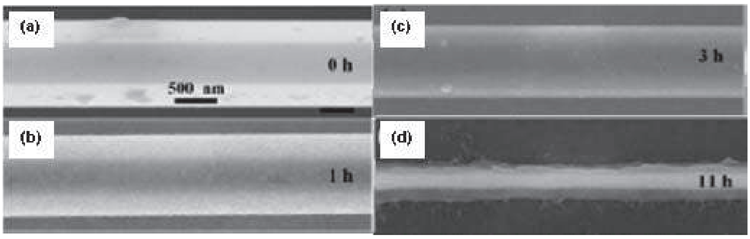

Figure 2.7: SEM images of a ZnO wire that has interacted with horse blood serum diluted in 10% aqueous NaOH solution (pH ≈ 7.9–8.2) for different lengths of time. a–d) SEM images of the ZnO wire after 0, 1, 3, and 11 h in the blood solution, respectively. The scale bar in (a) is the same for (b–d). (Reprinted from [13])

No visible etching of ZnO nanowire was observed after 1 h in the solution (Fig. 2.7 (b)). Subsequently, the etching became severe after 3 h of interaction as indicated by the reduced wire diameter (Fig 2.7 (c)), while increasing of etching time to 11 h (Fig. 2.7 (d)) resulted in ca. 94% by volume of the ZnO dissolution.

Later, they presented a cellular level study of biocompability and biodegradability of ZnO. Wang et al. found ZnO nanowires to be biocompatible and biosafe to two cell lines (Hela cells and L929 cells) from different origins of tissues in the incubation period up to 48 h keeping the nanowires concentration lower than 100 μg/ml [43]. All discussed makes ZnO an excellent candidate for the in vivo biomedical applications.

2.5 Morphology and synthesis of ZnO nanostructures

There is a large number of synthetic techniques that can result in a wide variety of shapes, size distributions and overall electrical, optical and piezoelectric properties of grown material. Together with the polar surfaces due to atomic terminations, ZnO is the unique material characterised by a diverse and versatile morphology family which is probably wider that any other material known (Fig. 2.8) [44,45]. Different nanostructures of ZnO have been reported such as wires, rods, combs, rings, loops, helices, bows, belts, flowers, cabbages, tetrapods, cages etc.

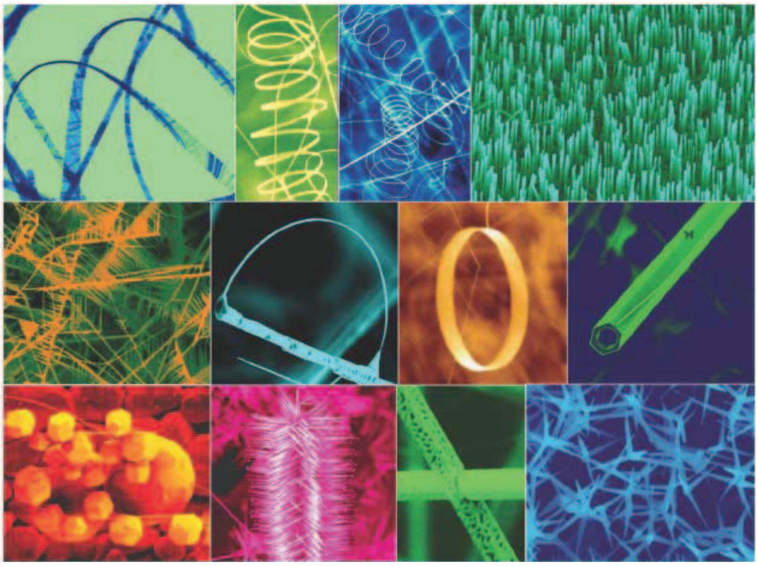

Figure 2.8: A collection of nanostructures of ZnO synthesized under controlled conditions by thermal evaporation of solid powders. (Reprinted from [44])

These structures have been efficiently synthesized with good reproducibility and crystal quality by tuning the growth rates along three types of fast growing directions. These directions are $\pm[0001]$, $\langle 01\bar{1}0\rangle$ ($\pm[01\bar{1}0], \pm[10\bar{1}0], \pm[1\bar{1}00]$) and $\langle 2\bar{1}\bar{1}0\rangle$ ($\pm[\bar{1}2\bar{1}0]$, $\pm[2\bar{1}\bar{1}0]$, $\pm[\bar{1}\bar{1}20]$) (Fig. 2.9) [46,47]. The polar faces are electrostatically unstable Tasker type III surfaces [48], making the $\pm[0001]$ planes have the highest energy of the low-index surfaces. Therefore the c-axis orientation is the preferred one for the ZnO hexagonal structure. The relative surface activities of various growth facets under given conditions are the key factor determining the morphology of grown material. Macroscopically, a crystal has different kinetic parameters for different crystal planes, which are emphasized under controlled growth conditions. Thus, after an initial period of nucleation and incubation, a crystallite will commonly develop into a three-dimensional object with well-defined, low index crystallographic faces.

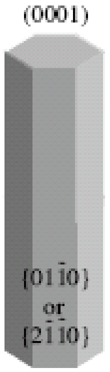

Figure 2.9: Typical growth morphologies of ZnO nanowire/nanorod with corresponding facets (Reprinted from [46])

Figure 2.9 shows a nanowire/nanorod morphology, which is mostly discussed in the present work, for ZnO nanostructures. These structures tend to maximize the areas of the $\langle 01\bar{1}0\rangle$ and $\langle 2\bar{1}\bar{1}0\rangle$ facets because of the lower energy [46]. The growth rates of various surfaces can also be kinetically controlled, especially in the case of solution-phase syntheses at moderate temperatures. For example, the growth of certain surfaces can be impeded by using additives that preferentially adsorb to specific crystal faces.

The ability to grow new and better quality materials for a wide variety of applications has been a major factor in the phenomenal growth of the opto-electronics, spintronics and sensing device-industry over the last few decades. Though, the fundamentals of all methods have been established in 60s – 70s years of last century, currently, the requirements in high quality large single crystals and uniform epitaxial layers gave rise to new developments. As of late, tremendous efforts were dedicated to design the synthetic methodologies to fabricate ZnO material. Some of the physical growth techniques allowing good control over the deposition procedure are molecular beam epitaxy (MBE), magnetron RF-sputtering, pulsed laser deposition [49-51] etc.

Approaches described in present work included chemical growth of ZnO. The chemical synthetic methods to grow ZnO nanostructures of various shape can be classified into two big groups as follows: gas phase synthesis and solution phase synthesis.

2.5.1 Gas phase synthesis

Gas phase synthesis uses gaseous environment in closed chambers. Normally the synthesis is conducted at rather high temperatures in the range 500 – 1500 ^{o}C. Some commonly used gas phase methods are vapor phase transport, which includes vapor-solid (VS) and vapor-liquid-solid (VLS) growth, physical vapor deposition, chemical vapor deposition, metal-organic chemical vapor deposition, thermal oxidation of pure Zn and condensation, microwave assisted thermal decomposition [52-56] etc. Some of these methods are discussed below.

The vapor-liquid-solid growth was proposed by Wagner et al. for the growth of silicon whiskers on liquid Au droplets places on a silicon substrate [58]. Later, P.Yang et al. applied the process for the ZnO growth with the use of gold as catalyst [59-61]. In the process the gold catalyst, dispersed in colloids or thin film on the substrate, initiates and guides growth, resulting in 5 - 20 μm long wires (Fig. 2.10). The process involves the high temperature (800 - 1000 ^{o}C) reduction of ZnO powder by carbon to form Zn and CO/CO_2 vapor. The Zn vapor is transported and reacting with the Au on the substrate forms alloy droplets. Supersaturation of the droplets is required to form crystalline ZnO nanowires. The Au thickness variation allows to control the diameter of the nanowires.

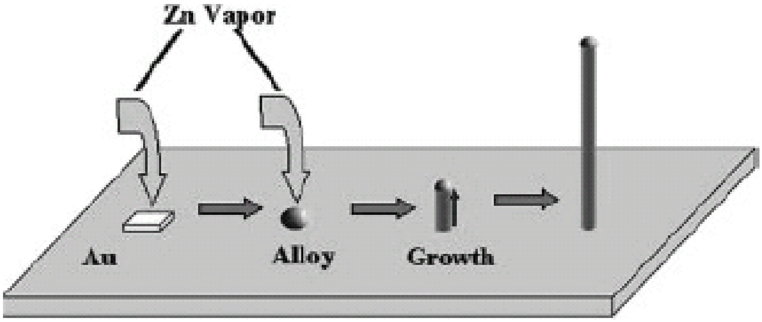

Figure 2.10: The Schematic representation of VLS growth (Reprinted from [61])

The spatial distribution of the catalyst particles determines the pattern of the nanowires allowing fine control of position and density of as-grown material. This step can be achieved using a variety of patterning technologies (e.g. lithography) for producing complex configurations. Fig. 2.11 represents typical scanning electron microscope (SEM) images of nanowire arrays grown on a-plane sapphire substrates.

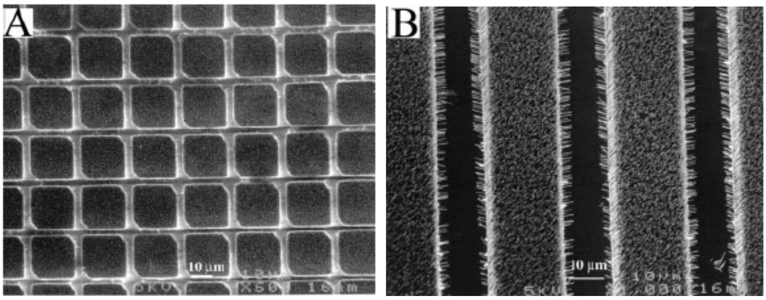

Figure 2.11: SEM images of patterned ZnO growth (Reprinted from [61])

These results confirm that the ZnO nanowires grow only in the Au-coated areas, and each nanowire is capped with Au–Zn alloy clusters on the tip and only in the presence of graphite. By adjusting the growth time, nanowires could be grown up to 40 µm length. The diameters of these wires range from 20 to 150 nm [61].

Apart from widely-used Au catalyst, Fe and Sn are also used for vapor-liquid–solid growth [62,63]. Wang et al. revealed that Sn particles can guide [0001] growth nanowires, as well as $[01\bar{1}0]$ and $[2\bar{1}\bar{1}0]$ growth nanobelts.

The interface prefers to take the least lattice mismatch, thus, the crystalline orientation of the tin particle may determine the growth direction and the side surfaces of the nanowires and nanobelts.

Another group suggested to use self-assembled thiol modified gold particles to promote site-selective growth of ZnO [64]. First, a patterned ZnO seed layer was fabricated using lithography. Gold nanoparticles functionalized with a layer of phosphonic acid were synthesized with uniform size. Then, using the charge interactions on surfaces of the ZnO seed layer and the Au nanoparticles, a monolayer of self-assembled Au nanoparticles was selectively deposited on the areas covered by ZnO seeds. Growth using a VLS process at 900 °C peak temperature resulted in aligned nanowire arrays on the patterned areas. This growth technique is likely to produce nicely patterned structures on any inorganic substrate regardless of whether it is crystalline or amorphous for a wide range of applications such as sensors, field emitting devices, and light-emitting devices.

The vapor-liquid-solid mechanism has been widely applied to the growth of ZnO nanostructures. However, its application is rather limited as it requires high growth temperatures (900 - 1200 ^{o}C) and expensive catalysts. Among other growth techniques, chemical vapor deposition (CVD) is particularly interesting not only because it gives rise to high-quality films but also because it provides high deposition rate, conformal step coverage, capability to coat complex shapes, adaptability to large scale processing and simplified apparatus [65]. On the downside, CVD processes are extremely complex and involve series of gas-phase and surface reactions, expensive and/or insulating (e.g. sapphire) substrates are often required for oriented growth, as well as the size and cost of the vapor deposition systems.

In the CVD method, ZnO deposition occurs as a result of chemical reactions of vapor-phase precursors on the substrate, which are delivered into growth zone by the carrier gas. The reaction takes place in the reactor where a necessary temperature profile is created in the gas flow direction.

Wu et al. reported ZnO nanorod growth on bare fused silica or silicon substrates at 500 ^{o}C [54]. To do so, zinc acetylacetonate hydrate was used as precursor and vaporized at 130 - 140 ^{o}C in a furnace. The N_2/O_2 flow was used as carrier gas to transfer the vapour into the reactor where substrates were placed. The as grown nanorods were oriented along c-axis direction having 60 - 80 nm in diameter. The photoluminescence study revealed three emitting bands, namely, strong ultraviolet emission at around 386 nm, a very week blue band

(440 ± 480 nm), as well as an almost negligible green band (510 ± 580 nm. Almost negligible green band suggests very low concentration of oxygen vacancies in the aligned ZnO nanorod array, which together with high UV emission makes it suitable for optoelectronic applications.

J.B. Baxter and E.S. Aydil described the use of zinc acetylacetonate to grow ZnO nanowires having dendric structures in oxygen atmosphere at 550 ^{o}C by using the same substrate in several growth cycles [66]. Repeating the growth procedure led to the growth of nanowires which acted as nuclei promoting the growth from shorter nanowires leading to a branched structure. Thus dendrite-like structure having high surface area and high density was employed as the wide-band-gap semiconductor to construct dye-sensitized solar cell with energy conversion efficiency of 0.5% with internal quantum efficiency of 70%.

Park et al. studied the effect of deposition temperature on the morphology of ZnO films [67]. Fig. 2.12 shows the ZnO morphology change with increase of the temperature. Thus, at very low growth temperatures of $T_g \leq 200$ °C, no ZnO formation was observed. Increase of the temperature to 200 °C < $T_g \leq 260$ °C led to columnar-like ZnO grains having a large amount of crystalline defects. Further rise in growth temperatures of 260 °C < $T_g \leq 320$ °C resulted in arrays of vertically well-aligned ZnO nanorods. The growth of ZnO nanoneedles was observed implying growth temperatures of 320 °C < $T_g \leq 380$ °C. However, at $T_g > 380$ C, ZnO nanowires start to grow on top of a continuous ZnO layer.

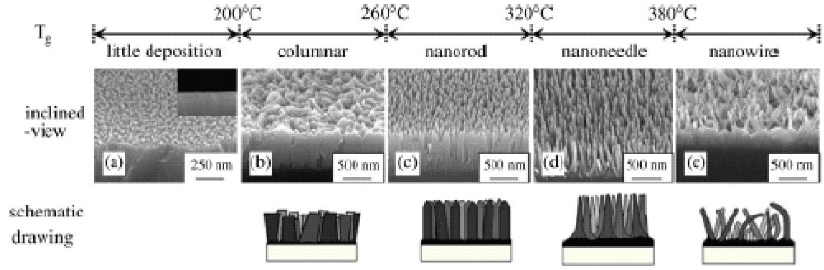

Figure 2.12: SEM cross section images of ZnO grown at various growth temperature (a) Tg≤ 200 °C, (b) 200 °C< Tg ≤260 °C, (c) 260 °C<Tg ≤320 °C (d) 320 °C < Tg ≤380 °C, and (e) Tg> 380 °C. The ZnO morphologies grown at these temperature regimes are schematically described (Reprinted from [67])

Along with growth from zinc acetylacetonate, the use of dimetyl- and diethyl zinc, alkoxide and solid acetate are reported in literature [68-71]. However, crystallite sizes of the precursors effect on the precursor evaporation rate and, therefore, the film growth rate [72]. Moreover, diethylzinc and dimethylzinc are extremely pyrophoric that is why zinc acetate or zinc acetylacetonate based precursors represent a good alternative as zinc sources to overcome the handling problems associated with the use of the pyrophoric compounds.

Recently, G. Malandrino et al. synthesized diamine adducts of zinc, the $Zn(tta)_2$·tmeda (htta = 2-thenoyltrifluoroacetone, tmeda = N,N,N',N'-tetramethylethylendiamine) for ZnO thin films MOCVD growth [73]. Such precursors are water-free, thermally-stable, volatile, and in liquid state at processing temperatures which allows to avoid fluctuations during the experiment [74]. The as synthesized precursor was employed for ZnO deposition in the temperature range 400 - 600 °C. The findings (see Fig. 2.13) suggested that the growth occurred in a kinetic regime within the reported temperature range resulting in a polycrystalline ZnO film formation [75].

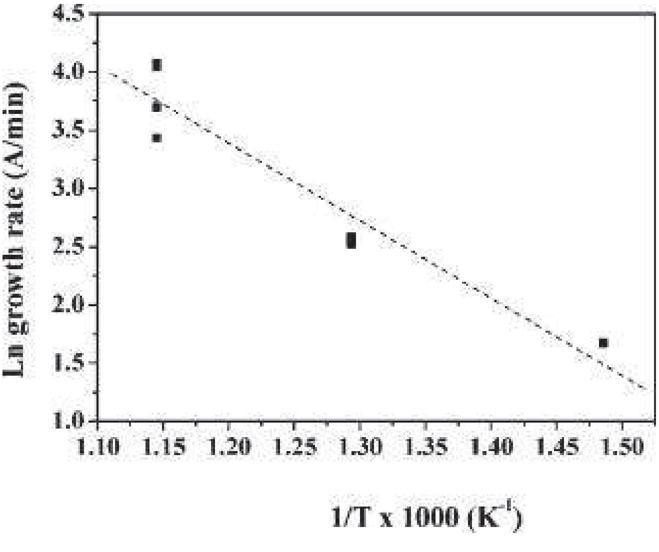

Figure 2.13: Arrhenius plot of deposition rate of ZnO film growth on quartz vs 1/T (Reprinted from [75])

2.5.2 Solution phase synthesis

Solution phase synthesis, in turn, provides the growth of ZnO material in a liquid. Normally aqueous or aqueous/alchoholic solutions are used. Some of the solution phase synthetic approaches are hydrothermal growth, chemical bath deposition, electrospinning, microwave-assisted approach [76-79] etc.

Solution phase synthesis possesses some advantages over the gas phase one due to low temperatures (<100 ^{o}C), formation of high density arrays, use of simple equipment, cheap and environmentally friendly chemicals, and large capacity of growth vessel used along with good quality of obtained crystals.

Literature review on ZnO growth has shown that for successful solution growth of high-quality crystals, growth system must satisfy the following requirements:

- ZnO-precursor (usually soluble zinc salt, e.g. nitrate, chloride, acetate) providing constant feedstock of Zn^{2+} to growth zone;
- purity of the precursor and mineralizers providing high quality of crystals;
- seed layers with crystallographic orientation (0001) providing growth of high-quality crystal with appropriate growth rates;
- growth conditions (temperature, pH, time, pressure) providing growth on seeds and absence of nucleation and growth in the solution to avoid precipitation.

However, the disadvantage of hydrothermal method over CBD is that it normally requires the presence of inner container isolating growth medium from autoclave walls (usually Pt, Ag, and Ti-alloy); need of complicated equipment to separate the reaction space onto two zones (dissolution zone and growth zone) with individual temperature control (baffle with 10–15% open space), as well as use of autoclaves to keep pressure at 50 - 200 atm.

The requirement of ZnO growth at low temperatures is attributed to the possibility of integrating with general substrates. Secondly, the 1D nanostructures, namely nanowires, nanorods, nanobelts, have to be of high quality with a high degree of control in size, orientation dimensionality, uniformity, and possibly shape. Finally, the catalyst may need to be eliminated for integration with silicon-based technology.

Laterally aligned ZnO nanowire arrays parallel to a substrate offer a potential benefit for fabricating integrated nano-device arrays. Taking advantage of the lattice match between ZnO and sapphire, Prof. Nikoobakht et al. received ZnO nanowires grown from two sides of gold pads deposited on a sapphire substrate [80]. However, the growth temperature (900 °C) and the choice of substrate are rather limited, which greatly restricts the integration of nanowires with silicon- or polymer-based devices. A general method has been developed to grow laterally aligned and patterned ZnO nanowire arrays on a general substrate as long as it is flat. Orientation control is achieved using the combined effect from a ZnO seed layer and the catalytically inactive Cr layer for nanowire growth. The growth temperature (100 °C) is so low that the method can be applied to a wide range of substrate materials that can be inorganic, organic, single crystal, polycrystalline, or amorphous.

Solution approaches to fabricate ZnO structures are appealing because of their low growth temperatures, low-cost, reproducibility and good potential for scale-up. Vayssieres et al. developed a hydrothermal process for producing arrays of ZnO microrods and nanorods on conducting glass substrates at 95 °C [81]. Later the process was used to grow flower like structures, rods and columns at similar temperature [82].

Greene et al. reported two-step deposition of ZnO nanowires on seeded with ZnO nanocrystals by spin-coating of silicon and plastic substrates with a subsequent growth in zinc nitrate hydrate aqueous solution in presence of methenamine or diethylenetriamine [83]. The as-grown nanowires were 200 nm in diameter and 3 μm in length said to be well-oriented. The method is claimed to be reproducible on a wide variety of substrates including ITO glass, sapphire, titanium foil and polymeric substrates. Annealing as-grown arrays in reducing atmospheres quenches the intense orange emission and lowers the lasing threshold of the larger nanowires to values similar to gas-phase samples.

Generally, in aqueous solution, zinc (II) is solvated by water, giving rise to aquo-ions. In dilute solutions, zinc(II) can exist as several monomeric hydroxyl species. These species include $ZnOH^+$(aq), $Zn\,(OH)_2$(aq), $Zn(OH)_2$(s), $Zn(OH)^{3\,-}$(aq), and $Zn(OH)_4{}^{2-}$(aq) [47].

At a given zinc (II) concentration, the stability of these complexes is dependent on various process parameters such as the pH and temperature of the solution. Solid ZnO nuclei are formed by the dehydration of these hydroxyl species. The ZnO crystal can continue to grow by the condensation of the surface hydroxyl groups with the zinc-hydroxyl complexes [84].

The hydrolysis and condensation reactions of zinc salts result in one-dimensional ZnO crystals under a wide variety of conditions. In general, rod/wire growth is possible in slightly acidic to basic conditions ($5 < pH < 12$) at temperatures from 50 to 200 °C [85]. Moreover, basic conditions are crucial for ZnO growth as divalent metal ions do not readily hydrolyze in acidic media. For growth at $pH < 9$, several amine-based ligands (hexamethylentetraamine

(HMTA), ethelenediamine (EDA), dimethylamineborane (DMBA), triethanolamine (TAA), diethylenetriamine (DETA)) were used to promote one-dimensional ZnO precipitation. These additives play role in decomposing during the reaction and increasing the pH to above 9 at the crystal surface.

On the other hand, the crystal morphology can be controlled by various species in the solution, which act as promoters or inhibitors for nucleation and growth. These species can include the zinc counter-ion, additives such as amines, and acids and bases. In general, additives such as DMBA and sodium citrate form platelets, while rods (aspect ratio < 10) and wires (aspect ratio > 10) form in the presence of amines such as HMTA, EDA, TAA, and DETA. Govender et al. studied the effect of the counterion for solutions containing HMTA [86]. Solutions containing acetate, formate, or chloride mainly formed rods, nitrate or perchlorate produced wires, and sulphate yielded flat hexagonal platelets. Although pH may play an important role in this case, these results show that the species in solution can have a strong effect on the resulting morphology.

In solution method, the pH of synthesis solution plays an important role in producing ZnO nanostructures. Literature review revealed that pH of the solution affects the density, size and shape of as-grown structures [31, 86-89]. Thus, increase of zinc nitrate solution pH value from 7.5 to 11 resulted in the growth of ZnO crystallites of higher density. The pH of counterion solution appeared to affect the morphology of the ZnO powders prepared in zinc nitrate solution, as one end-pointed shape was observed at a pH of 11, while lower pH value (6.7) led to structures with flat faces. Also, increase of the pH resulted in the diameter variation from 50 to 170 nm when the pH of the zinc nitrate solution was changed from 8.8 to 9.7. The use of acids (e.g. HCl and CH_3COOH) allows to control the pH and decreased its value to the acidic region from 6.5 to 5, inhibited the growth therefore reducing the size of ZnO crystals. Normally, wurtzite ZnO crystals were synthesized in a zinc sulfate solution with a pH range of 9 – 13. However, Yahiro and Imai used various additives (e.g.PO_4^{3-}, citric acid, tartatic acid, maleic acid, and phenolphthalein) to changed pH of zinc sulfate solution to modify the morphology of ZnO crystals [90].

2.6 Some applications of ZnO

ZnO nanostructures are very promising for sensor applications use due to their small dimension and high surface to volume ratio, chemical stability, the oxide is single crystalline, low cost, low power consumption, on-line operation and high compatibility with microelectronic processing. ZnO 1D structures have been used as active components in gas and bio- sensors, visible light sensors, visible-blind UV sensors, and strain sensors [91-94]. ZnO nanorod-based field effect transistors (FET) and nanogenerator-based sensors may open up opportunities for highly sensitive and selective real-time detection of a wide variety of gas and bio molecules [95-96].

The first report on ZnO sensing capability date back to 1960s, when Seiyama et al. demonstrated that the conductivity of ZnO thin films heated to 300 ^{o}C were sensitive to the presence of the reactive gases in the air [97]. Furthermore, various research groups reported the potential use of ZnO nanowires, owing to the large surface area and good piezoelectricity, for detecting NO_2, NH_3, NH_4, CO, H_2, H_2O, O_3, H_2S, formaldehyde, triethylamine and C_2H_5OH [4].

The potential of ZnO nanostructures as nanosized biosensors has also been explored for detecting different biological molecules such as glucose, cholesterol, proteins and DNA [98-101]. Development of 1D ZnO nanostructures as biosensors is in the state of infancy and only a limited number of reports are available. The 1D ZnO biosensors have advantages such as stability in air, non-toxicity, chemical stability, electrochemical activity, ease of synthesis, and bio-safe characteristics. As in the case of gas sensors, the principle of operation is that the conductance of ZnO nanorod FETs drastically changes when bio-molecules are adsorbed.

The key factor in most biological processes is the need for a small change of the pH concentration created by the release of H^+ ions during biochemical reactions. Therefore, determination of pH is a prerequisite for many processes. The sensing mechanism for pH is the polarization-induced bound surface charge by interaction with the polar molecules in the liquids. Application of ZnO nanorods as pH sensors for intracellular chemical sensing is under development and a room-temperature sensitivity (change in surface potential) as high as 59mV per decade change in the pH value has been reported [102].

2.7 Concluding remarks

ZnO offers a great potential in providing opto-electronic, photonic, piezoelectric and sensing devices, and astonishing progress has been made in the research up-to-date. Despite this progress, there is still a number of important issues that need to be further investigated before this material can be transitioned to commercial use for the stated applications. The task is made more difficult by the highly successful GaN and TiO_2 that compete for similar applications.

It is one of the most significant material in terms of the variety of synthetic techniques available to grow nanostructures of various shapes and morphology which coupled with outstanding properties determine its wide range of applications. However, there is still much to be understood in terms of growth mechanisms and accurate tailoring of ZnO nanostructures. Another issue is the ease of fabrication and high reproducibility of large arrays through vapor and solution techniques.

ZnO also paves its way to applications in sensing, in part, due to the ease with which ZnO can be produced in the form of nanostructures. In the case of ZnO-based sensing devices, the critical issues are high surface-to-volume ratio of the material and the good electron mobility and recombination properties, as well as the choice of ZnO processing and tailoring conditions, which are important in achieving the structures allowing high sensitivity and selectivity towards analyte molecules. There is still much to be understood in terms of the mechanism of ZnO gas and bio-sensors as the selectivity still remains to be the main issue since identification of the nature of the absorbed molecules is very important. Research on this topic is still facing challenges on both scientific and technological aspects.

References

1. Z.L. Wang, Appl. Phys. A- Mat. Sci. Eng. 88 (2007) 7-15.
2. K. Ellmer, A. Klein, B.Rech (Eds.), Transparent conductive zinc oxide: basics and applications in thin film solar cells. Series:Springer Series in Materials Science, Vol. 104 2008, XIV, 446 p.
3. C.F. Klingshim, B.K. Meyer, A. Waag, A. Hoffmann, J.M.M. Geurts

(Eds.), Zinc Oxide: From Fundamental Properties Towards Novel Applications, Springer, 2010, 300 p.

4. H. Morkoç, Ü. Özgür (eds.), Zinc Oxide: Fundamentals, Materials and Device Technology. Wiley-VCH, 2009, 477 p.
5. N. H. Nickel. Zinc oxide – a material for micro- and optoelectronic applications, Springer, 2005, 240 p.
6. Ch. Jagadish, S. J. Pearton (Eds.), Zinc Oxide bulk, thin films and nanostructures: processing, properties and applications, Elsevier, 2006, 589 p.
7. C.W. Bunn, Proc. Phys. Soc. 47 (1935) 835-842.
8. E. Mollwo, Z. Angew. Phys. 6 (1954) 257-260.
9. J.C. Philips, Bonds and Bands in Semiconductors, Academic Press, New York, 1973.
10. Z.L. Wang, Mat. Sci.Eng.R 64 (2009) 33-71.
11. O. Dulub, L.A. Boatner and U. Diebold, Surf. Sci. 519 (2002) 201-217.
12. B. Meyer and D. Marx, Phys. Rev. B 67 (2003) 035403.
13. J. Zhou, N.S. Xu, Z.L. Wang, Adv. Mater. 18 (2006) 2432–2435.
14. D.C. Reynolds, D.C. Look, B. Jogai, C.W. Litton, T.C. Collins, W. Harsch, G. Cantwell, Phys. Rev. B 57 (1998) 12151-12155.
15. Y.R.Ryu, T.S. Lee, J.A. Lubguban, H.W. White, B.J. Kim, Y.S. Park, C.J. Youn, Appl. Phys. Lett. 88 (2006) 241108-01-241108-02.
16. Y.F. Chen, D. Bagnall, T.F. Yao, Mat. Sci. Eng. B – Solid State Mater. Adv. Techn. 75 (2000) 190-198.
17. J.H. Choy, E.S. Jang, J.H. Won, J.H. Chung, D.J. Jang, Y.W. Kim, Adv. Mater. 15 (2003) 1911-1914.
18. E.M. Wong, P.C. Searson, Appl. Phys. Lett. 74 (1999) 2939-2941.
19. E.A. Meulenkamp, J. Phys. Chem. B 102 (1998) 5566-5572.
20. S. Choopun, R.D. Vispute, W. Noch, A. Balsamo, R.P. Sharma, T. Venkatesan, A. Iliadis, D.C. Look, Appl. Phys. Lett. 75 (1999) 3947-3949.
21. M.H. Huang, S. Mao, H. Feick, H.Q. Yan, Y. Wu, H. Kind, E. Weber, R. Russo, P.D. Yang, Science 292 (2001) 1897-1899.
22. F.M. Li, G.-W. Hsieh, S. Dalal, M.C. Newton, J.E. Stott, P. Hiralal, A. Nathan, P.A. Warburton, H.E. Unalan, P. Beecher, A.J. Flewitt, I. Robinson, G. Amaratunga, and W.I. Miln, IEEE Trans. Electron Devices, 55 (2008) 3001-3011.
23. D.M. Bagnall, Y.F. Chen, Z. Zhu, T. Yao, M.Y. Shen, T. Goto, Appl. Phys. Lett. 73 (1998) 1038-1041.

24. S.W. Jung, W.I. Park, H.D. Cheong, G.-C. Yi, H.M. Jang, S. Hong, T. Joo, Appl. Phys. Lett. 80 (2002) 1924-1926.
25. K. Vanheusden, W.L. Warren, C.H. Seager, D.R. Tallant, J.A. Voigt, B.E. Gnade, J. Appl. Phys. 79 (1996) 7983-7990.
26. W.I. Park, G.-C. Yi, M. Kim, S.J. Pennycook, Adv. Mater. 14 (2002) 1841-1843.
27. R. Dingle, Phys. Rev. Lett. 23 (1969) 579-581.
28. A. Ghosh, N.G. Deshpande, Y.G. Gudage, R.A. Joshi, A.A. Sagade, D.M. Phase Ramphal Sharma, J. Alloys Compd. 469 (2009) 56-60.
29. A.B. Djurišić, Y.H. Leung, K.H. Tam, L. Ding, W.K. Ge, H.Y. Chen, and S. Gwo, Appl. Phys Lett. 88 (2006) 103107-1-103107-3.
30. A.B Djurišić, Y.H. Leung, K.H. Tam, Y.F. Hsu, L. Ding, W.K. Ge, Y.C. Zhong, K.S. Wong, W.K. Chan, H.L. Tam, K.W. Cheah, W.M Kwok and D.L. Phillips, Nanotechnology 18 (2007) 095702.
31. J. Song, S. Baek, S. Lim, Physica B 403 (2008) 1960–1963.
32. C.-C. Lin, H.-P. Chen, H.-C. Liao, S.-Y. Chen, Appl. Phys. Lett. 86 (2005) 183103-1-183103-3.
33. A.K.Singh, V.Viswanath,V.C.Janu, J. Lumin. 129 (2009) 874–878.
34. T. Tan, B.J. Chen, X.W. Sun, W.J. Fan, H.S. Kwak, X.H. Zhang, S.J. Chua, J. Appl. Phys. 98 (2008) 13505-1-13505-3.
35. U.Ozgur, Ya. I. Alivov, C.liu, A.teke, M.A. Reschikov, S. Dogan, V. Avrutin, S.-J. Cho, and H. Morkoc, J. Appl. Phys. 98 (2005) 041301-041301-103.
36. Z. L. Wang, X. Y. Kong, Y. Ding, P. Gao, W.L. Hughes, R. Yang and Y. Zhang, Adv. Funct. Mater. 14 (2004) 943-956.
37. A.D. Corso, M. Posternak, R. Resta, A. Baldereschi, Phys. Rev. B 50 (1994) 10715-10721.
38. F. Bernardini, V. Fiorentini, D. Vanderbilt, Phys. Rev. B 56 (1997) 10024-10027.
39. M.H. Zhao, Z.L. Wang, S.X. Mao, Nano Lett. 4 (2004) 587-590.
40. X.Y. Kong and Z.L. Wang, Nano Lett. 3 (2003) 1625-1631.
41. K.H.Muller, J. Kulkami, M. Motskin, A. Goode, P. Winship, J.N. Skepper, M.P. Ryan, and A.E. Porter, ACS Nano 4 (2010) 6767-6779.
42. S. George, S. Pokhrel, T. Xia, B. Gilbert, Z. Ji, M. Schowalter, A. Rosenauer, R. Damoiseaux, K.A. Bradley, L. Madler, and A.E. Nel, ACS Nano 491 (2010) 15-29.

43. Z. Li, R.S. Yang, M. Yu, F. Bai, C. Li, Z.L. Wang, J. Phys. Chem. C. 112 (2009) 20114-20117.
44. Z.L. Wang, Mater. Today 7 (2004) 26-33.
45. Z.L. Wang, ACS Nano 2 (2008) 1987–1992.
46. Z.L. Wang, J. Phys.: Condens. Matter 16 (2004) R829-R858.
47. S. Baruah and J.Dutta, Sci Technol. Adv. Mater. 10 (2009) 013001.
48. P.W. Tasker, J. Phys. C: Solid State Phys. 12 (1979) 4977-4984.
49. M. Johnson, S. Fujita, W.H. Rowland, W.C. Hughes, J.W. Cook, J.F. Schetzina, J. Electron. Mater. 25 (1996) 855-862.
50. P.F. Carcia, R.S. McLean, M.H. Reilly, G.Nunes, Appl. Phys. Lett 82 (2003) 1117-1119.
51. J.L. Zhao, X.M. Li, J.M. Bian, W. D. Yu, X.D. Gao, J. Cryst. Growth 276 (2005) 507-512.
52. S.Y. Li, C.Y. Lee, T.Y. Tseng, J. Cryst Growth 247 (2003) 357-362.
53. Y.C. Kong, D.P. Yu, B. Zhang, W. Fang, S.Q. Feng, Appl. Phys. Lett. 78 (2001) 407-409.
54. J.J. Wu and S.C. Liu, Adv. Mater. 14 (2002) 215-218.
55. J.L. Yang, S.J. An, W.I. Park, G.C. Yi, W. Choi, Adv. Mat. 16 (2004) 1661-1664.
56. Y.G. Wang, S.P. Lau, H. W. Lee, S.F. Yu, B.K. Tay, X.H. Zhang, H.H. Hng, J. Appl. Phys. 94 (2003) 354-358.
57. A. Lagashetty, V.Havanoor, S. Basavaraja, S.D. Balaji, A. Venkataraman, Sci. Technol. Adv. Mat. 8 (2007) 484-493.
58. R.S. Wagner and W.C. Ellis, Appl. Phys. Lett. 4 (1964) 89-90.
59. M.H. Huang, S. Mao, H. Feick, H.Q. Yan, Y.Y. Wu, H. Kind, E. Weber, R. Russo, P.D. Yang, Science 292 (2001) 1897–1899.
60. M.H. Huang, Y. Wu, H. Feick, N. Tran, E. Weber and P. Yang, Adv. Mater. 13 (2001) 113-116.
61. P. Yang, H. Yan, S. Mao, R. Russo, J. Johnson, R. Saykally, N. Morris, J. Pham, R. He and H.-J. Choi, Adv. Funct. Mater. 12 (2002) 323-332.
62. Y. Ding, P.X. Gao and Z.L. Wang, J. Am. Chem. Soc. 126 (2004) 2066-2072.
63. P. X. Gao and Z. L. Wang, J. Phys. Chem. B 108 (2004) 7534-7537.
64. D. Ito, M.L. Jespersen and J.E.Hutchison, ACS Nano 2 (2008) 20001-20006.

65. M.L. Hitchman, K.F. Jensen (Eds.), Chemical Vapor Deposition: Principles and Applications; Academic Press, London, 1993, 677 pp.
66. J.B. Baxter and E.S. Aydil, Appl. Phys. Lett 86 (2005) 053114-1-053114-3.
67. J.Y. Park, D.J. Lee, Y.S. Yun, J.H. Moon, B.-T. Lee, S.S. Kim, J. Cryst. Growth 276 (2005) 158-164.
68. J.D. Ye, S.L. Gu, F.Qin, S.M. Zhu, S.M. Liu, X. Zhou, W. Liu, L.Q. Hu, R. Zhang, Y. Shi, Y.D. Zheng, Y.D. Ye, Appl. Phys. A 81 (2005) 809-812.
69. T. Kaufmann, G.Fuchs, M. Webert, S. Frieske, M. Gackle, Cryst. Res. Techn. 24 (1989) 269-274.
70. J. Auld, D.J. Houlton, A.C. Jones, S.A. Rushworth, M.A. Malik, P. O'Brien and G. W. Critchlow, J. Mater. Chem. 4 (1994) 1249-1253.
71. J. Hu, R.G. Gordon, J. Appl. Phys. 71 (1992) 880-890.
72. M.L. Hitchman, S.H. Shamlian, D.C. Gilliland, D. Cole-Hamilton, J.A.P. Nash, S.C. Thompson, S.L. Cook, J. Mater. Chem. 5 (1995) 47-52.
73. G. Malandrino, M. Blandino, L.M.S. Perdicaro, I.L. Fragala', P. Rossi, and P.Dapporto, Inorg. Chem. 44 (2005) 9684-9689.
74. J. Ni, H. Yan, A. Wang, Y. Yang, C.L. Stern, A.W. Metz, J. Shu, L. Wang, T.J. Marks, J.R. Ireland, C.R. Kannewurf, J. Am.Chem. Soc. 127 (2005) 5613-5624.
75. G. Malandrino,M. Blandino, M.E. Fragala, M. Losurdo, and G. Bruno, J. Phys. Chem. C 112 (2008) 9595–9599
76. B.Liu, H.C. Zeng, J. Am. Ceram. Soc. 125 (2003) 4430-4431.
77. S.H. Yi, S.K. Choi, J.M. Jang, J.A. Kim, W.G. Jung, J. Colloid Interface Sci. 313 (2007) 705-710.
78. D.D. Lin, W. Pan, H.J. Wu, J. Am. Ceram. Soc. 90 (2007) 71–76.
79. A.S. Shaporev, V.K. Ivanov, A.E. Baranchikov, Y.D. Tretyakov, Inorg. Mater. 43 (2007) 35-39.
80. B. Nikoobakht, Chem. Mater. 19 (2007) 5279-5284.
81. L. Vayssieres, Adv. Mater. 15 (2003) 464-466.
82. W. Peng, S. Qu, G. Cong, Z. Wang, Cryst. Growth Des. 6 (2006) 1518-1522.
83. L. E. Greene, M.Law, J. Goldberger, F.Kim, J.C.Johnson. Y.Zhang, R.J. Saykally, P.Yang, Angew. Chem. Int. Ed. 42 (2003) 3031-3034.
84. M. Law, L.E.Greene, J.C. Johnson, R.Saykally and P.Yang. Nature Mater. 4 (2005) 455-459.

85. L.E. Greene, B.D. Yuhas, M. Law, D. Zitoun, P. Yang, Inorg. Chem. 45 (2006) 7535-7543.
86. K. Govender, D.S. Boyle, P.B. Kenway, and P. O’Brien, J. Mater. Chem. 14 (2004) 2575-2591.
87. J.H. Kim, E.M. Kim, D. Andeen, D. Thomson, S.P. DenBaars, F.F. Lange, Adv. Funct. Mater. 17 (2007) 463-471.
88. A.Y.L. Sim, G.K.L. Goh, S. Tripathy, D. Andeen, F.F. Lange, Electrochim. Acta 52 (2007) 2933-2937.
89. K. Yu, Z. Jin, X. Liu, J. Zhao, J. Feng, Appl. Surf. Sci. 253 (2007) 4072-4078.
90. J. Yahiro and H. Imai, Key Eng. Mater. 320 (2006) 155-158.
91. Q. Wan, Q.H. Li, Y.J. Chen, T.H. Wang, X.L. He, J.P. Li, C.L. Lin, Appl. Phys. Lett. 84 (2004) 3654-3656.
92. A. Wei, X.W. Sun, J.X. Wang, Y. Lei, X.P. Cai, C.M. Li, Z.L. Dong, W. Huang, Appl. Phys.Lett. 89 (2006) 123902-1-12902-3.
93. M. Li, G. Meng, Q. Huang, Z. Yin, M. Wu, Z. Zhang, M. Kong, Langmuir 26 (2010) 13703-13706.
94. T.V. Cuong, H.N. Tien, V.H. Luan, V.H. Pham, J.S. Chung, D.H. Yoo, S.H. Hahn, K.-K. Koo, P.A. Kohl, S.H. Hur, E.J.Kim, Phys. Status Solidi 208 (2011) 943-946.
95. C.S. Lao, Q. Kuang, Z.L. Wang, M.-C. Park, Y. Deng, Appl. Phys. Lett. 90 (2007) 262107-1-262107-3.
96. M. Lee, J. Bae, J. Lee, C.-S. Lee, S. Hong and Z. L. Wang, Energy Environ. Sci. 4 (2011) 3359-3363.
97. T. Seiyama, A. Kato, K. Fujiishi, and M. Nagatani, Anal. Chem. 34 (1962) 1502-1503.
98. M.H. Asif, A. Smu, O. Nur, M. Willander, C. Brannmark, P. Stralfors, E. Uh, F. Elinder, B. Danielson, Biosens. Bioelectron. 25 (2010) 2205-2211.
99. A. Umar, M.M. Rahman, M. Vaseem, Y.-B. Hahn, Electrochem. Commun. 11 (2009), 118-121.
100. S. Krishnamoorthy, A.A. Iliadis, T.Bei, G.P. Chrousos, Biosens. Bioelectron. 24 (2008) 313-318.
101. N. Kumar, A. Dorfman and J. Hahm, Nanotechnology 17 (2006) 2875-2881.
102. S.M. Al-Hilli, R.T. Al-Mofarji, and M. Willander, Appl. Phys. Lett. 89 (2006) 173119-1–173119-3.

3. Experimental methodology and material synthesis

3.1 Introduction

This chapter describes the experimental conditions which were used in the work for this thesis. The first part of the chapter describes the system of deposition used for the fabrication of ZnO nanostructures. The second part of this chapter is dedicated to the characterization methods of the used for measurements of structural, crystal and optical properties of the ZnO nanostructures.

3.2 Preparation of substrates

The substrates used for the deposition were (i) monopolished (100) silicon (University Wafer), quartz and glass substrates. Specifically, glass coverslip (Biopthecs) were used for confocal microscopy measurements.

Silicon substrates prior to use have been etched in HF (7:1 HF/H_2O dilution) for 60 s in order to remove the surface native oxide, washed with water and blown with nitrogen. As for the glass and quartz substrates they have been sonicated for 15 min in acetone, ethanol and Millipore water respectively and blown with nitrogen.

Prior to nanopatterning the seedless substrates were cleaned with piranha (H_2O_2:H_2SO_4 1:3) for 10 minutes.

3.3 Synthesis of metal organic precursor

Materials. Zinc acetate dehydrate ($Zn(CH_3COO)_2$ $2H_2O$, MW = 219.51, Carlo Erba), 2-thenoyltrifluoroacetone (H-tta) ($CF_3COCH_2COC_4H_3S$, MW = 222.18, STREM Chemicals), N, N, N', N' - tetramethyletilendiamine (TMEDA/tmeda) ($(CH_3)_2NCH_2CH_2N(CH_3)_2$, MW=116.21, Alfa Aesar), dichloromethane (CH_2Cl_2, MW=84.93, Sigma Aldrich), Ethanol (C_2H_5OH, MW = 46.07, Sigma Aldrich), Pentane (C_5H_{12}, MW = 72.15, Sigma Aldrich). All chemicals were of analytical reagent grade and used without further purification.

A diamine (N,N,N',N'-tetramethyletilendiamine) adduct of zinc bis(2-thenoyl-trifluoroacetonate) has been used as a metal-organic precursor [1]. For the synthesis, an aqueous solution of $Zn(CH_3COO)_2$ $2H_2O$ (2.064 g) in 50 ml of H_2O was added to a CH_2Cl_2 solution (40 ml) containing H-tta (4.177 g) and TMEDA (1.418 ml):

The resulting solution was vigorously stirred at room temperature for 2 h. The $Zn(tta)_2$ tmeda, insoluble in the CH_2Cl_2/H_2O mixture, precipitates, and is recovered by adding ethanol (20 ml). The solution was left to crystallize, and the $Zn(tta)_2$·tmeda crystals were washed with small quantities of pentane, in which the adduct is insoluble.

3.4 Synthesis of catalyst

Materials. Silver oxide (Ag_2O, PM = 231.74, Sigma Aldrich), 1,1,1,5,5,5-hexafluoro-2,4-pentanedione (H-hfa), ($C_5H_2F_6O_2$, PM = 208,06, Sigma Aldrich), 2,5,8,11,14-pentaoxatetradecane (tetraglyme), ($CH_3O(CH_2CH_2O)_4CH_3$, PM = 222.28, Sigma Aldrich). All chemicals were of analytical reagent grade and used without further purification.

The adduct of Ag(hfa)·tetraglyme precursor, whose synthesis has been reported elsewhere [2], used to obtain catalyst layer promoting ZnO growth, was synthesized using single-step reaction of silver oxide (2.317g) with 1,1,1,5,5,5-hexafluoro-2,4-pentanedione (4.161g) and tetraglyme (4.445g) in dichloromethane (50 ml).

The resulting solution was vigorously stirred at room temperature for 1 h. The solution was left to crystallize, and the Ag(hfa)·tetraglyme crystals were washed with small quantities of pentane, in which the adduct is insoluble.

3.5 Catalyst patterning

The adduct of Ag(hfa)·tetraglyme precursor was dissolved in ethanol and solutions having various concentrations, i.e. 0.1 M and 0.01 M, were prepared. The above mentioned solutions were drop casted (20 μl drop) on Si substrates, dried at room temperature and annealed in air at 400 °C for 30 min.

3.6 ZnO nanostructure fabrication techniques

The oxide nanostructures to be discussed in present work were synthesized by metal-organic chemical vapor deposition and/or chemical bath deposition integrated with electrospinning or colloidal nanosphere lithography techniques.

3.6.1 Metal-Organic Chemical Vapor Deposition

Chemical vapor deposition (CVD) is a process whereby a thin solid film is deposited onto a substrate from the gaseous phase by a chemical reaction. It is this reactive process which distinguishes CVD from physical deposition processes, such as evaporation, sputtering and sublimation.

According to the characteristics of the CVD processing parameters, CVD methods are generally classified and categorized into seven main types of fabrication depending on temperature, pressure, wall/substrate temperature, precursor nature, depositing time, gas flow state and activation manner.

Classified by operating pressure:

- Atmospheric pressure CVD (APCVD) - CVD processes at atmospheric pressure.
- Low-pressure CVD (LPCVD) - CVD processes at subatmospheric pressures.
- Reduced pressures tend to reduce unwanted gas-phase reactions and improve film uniformity across the wafer. Most modern CVD process are either LPCVD or UHVCVD.
- Ultrahigh vacuum CVD (UHVCVD) - CVD processes at a very low pressure, typically below 10^{-6} Pa.

Classified by physical characteristics of vapour:

- Aerosol assisted CVD (AACVD) - A CVD process in which the precursors are transported to the substrate by means of a liquid/gas aerosol, which can be generated ultrasonically. This technique is suitable for use with non-volatile precursors.
- Direct liquid injection CVD (DLICVD) - A CVD process in which the precursors are in liquid form (liquid or solid dissolved in a convenient solvent). Liquid solutions are injected in a vaporization chamber

towards injectors. Then the precursor vapours are transported to the substrate as in classical CVD process. This technique is suitable for use on liquid or solid precursors. High growth rates can be reached using this technique.

Plasma-assisted methods also exist:

- Microwave plasma-assisted CVD (MPCVD)
- Plasma-Enhanced CVD (PECVD) - CVD processes that utilize plasma to enhance chemical reaction rates of the precursors. PECVD processing allows deposition at lower temperatures, which is often critical in the manufacture of semiconductors.
- Remote plasma-enhanced CVD (RPECVD) - Similar to PECVD except that the wafer substrate is not directly in the plasma discharge region. Removing the wafer from the plasma region allows processing temperatures down to room temperature.

Depending on the precursors used, one can distinguish metal–organic chemical vapor deposition (MOCVD) - CVD processes based on metal-organic precursors and inorganic chemical vapor deposition employing inorganic precursors respectively.

Metal-Organic Chemical Vapor Deposition (MOCVD), also known as organo-metallic chemical vapor deposition (OMCVD), metal-organic vapor phase epitaxy (MOVPE), and organo-metallic vapor phase epitaxy (OMVPE), is nowadays one of the most commonly used deposition techniques in the semiconductor manufacturing. In principle, MOCVD involves the formation of a thin solid film on a substrate material by a chemical reaction of metal-organic vapor-phase precursor [3]. It is this reactive process which distinguishes CVD from physical deposition processes, such as evaporation, sputtering and sublimation [4,5].

The ability to grow new and better quality materials for a wide variety of applications has been a major factor in the phenomenal growth of MOCVD over the last few decades.

This process can be used to obtain products with a variety of applications such as coatings, semiconductors, optical fibres, ceramic matrix composites (i.e. carbon- carbon, carbon-silicon carbide and silicon carbide-silicon carbide composites), catalysts, nanopowders etc.

Metal-organic sources or complexes with organic ligands for the MOCVD include $M(CH_3)_n$, $M(Ot\text{-}Bu)_n$, $MN(CH_3)_{3n}$, $M[RC(O)CHC(O)R]_n$. With the increasing demand for more sophisticated deposits, especially of optoelectronic materials, and the need for tighter control of deposition rates, uniformity and layer properties and quality, there has been a major interest in recent years in metal-organic precursors where the metal has been made volatile by bonding it to organic ligands.

MOCVD precursors should have particular chemical and physical properties: be thermally stable and highly volatile, be easily synthesized in significant quantities and easily purified, be stable on air, have high purity and be low or non toxic.

In a typical deposition process mass transport takes place in the bulk gas flow region from the reactor inlet to the deposition zone, reactions in the gas phase provide the formation of film precursors and byproducts, followed by mass transport of film precursors to the growth surface and their adsorption on the growth surface due to surface diffusion of film precursors to growth sites and incorporation of film constituents into the growing film. After what by-products of the surface reactions are desorbed and transported in the bulk gas flow region away from the deposition zone towards the reactor exit.

The growth of thin film in this case is initiated by exposing a suitably prepared substrate to the film precursors in the reactor. The resulting growth and microstructure of the film is determined by surface diffusion and nucleation processes on the growth interface, which are influenced by the substrate temperature, reactor pressure, and gas-phase composition.

An amorphous film is formed at low temperatures (and high growth rates) when the surface diffusion is slow relative to the arrival rate of film precursors. At high temperatures (and low growth rates) the surface diffusion is fast relative to the incoming flux, allowing the adsorbed species to diffuse to step growth and to form epitaxial layers replicating the substrate lattice. Nucleation occurs at many different points on the surface at intermediate temperatures (and growth rates). Adsorbed species then diffuse to the islands which grow and coalesce to form a polycrystalline film. The presence of impurities increases the nucleation density and shifts the transition of epitaxy to higher substrate temperatures.

In a first-order approximation and assuming thermodynamic equilibrium, the growth morphology can be established from the balance of the various surface free energies involved according to the following expression [6]

$$\Delta\gamma_{total} = \gamma_{ads} + \gamma_i - \gamma_s \qquad (3.1)$$

where the sub indices *ads*, *i*, and *s* stand for adsorbate, interface, and substrate, respectively. Three different growth modes must be considered (Fig. 3.1).

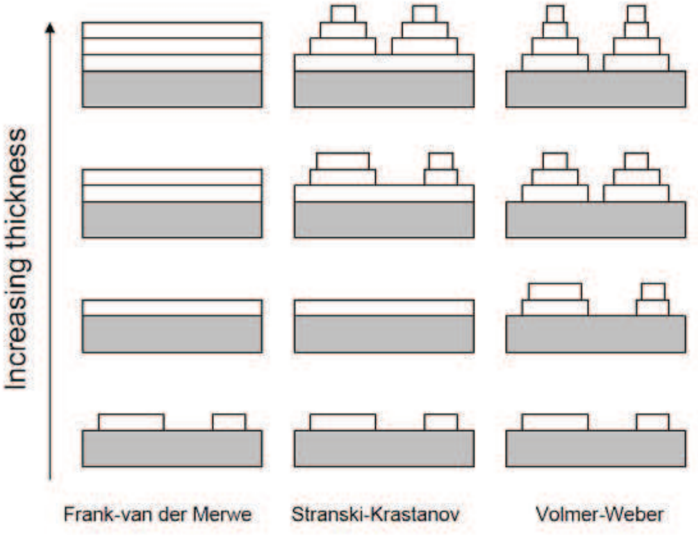

Figure 3.1: Classification of epitaxial growth modes (Reprinted from [8])

If $\Delta\gamma_{total} < 0$, the sum $\gamma_{ads} + \gamma_i$ is inferior or equal γ_s, which means that the energetic cost of creating a substrate-adsorbate and an adsorbate-vacuum interface is less than the substrate surface free energy; substrate coverage is favored, and the deposit grows in a layer-by-layer manner. This is the Frank-van der Merwe growth mode [7]. Pagni showed that in heteroepitaxial systems with a substantial lattice mismatch, like the ZnO/Si system, the elastic strain energy amassed with increasing thickness must also be taken into account. Indeed, this fourth energy term is accountable for the break-up of the film into three-dimensional islands after the growth of a few atomic layers [8]. This is the Stranski-Krastanov growth mode [9]. Finally, if $\Delta\gamma_{total} > 0$, the system aims to keep the substrate surface bare as long as possible whilst minimizing the exposed area of the deposit, thus generating the formation of 3D islands. This is the Volmer -Weber growth mode [10].

Herein, the ZnO films and nanostructures were synthesized by MOCVD process. The deposition was carried out on Si (100), glass and quartz substrates 10 mm x 20 mm using a reduced pressure horizontal hot-wall MOCVD reactor (Fig. 3.2).

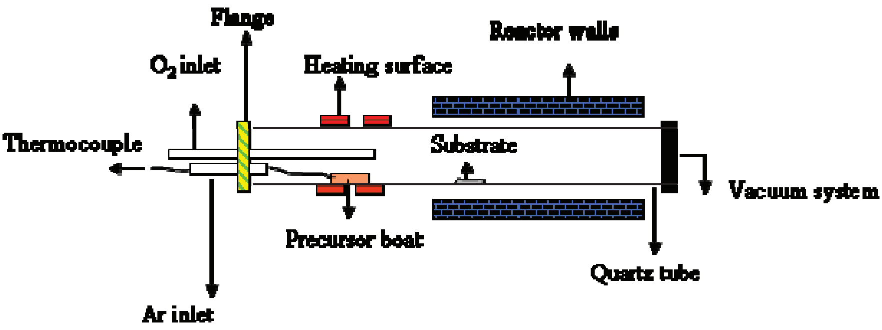

Figure 3.2: Schematic representation of MOCVD reactor

The processes was carried out in a horizontal tube furnace, which is composed of a horizontal tube furnace, a quartz tube, a rotary pump system and a gas supply and control system. The left-hand end of the quartz tube is connected to the rotary pump. Both ends are sealed by rubber O-rings. The ultimate vacuum for this configuration was 3 Torr. The carrying gas comes in from the right end of the quartz tube and is pumped out at the left end. Two pyrex traps are used to intrap the vapors of decomposition. The source material was loaded on a boat and positioned in the quartz tube, where the temperature is the highest. The substrates were placed downstream for collecting growth products. This simple setup can achieve high control of the final product.

The success of a MOCVD process depends critically on the availability of volatile, thermally stable precursors that exhibit high and constant vapor pressures to achieve uniform and reproducible film growth. Herein, the used precursor material, namely diamine adduct $Zn(tta)_2{\cdot}tmeda$, was evaporated at elevated temperature (170 °C) and then the resultant vapor phase by means of argon carrier gas was transferred to the reactant zone and condensed under certain conditions to form the desired product.

It is worth of note that the use of conventional liquid dimethyl-Zn and diethyl-Zn complexes or of the solid acetate, alkoxide, and acetyl- acetonate zinc complexes as precursors presents some drawbacks mainly related to their pyrophoric nature. In the case of dialkyl zinc complexes there is another disadvantage because of the effects of crystallite sizes on the precursor evaporation rate and, hence, on the film growth rate, in the case of solid source [11]. Conversely, $Zn(tta)_2{\cdot}tmeda$ used in the molten phase, thus represent a, a safe-handling alternative as liquid precursor thermally stable under processing conditions.

The substrate temperature was varied in the range 250 - 700 °C. Depositions were carried out for 5 - 90 min.

Oxygen gas was used as reactant gas. The mass flows were controlled with 1160 MKS flow-meter using an MKS147 electronic control unit. Total gas flow of 500 sccm was employed keeping an Ar/O_2 ratio of 1:1 (Ar/O_2 250/250sccm).

ZnO films deposited at T > 500 °C are uniform with smooth surfaces, good crystal and optical quality. The process is reproducible and can be tuned by adjusting the main process parameters such us temperature, and gas flows.

3.6.2 Chemical Bath Deposition

Chemical Bath Deposition (CBD), also known as liquid phase deposition, is a technique originated more than 150 years ago with a main focus on the deposition of chalcogenide and oxide compounds [12]. CBD is a low-cost, environmently friendly and low-temperature operation method, also convenient for a large-area deposition.

It does not require sophisticated instrumentation like vacuum systems and other expensive equipments. The starting chemicals are commonly available and are cheap materials. With chemical bath deposition a large number of substrates can be coated in a single run with a proper jig design. Unlike in electrodeposition, electrical conductivity of the substrate is not a necessary requirement in chemical deposition. Hence any insoluble surface to which the solution has free access will be suitable substrate for the deposition. The low temperature deposition avoids oxidation or corrosion of metallic substrates. Chemical bath deposition results in pinhole free and uniform deposits as the solution from which these are deposited always remains in contact with the substrate. Stoichiometric deposits are easily obtained since the basic building blocks are ions instead of atoms. In the case of CBD, solution chemistry is chosen in such a way that a spontaneous reaction from liquid phase is possible, contrary to spray pyrolysis where due to different solution chemistry; the reaction needs much higher temperature to process (273–233 K) and thus takes place from the vapour phase [13].

This method involves immersion of a substrate in an aqueous solution containing precursor species. It includes particle growth at surface nucleation sites in parallel with deposition of particles formed in solution [14]. In case of aqueous growth of ZnO, metal cations Zn^{2+} are solvated by water giving rise to aquo-ions intermediates. Generally, amine-based ligand is used to supply the hydroxyl ions through thermal degradation promoting the precipitation reaction.

This can be summarized in the following equations:

$$4OH^- + Zn^{2+} \rightarrow Zn(OH)_n^{m-} \tag{3.2}$$

$$Zn(OH)_n^{m-} \rightarrow ZnO + H_2O + 2OH^- \tag{3.3}$$

Moreover, amine ligand plays as buffer to control the pH of the bath. In turn, hydroxyl ions react with Zn^{2+} ions to form ZnO [15]. Depending on given pH and temperature ZnO can be formed from these intermediated through dehydratation of these intermediates [15,16].

Generally, the conditions (composition of the solution, deposition temperature, reactivity of the substrate surface) are chosen so to allow the deposition on the surface (heterogeneous process), and minimize the reaction in the liquid phase (homogeneous process).

The CBD procedure involved in this work was as follows:

The zinc acetate dehydrate $Zn(CH_3COO)_2{\cdot}2H_2O$ dissolved in distilled water at 70 °C was admixed with a separately prepared *N,N,N',N'*-tetramethylethylenediamine (TMEDA) or ethylendiamine (EDA) solution in distilled water. The zinc acetate and the TMEDA/EDA ligand concentrations were kept to a 1:1 molar ratio in all the experiments (in order to maintain the same degree of supersaturation), while the molar concentrations in final solution were ranging from 5 to 50 mM. No pH adjustment has been done. The resulting cloudy ZnO-containing suspensions were maintained at 70 °C without stirring for a time ranging from 30 min to 6 h to grow ZnO nanorods. The substrates containing seed layers were immersed in the solution for a fixed period of time to promote the growth. At the end of the process all the samples were extensively washed with distilled water and dried in nitrogen ambient.

3.7. Template fabrication techniques

In this work ZnO was also grown on pre-fabricated templates representing two-dimensional arrays of polystyrene nanospheres obtained by nanosphere colloidal lithography approach, as well as on inorganic nanofibers created via electrospinning which were used as supports to grow three dimensional hierarchical zinc oxide nanostructures.

3.7.1 Electrospinning

Electrospinning is a highly versatile method to process solutions or melts into continious fibers with diameters ranging from a few micrometers to a few nanometers. A large number of polymer/metal oxide composite fibers have been produced by electrospinning combined sol-gel process. In such case, the composite fibers could be converted into metal oxide by subsequent pyrolysis [17]. Electrospun nanofibers can be used as templates for hollow growth, filters and textile applications, tissue engineering, drug delivery and catalytic applications.

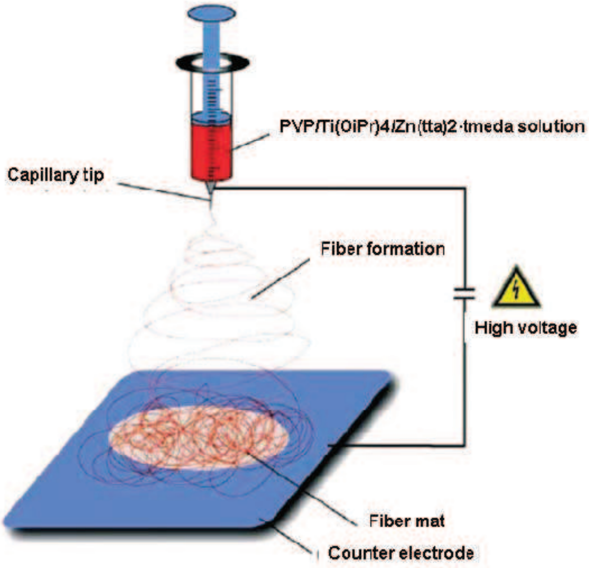

Figure 3.3: Typical electrospinning setup [17]

In experimental set-up employed (Fig. 3.3) polyvinylpyrolidone (PVP) solution (7 %wt) was prepared dissolving PVP (Aldrich, MW=1300000) powder in ethanol at room temperature under magnetic stirring. TiO_2 precursor solution was prepared, by mixing 1.5 g of titanium tetraisopropoxide ($Ti(OiPr)_4$, Aldrich) with 3 ml of acetic acid and 3 ml of ethanol and stirring for 10 minutes. The resulting mixture was added to 7.5 ml of PVP solution previously prepared and stirred for further 10 minutes. Zn doping was made by mixing the $Ti(OiPr)_4$ and

$Zn(tta)_2 \cdot tmeda$ solutions (1% molar). The obtained solution was poured in a glass syringe (Hamilton, Carlo Erba) equipped with a 21 G needle, fixed in a digitally controlled syringe pump (KD Scientific, MA, USA). The needle was connected to a high-voltage supply (Spellman, Model SL 30, NY, USA) that is capable of generating DC voltages up to 30 kV. The solution was electrospun in air on a Si substrate and the obtained sample was dried under vacuum for 24 h. The resulting ZnO/ TiO_2/PVP nanofibers were finally calcined in air at 500 °C for 3 hours (heating rate 5 °C/m, cooling rate 2 °C/m), in order to completely remove the polymeric component, and were used as template for the following ZnO deposition.

3.7.2 Nanosphere Colloidal Lithography

Nanolithography is a process for fabricating functional nanostructures from bulk materials. In particular, Nanosphere Colloidal Lithography (NSCL) is an inexpensive, inherently parallel, high-throughput, and materials-general nanofabrication technique capable of producing well-ordered 2D and 3D periodic particle arrays of nanoparticles using the self-assembly of colloids [18].

Spontaneous formation of well-ordered colloidal arrays provides lithographic masks or scaffolds for creating useful patterns. Materials with designed functional nanopores, hemispherical metal caps and sculptured colloids have been fabricated by colloidal templating for various applications. And can be used for patterning biomaterials, which are relevant for the fabrication of biosensors or biochips. High efficiency in NSCL for nanofabrication is due to the fact that large-area spontaneous assembly of a colloid can be produced by the relatively easy methods such as spin-coating or drop-casting.

Figure 3.4 illustrates the representative NSCL techniques. Route A shows a templating of organic and inorganic materials with a hexagonally packed structure, while route B shows the creation of nanorings using metal sputtering and ion milling; Route C shows the nanomachining process to fabricate regular holes on colloids for functionalization [19].

In the presented work, the mask formed by a 2D close-packed monolayer of polystyrene colloids of 200 nm and 1μm of diameter (Sigma), self-assembled by dewetting (1 wt.% in aqueous solution), was achieved on Si or glass substrates with and without ZnO layer. Such mask was subsequently used for the ZnO nanohole array formation via MOCVD or CBD methods. The residues of polystyrene spheres were removed by soaking in toluene overnight, and subsequently washed in distilled water.

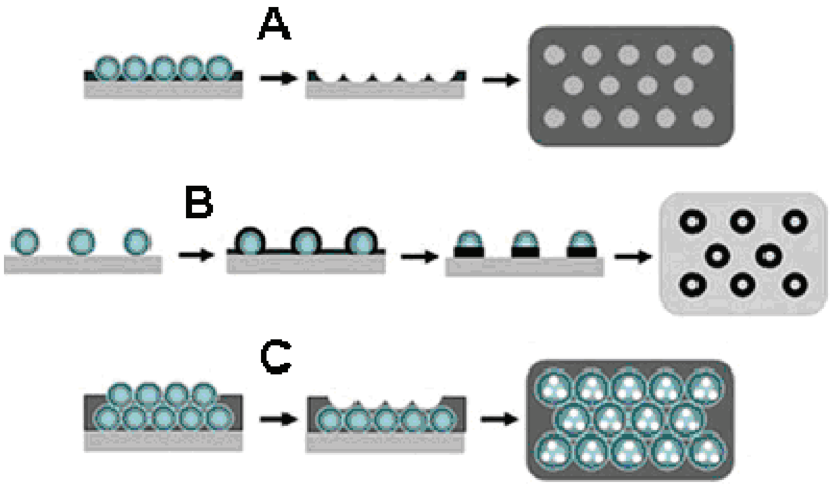

Figure 3.4: Typical nanofabrication routes of CL [19]

3.8 Protein immobilization

Fluorescein isothiocyanate–labeled albumin (FITC-albumin powder, Sigma) was purchased as powder and used as received after dissolving in 0.01 M phosphate buffer saline solution containing 0.003 M KCl and 0.14 M NaCl (PBS, pH 7.4 at 25 °C, Sigma).

As indicated by the supplier, the chromophore is coupled to the protein through the ε-amino group of lysines of the albumin, and the labeling density corresponds to a degree of substitution of 7 – 12 moles of FITC per mole of albumin. The protein was immobilized on the ZnO-based films by spontaneous adsorption from 100 µg/mL solution in PBS (40 min incubation time), followed by gentle rinsing with PBS and drying by dewetting in controlled laboratory atmosphere. No sodium peak was observed by XPS analysis, therefore the results for the ZnO surfaces immersed in buffer were essentially the same as those for the sample immersed in water. This indicates that the method used to wash the protein was sufficient to remove any non-adsorbed material from the ZnO substrate.

The fluorescence signal–enhancing capability of ZnO-based films was assessed *in situ* by using an experimental configuration consisting of the substrates in contact with the protein solution (50 μL drop) during an established incubation time (40 min), thus rinsing with PBS to remove unbound protein molecules.

3.9 Characterisation Techniques

The characterization of structural and optical properties was performed by Scanning Electron Microscopy (SEM), Atomic Force Microscopy (AFM), X-ray Diffraction (XRD), X-ray Photoelectron Spectroscopy (XPS), Energy - dispersive x-ray analysis (EDX), UV-vis spectroscopy, Cathodoluminescence (CL), Photoluminescence (PL), Transmission electron microscopy (TEM).

The interaction of ZnO surfaces with proteins was studied by confocal microscopy and fluorescence recovery after photobleaching techniques (FRAP).

3.9.1 Scanning Electron Microscopy

Scanning electron microscopy (SEM) is a versatile electron microscopy technique used for the examination and analysis of the microstructural characteristics of solid objects. SEM uses high-energy beam of electrons interacting with the atoms that make up the sample producing signals providing information about the sample's surface topography, chemical composition, crystalline structure and orientation of sample material.

In principle, a beam of electrons is thermionically emitted at the top of the microscope by heating of a metallic filament (Fig. 3.5). The electron beam having energy up to 40 KeV follows a vertical path through the column of the microscope electromagnetic lenses which focus and direct the beam down towards the sample. The types of signals produced by an SEM normally include secondary electrons, back-scattered electrons, characteristic X-rays, but may also include light, specimen current and transmitted electrons depending on the detectors used. Detector collect ejected electrons and convert them to a viewing screen producing an image [20].

The SEM instrument used to characterise the ZnO samples herein presented is a Field Emission SEM (FE-SEM), thus representing an advance with respect to the standard SEM. Thermionic sources have relative low brightness, evaporation of cathode material and thermal drift during operation. Field Emis-

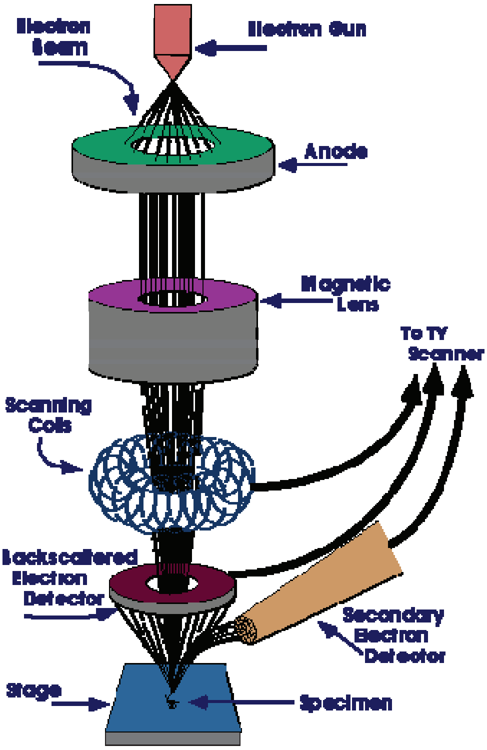

Figure 3.5: Schematic representation of scanning electron microscope (Reprinted from [20])

sion is one way of generating electrons to avoid these problems. A Field Emission Source (FES), also called a cold cathode field emitter, does not heat the filament. The emission is reached by placing the filament in a huge electrical potential gradient. The FES is usually a wire of Tungsten (W) fashioned into a sharp point. The significance of the small tip radius (~ 100 nm) is that an electric field can be concentrated to an extreme level, becoming so big that the work function of the material is lowered and electrons can leave the cathode. FE-SEM uses Field Emission Source producing a cleaner image, less electrostatic distortions and spatial resolution < 2nm (that means 3 or 6 times better than SEM). A voltage (1 ~ 30 KV), called the accelerating voltage, between the cathode and the second anode increases the beam energy and determines the velocity at which the electrons move into the column. This voltage combined with the beam diameter determines the resolution (capacity to resolves two closely spaced point as two separates entities). As voltage increases, better point-to-point resolution can be reached.

Herein, morphologies of the seed layers, polystyrene masks employed for the growth of ZnO, as-grown ZnO thin films and nanostructured arrays, TiO_2 nanofibers and TiO_2 - ZnO core-shell nanostructures were investigated using a LEO Supra 55VP field emission scanning electron microscope (FE-SEM).

3.9.2 Energy-Dispersive X-ray Analysis

Energy dispersive X-ray analysis is an analytical technique used for qualitative and quantitative elemental analysis or chemical characterisation of the interfaces and interlayers, with high lateral resolution [21]. It is most commonly used in conjunction with SEM. When the sample is bombarded by the SEM's electron beam, electrons are ejected from the atoms comprising the sample's surface. The resulting electron vacancies are filled by electrons from a higher state, and an x-ray is emitted to balance the energy difference between the two electrons' states. The x-ray energy is characteristic of the element from which it was emitted.

The EDX x-ray detector measures the relative abundance of emitted x-rays versus their energy. The detector is typically a lithium-drifted silicon, solid-state device. When an incident x-ray strikes the detector, it creates a charge pulse that is proportional to the energy of the x-ray. The charge pulse is converted to a voltage pulse (which remains proportional to the x-ray energy) by a charge-sensitive preamplifier. The signal is then sent to a multichannel analyzer where the pulses are sorted by voltage. The energy, as determined from the voltage measurement, for each incident x-ray is sent to a computer for display and further data evaluation. The spectrum of x-ray energy versus counts is evaluated to determine the elemental composition of the sampled volume [22].

In this work, the atomic composition of the as-deposited TiO_2 nanofibers has been analyzed by EDX using a windowless Oxford INCA Energy solid state detector. The use of the “windowless” EDX detector allowed the detection of the O Kα peak at 0.560 KeV.

3.9.3 Atomic Force Microscopy

Atomic force microscope is a high resolution scanning probe microscopy. In principle, in AFM experiment an atomically sharp tip is scanned over a surface with feedback mechanisms that enable the piezo-electric scanners to maintain the tip at a constant force (to obtain height information), or height (to obtain force information) above the sample surface [22-24].

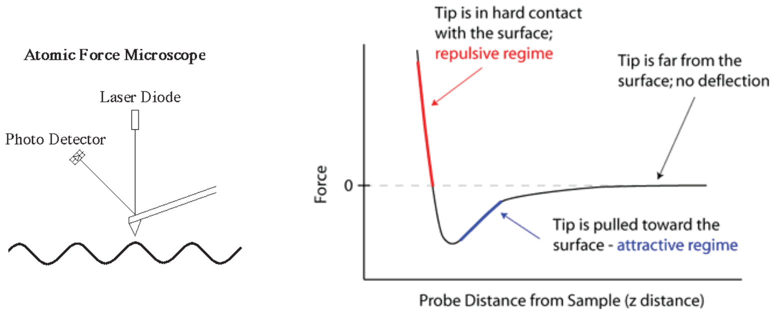

Figure 3.6: Brief scheme of how AFM works (left) and forces vs Z distance (right)

The nanoscope AFM head employs an optical detection system in which the tip is attached to the underside of a reflective cantilever (Fig. 3.6). A diode laser is focused onto the back of a reflective cantilever. As the tip scans the surface of the sample, moving up and down with the contour of the surface, the laser beam is deflected off the attached cantilever into a dual element photodiode. The photodetector measures the difference in light intensities between the upper and lower photodetectors, and then converts to voltage. Feedback from the photodiode difference signal, through software control from the computer, enables the tip to maintain either a constant force or constant height above the sample. In the constant force mode the piezo-electric transducer monitors real time height deviation. In the constant height mode the deflection force on the sample is recorded. The latter mode of operation requires calibration parameters of the scanning tip to be inserted in the sensitivity of the AFM head during force calibration of the microscope.

Because the atomic force microscope relies on the forces between the tip and sample, knowing these forces is important for proper imaging. The force is not measured directly, but calculated by measuring the deflection of the lever, and knowing the stiffness of the cantilever. Hook’s law gives

$$F = -kz, \qquad (3.4)$$

where F is the force, k is the stiffness of the lever, and z is the distance the lever is bent. According to the interaction of the tip and the sample surface, the AFM can be classified as repulsive or Contact mode, tapping, and attractive or Non-contact mode (Fig. 3.6).

Atomic force microscopy (AFM) images have been obtained in high amplitude tapping mode in air with an NT-MTD instrument. Golden silicon probes (NT-MTD) with a nominal resonant frequency of 190–325 kHz have been employed. The root mean-square roughness determined by AFM has been calculated from (5×5) μm^2 area.

3.9.4 X-ray Diffraction

X-ray diffraction is a non-destructive technique that reveals the information about the chemical composition, crystal structure and preferred orientation of the material.

X-rays are high-energy electromagnetic radiation having energies ranging from 200 eV to 1 MeV. If a beam of x-ray incidents an atom, the electrons in the atom absorb and reemit electromagnetic radiation. This process is known as scattering. Scattering which occurs without the energy loss is called elastic. On the other hand, if there is energy loss between the incident and emitted photon, such scattering is called inelastic. In materials with a crystalline structure, x-rays scattered by ordered features will be scattered coherently "in-phase" in certain directions meeting the criteria for constructive interference [25].

The conditions required for constructive interference are determined by Bragg's law. When the parallel planes of atoms reflect the incident beam of x-rays as shown in Fig. 3.7 the reflected rays interfere constructively and produce the maximum intensity [26].

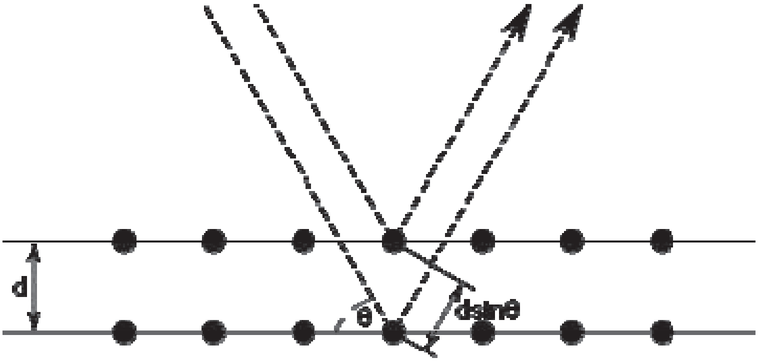

Figure 3.7: Bragg's reflections

The path difference between two reflected rays is $2d\sin\theta$, where d is the inter-planar spacing and and θ is the angle between the incident beam and the crystal plane. The constructive interference occurs when

$$2d\sin\theta = n\lambda, \qquad (3.5)$$

where n=0,1,2,… This is known as Bragg's law. The Bragg's reflection and diffraction patterns are possible because inter-planar spacing and wavelength of X-rays is of the same order (i.e. few angstroms).

Herein, X-ray diffraction (XRD) patterns were recorded with a Bruker-AXS D5005 θ-2θ X-ray diffractometer, using Cu K_α radiation operating at 40 kV and 30 mA in locked coupled and detector scan modes. The data were collected at room temperature with a step size 0.02° and a counting time of 0.02 s/step.

3.9.5 X-ray Photoelectron Spectroscopy

X-ray photoelectron spectroscopy (XPS) is one of the most widely used surface analytical technique. Based on photo-ionization and analysis of the kinetic energy distribution of the emitted photoelectrons XPS allows to study the composition and electronic state of the surface region of a sample [27]. In XPS, excitation by X-rays allows core (and valence) atomic levels to be probed, and the resultant chemical shifts provide an indication of the oxidation state of the material in the surface.

Photoelectron spectroscopy is based upon a single photon in/electron out process and from many viewpoints this underlying process is a much simpler phenomenon than the Auger process. The energy of a photon of all types of electromagnetic radiation is given by the Einstein relation:

$$E = h\,v\,, \qquad (3.6)$$

where h - Planck constant (6.62 x 10^{-34} J s) and v - frequency (Hz) of the radiation.

Photoelectron spectroscopy uses monochromatic sources of radiation (i.e. photons of fixed energy). In XPS the photon is absorbed by an atom in a molecule or solid, leading to ionization and the emission of a core (inner shell) electron. The kinetic energy distribution of the emitted photoelectrons (i.e. the number of emitted photoelectrons as a function of their kinetic energy) can be measured using any appropriate electron energy analyser and a photoelectron spectrum can thus be recorded.

The process of photo-ionization can be considered in several ways: one way is to look at the overall process as follows:

$$A + h\nu \rightarrow A^{+} + e^{-}, \qquad (3.7)$$

Conservation of energy then requires that:

$$E(A) + h\nu = E(A^{+}) + E(e^{-}), \qquad (3.8)$$

Since the electron's energy is present solely as kinetic energy (KE) this can be rearranged to give the following expression for the KE of the photoelectron:

$$KE = h\nu - (E(A^{+}) - E(A)), \qquad (3.9)$$

The final term in brackets, representing the difference in energy between the ionized and neutral atoms, is generally called the binding energy (BE) of the electron - this then leads to the following commonly quoted equation:

$$KE = h\nu - BE \qquad (3.10)$$

An alternative approach is to consider a one-electron model along the lines of the following pictorial representation; this model of the process has the benefit of simplicity but it can be rather misleading. The BE is now taken to be a direct measure of the energy required to just remove the electron concerned from its initial level to the vacuum level and the KE of the photoelectron is again given by:

$$KE = h\nu - BE \qquad (3.11)$$

Must be noted that the binding energies (BE) of energy levels in solids are conventionally measured with respect to the Fermi level of the solid, rather than the vacuum level. The Fermi level is determined to be at the point where the electron emission goes to zero. This point in the spectrum stays fixed independent of sample measured, and the X-ray photoelectron spectrum may directly recorded as function of binding energy. For each and every element, there will be a characteristic binding energy associated with each core atomic orbital, i.e. each element will give rise to a characteristic set of peaks in the photoelectron spectrum at kinetic energies determined by the photon energy and the respective binding energies. The presence of peaks at particular energies therefore indicates the presence of a specific element in the sample under study - furthermore, the intensity of the peaks is related to the concentration of the element within the sampled region. Thus, the technique provides a quantitative analysis of the surface composition [28].

The X-ray photoelectron experiments (XPS) have been carried out with a base pressure of 2×10^{-10} Torr using a PHI ESCA/SAM 5600 Multi technique spectrometer. A monochromatic Al K radiation source (hν=1486.6 eV) has been used.

The surface analysis of ZnO films has been conducted by acquiring both survey and narrow region scans at pass energies respectively of 187 eV and 11 eV, with an incremental step size of 1 eV for survey scans and 0.05 eV for the narrow scans, and a 0.8 mm slit width. Spectra have been acquired at a takeoff angle of 45° with respect to the samples surface. XPS spectra were collected at a photoelectron take-off angle of 45°, which, according to the effective attenuation length values, respectively, of 0.74 nm, for photoelectron from Zn 2p traveling in ZnO [29], and of 3.13 nm, for Si 2p photoelectrons in an organic layer [30], roughly corresponds to an actual sampling depth in the range from about 1.6 nm (bulk ZnO) up to about 6.4 nm (bulk SiO_2). Both survey and narrow region scans were recorded, namely Zn 2p, C 1s, Si 2p, O 1s and N 1s peaks, at pass energy and incremental step size of 150 eV/1 eV for survey and 11.85 eV/0.05 eV for the narrow scans, respectively.

The surface analysis of ZnO/TiO_2 nanofibers was conducted by acquiring both survey and narrow region scans of Zn 2p, C 1s, Ti 2p, O 1s and C 1s at 150 eV pass energy, with an incremental step size of 1 eV for survey scans and 0.05 eV for the narrow scans, and a 0.8 mm slit width.

The samples were sufficiently conducting that it was not necessary to supply electrons for charge compensation. The XPS signals were analysed by using a peak synthesis program in which a nonlinear background is assumed and the fitting peaks of the experimental curve are defined by a combination of gaussian (80%) and lorentzian (20%) distributions. All binding energies were referenced to C 1s neutral carbon peak at 285 eV. The atomic compositions were evaluated using sensitivity factors as provided by F V5.4A software.

3.9.6 Transmission Electron Microscopy

Transmission Electron Microscopy (TEM) is a technique which allows the crystallographic and chemical characterization of materials with high spatial resolution of 1 nm or better, allowing direct identification the chemistry of a single nanocrystal [31]. TEM is unique for characterizing the in situ structural evolution of nanocrystals resulting from annealing, electric field, or mechanical stress, such as imaging a single carbon nanotube when a mechanical or electrical measurement is being carried out in situ.

A modern TEM is composed of an illumination system, a specimen stage, an objective lens system, the magnification system, the data recording system(s), and the chemical analysis system. In TEM electrons are emitted in the electron gun by thermionic, Schottky, or filed emission [32]. A three- or four- stage condenser – lens system permits variation of the illumination aperture and the area of the specimen illuminated. The electron-intensity distribution behind the specimen is imaged with a lens system, composed of three to eight lenses, onto a fluorescent screen. The image can be recorded by direct exposure of a photographic emulsion or an image plate inside the vacuum, or digitally via a fluorescent screen coupled by a fiber optic plate to a camera.

Electrons interact strongly with atoms by elastic and inelastic scattering. Therefore, very thin (5 – 100 nm for 100 keV electrons) samples are required.

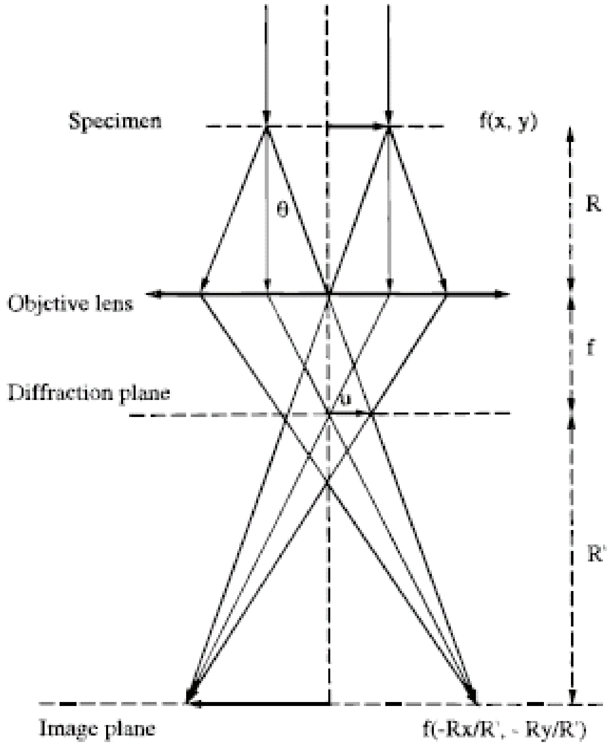

Figure 3.8: One lens Transmission electron microscope (Reprinted from [31])

For illustration, a TEM is simplified into a single lens microscope, as given in Figure 3.8, in which only a single objective lens is considered for imaging and the intermediate lenses and projection lenses are omitted. The entrance surface of a thin foil specimen is illuminated by a parallel or nearly parallel electron beam. The electron beam is diffracted by the lattices of the crystal, forming the Bragg beams which are propagating along different directions. The electron-specimen interaction results in phase and amplitude changes in the electron wave that are determined by quantum mechanical diffraction theory. For a thin specimen and high-energy electrons, the transmitted wave function ¾(x,y) at the exit face of the specimen can be assumed to be composed of a forward-scattered wave. The exit wave ¾(x,y) contains the full structural information on the specimen. Unfortunately, this wave will be transmitted nonlinearly by the optic system.

The nonlinear-axis propagation of the electrons through the objective lens is the main source of nonlinear information transfer in TEM. The diffracted beams will be focused in the back focal plane, where an objective aperture could be applied.

An ideal thin lens brings the parallel transmitted waves to a focus on the axis in the back focal plane. Waves leaving the specimen in the same direction (or angle θ with the optic axis) are brought together at a point on the back focal plane, forming a diffraction pattern. The electrons scattered to angle θ experience a phase shift introduced by the spherical aberration and the defocus of the lens, and this phase shift is a function of the scattering angle. The phase shift due to spherical aberration is caused by a change in focal length as a function of the electron scattering angle, and the phase shift owing to defocus is caused by the spherical characteristics of the emitted wave in free space (e.g., the Huygens principle).

A high-resolution TEM image of a crystalline specimen is formed by the interference of the Bragg reflected beams. Since the phase of each Bragg beam is perturbed by the phase shift induced by spherical and defocus, the object information will be transmitted nonlinearly [32]. Contrast and resolution of the image are obtained by elastically scattered electrons.

The elemental chemical distribution was investigated by energy filtered TEM (EF-TEM) analysis by the three windows method using the L edges for the Ti and Zn, and the K edge for O, respectively, using a TEM JEOL 2010 F instrument.

3.9.7 Photoluminecence Spectroscopy

Photoluminescence is the re-emission of light by interband luminescence after a direct gap semiconductor has been excited by a photon energy greater than the photon energy corresponding to the adsorption edge (E_g). Photoluminescence can be used for band gap determination, to determine impurity levels and defects, to study recombination mechanisms and to measure the material quality [33].

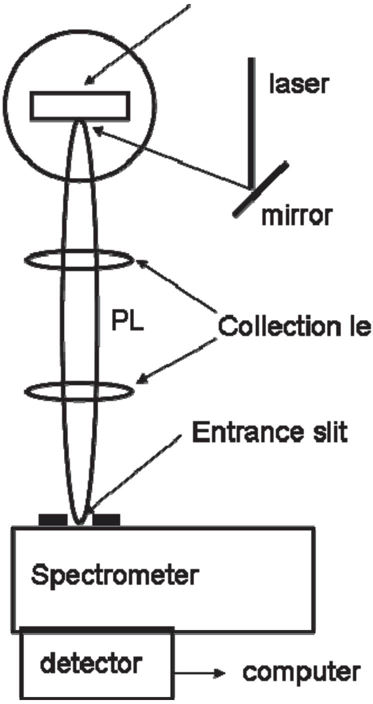

Figure 3.9: Schematic photoluminescence setup (Reprinted from [33])

In a typical photoluminescence setup (Fig. 3.9) the sample is placed in a variable temperature cryostat (room temperature in our case) and is illuminated with a laser or bright lamp with photon energy greater than the E_g. The luminescence is emitted at lower frequencies and in all directions. A portion is collected with a lens and focused onto the entrance slit of a spectrometer. The spectrum is recorded by scanning the spectrometer and measuring the intensity at catch wavelength with a sensitive detector such as a photomultiplier tube. Alternatively, the whole spectrum is recorded at once by using an array of detectors such as a charge-coupled device [33].

Room temperature photoluminescence (PL) measurements have been performed using a 325 nm He-Cd laser with a 2.5 W/cm incident power density. The PL spectra have been recorded with a monochromator fitted with 1800 grooves/mm grating and a photomultiplier tube.

3.9.8 UV-vis Absorption Spectroscopy

Ultraviolet-visible spectroscopy or ultraviolet-visible spectrophotometry (UV-vis or UV/Vis) refers to absorption spectroscopy or reflectance spectroscopy in the ultraviolet-visible spectral region.

When a beam of monochromatic light passes through a transparent medium, part of the light is absorbed and the transmitted beam has a lower intensity than the intensity of the incident beam [34]. The fraction of radiant energy transmitted by a given thickness of the absorbing medium is independent of the intensity of the incident radiation, provided that the radiation does not alter the physical or chemical state of the medium.

Let *I* be the intensity of a parallel beam of monochromatic light of wavelength λ, passing through a layer thickness d*l* of an absorbing material. The change in intensity d*I*, is given by

$$dI = -k_\lambda \cdot I \cdot dl \qquad (3.12)$$

where k_λ is a wavelength dependent proportionally constant. The negative sign is required because *I* becomes smaller as *l* becomes larger. Rearranging the above written equation and integrating it between limits I_0 and *I*, for *l* between 0 and l:

$$\log_{10}\frac{I_0}{I} = \frac{k_\lambda \cdot l}{2.303} \qquad (3.13)$$

where $\log_{10}\frac{I_0}{I}$ is called absorbance (A), $\frac{I_0}{I}$ is called transmittance (T).

Therefore the absorbance A is related to the transmittance T as

$$\mathrm{A} = \log_{10} T \qquad (3.14)$$

The typical UV-vis spectrophotometer consists of a light source, a monochromator and a detector [35]. The light sources are a deuterium and tungsten lamps, which emits electromagnetic radiation in the ultraviolet and visible region of the spectrum respectively. The monochromator is a diffraction grating used to spread the beam of light into its component wavelengths. A system of slits focuses the desired wavelength on the sample cell. Light from the slit then falls onto a rotating disc. Each disc consists of different segments – an opaque black section, a transparent section and a mirrored section. If the light hits the transparent section, it will go straight through the sample cell, get reflected by a mirror, hits the mirrored section of a second rotating disc, and then collected by the detector. Else if the light hits the mirrored section, gets reflected by a mirror, passes through the reference cell, hits the transparent section of a second rotating disc and then collected by the detector. Finally if the light hits the black opaque section, it is blocked and no light passes through the instrument, thus enabling the system to make corrections for any current generated by the detector in the absence of light. The light passes through the sample reaches the detector, which records the intensity of the transmitted light I. The detector is generally a photomultiplier tube or a photodiode. In a typical double-beam instrument, the light generated from the light source is split into two beams, the sample beam and the reference beam. When there is no sample cell in the reference beam, the detected light is taken to be equal to the intensity of light entering the sample I_0.

The transmission spectra were performed on a double-ray Jasco V-560 UV-vis spectrometer in the 200 and 800 nm range using a scan speed of 200 nm/min.

3.9.9 Cathodoluminescence

In cathodoluminescence (CL) light is emitted from a solid in response to excitation by electron beams cathode rays. CL is the contactless method allowing microcharacterization of the optical and electronic properties of luminescent material [36]. The CL signal is formed by detecting photons of the ultraviolet, visible, and near-infrared regions of the spectrum. These photons are emitted as the result of electronic transitions between the conduction and valence bands and levels lying in the band gap of the material.

In principle, the electrons in the e-beam are called primary electrons, have an energy which is determined by the applied voltage (1-100 kV). Due to the scattering of primary electrons high energy backs-scattered electrons are produced. These back scattered electrons are collected and used to form an image of the sample. The remaining electrons are scattered inelastically many times as they penetrate the crystal, and their direction gets randomized in the process. The region of the crystal that interacts with the e-beam is called the excitation volume, and the distance the beam travels is called the penetration depth. The penetration depth increases with increasing primary electron energy, and typically varies in the range 1-10 μm [33].

The electrons that penetrate the surface transfer their energy to the crystal by exciting electron-hole pairs. The number of electron-hole pairs generated per primary electron can be determined as follows:

$$N^{eh} = (1-\gamma)E^{p}/E^{i} \qquad (3.15)$$

where γ is the fractional energy loss due to back scattering, E^p is the energy of the primary electron, and E^i is the ionization energy. These electrons and holes are created high up in their bands, and emit photons in all directions with energy $h\nu \geq E_g$ after having relaxed to the bottom of their bands. It is these photons that comprise the cathodoluminescence signal.

Cathodoluminescence (CL) spectra have been excited with a field-emission gun in a conventional scanning electron microscope (FEG-SEM, SE-4300, Hitachi Co., Tokyo, Japan), equipped with a high-sensitivity CL detector unit (MP-32FE, Horiba Ltd., Kyoto, Japan). The CL experiments have been performed at 20 kV and 200 pA of probe current. The emitted CL spectrum has been analyzed using a monochromator equipped with a CCD camera. A new mapping device (PMT R943-02 Select, Horiba Ltd., Kyoto, Japan) has been used and related software has been developed to enable collection with nanometer - scale spatial resolution and to automatically analyze large numbers of CL spectra in nearly real time.

3.9.10 Confocal Fluorescence Microscopy and Fluorescence Recovery after Photobleaching

Confocal fluorescence microscopy (CFM) is one of the most powerful and popular tools in biomedical imaging applications [37]. It allows to obtain three-dimensional images of individual chromatographic support particles that directly illustrate the amount of protein uptake [38].

In fluorescence microscopy, naturally occurring autofluorescent molecules and introduced fluorophores targeted to cellular structures of interest are irradiated with high intensity light. When these molecules absorb a quantum of light, a valence electron is boosted up into a higher energy orbit, creating an excited state. When this electron returns to its original, lower energy orbit, termed the ground state, a quantum of light may be emitted. Absorption occurs only at wavelengths of light whose quantum energy is equivalent to the difference in energy between the ground electronic state and the excited state. Consequently, a given fluorescent molecule will have a discrete wavelength at which it will become excited; this is know as its excitation spectrum. Because fluorescence offers a pathway for a molecule to relax from an excited state back down to a non-excited state, it is known as a relaxation process. However, fluorescence is only one of a number of possible 'de-excitation pathways' available to molecules. One of the most fundamentally important of these is vibrational relaxation. The loss of some energy through vibrational relaxation means that less energy is available for emission as fluorescence. Because wavelength varies inversely to radiative energy, fluorescence emission is at a longer (i.e. lower energy) wavelength than the light used to excite it (Stokes Law).

In a confocal microscope detecting fluorescent light from the specimen the depth discriminating property can be used to carry out virtual sectioning of a specimen. First, light is focused by an objective lens into an hourglass/shaped beam so that the bright "waist" of the beam strikes one spot at some chosen depth in a specimen. Following by focusing the reflected or fluorescent light from that spot in a point and passing it through a pinhole aperture in a mask positioned in front of the detector, which effectively blocks light from out-of-focus planes. Finally the light is moved from point to point in the specimen until the entire plane of interest has been scanned [39].

One of the major uses of confocal microscopy is for fluorescence imaging. The fluorophores used tend to bleach out when exposed to too much light. Bleaching is generally thought to be proportional to light dose, although there are some examples of nonlinearities, both favourable and unfavourable to the high intensities of the laser-scanning confocal microscopes. Fluorophore saturation certainly occurs, and that limits the useful intensity, but bleaching is permanent, as is photodamage to biological structures.

There really is not much one can do about a process proportional to light dose, as the fluorescence has the same dependence, but one can avoid exposure to light that is not giving a fluorescent signal. That means not exposing the sample to light during "fly-back"--the time when the scanning engine is merely returning to zero. It also means avoiding exposure to one laser while another is being used. These are just points that a careful microscope builder pays attention to focal volume participates in the bleaching. All single photon microscopes expose the layers above and below the focal plane, even though they image only the focal plane. The advantage of the multiphoton microscope is clear and is one of the major reasons for using it.

Two distinct situations can occur during fluorescence imaging that lead to a decrease in fluorescence intensity, often referred to as fading. The first of these fading events is known as quenching. Fluorescence quenching is defined as a biomolecular process that reduces the quantum yield of a fluorophore without changing the fluorescence emission spectrum. It can be caused by oxidising agents, salts, heavy metals or halogen compounds as well as the transfer of energy from one fluorescent molecule to another one that is in close physical proximity. This transfer of energy is known as fluorescence resonance energy transfer. The other event that causes fading is photobleaching. In this case, high light intensity in the presence of molecular oxygen causes irreversible damage to the fluorophore and inhibits it from emitting light.

Fluorescence recovery after photobleaching (FRAP), also called (micro)photolysis, allows to determine translational diffusion coefficient of a fluorescent molecule by bleaching fluorescent molecules that move in the focal area of a light beam [40]. Immediately after the bleaching process, a highly attenuated light beam measures the recovery of the fluorescence in the bleached area due to the diffusion of fluorescent molecules from the surrounding unbleached areas into the bleached area (Fig. 3.10).

In practice, FRAP requires that a series of fluorescence intensity images are first collected to give a value for intensity in both the region of interest and the surrounding sample. Following this, a defined region of the sample is illuminated with high intensity light causing the fluorophore within that region to become photobleached. This creates a darker, bleached region, within the sample. Photobleached molecules are subsequently replaced by nonbleached molecules over time, and this results in an increase in fluorescence intensity in the bleach region. For a FRAP experiment to provide meaningful data, it is important that the sample is not photobleached during the prebleach or recovery phase of the experiment and that the camera is not saturated.

Recovery of fluorescence into the bleached area occurs as a result of the diffusional exchange between bleached and unbleached molecules. The fraction of fluorescent molecules that can participate in this exchange is referred to as the mobile fraction. The fraction of molecules that cannot exchange between bleached and nonbleached regions is called the immobile fraction. Knowledge of the rate of molecular exchange, elucidated by FRAP, can provide important insights into the properties and interactions of molecules within the cellular environment.

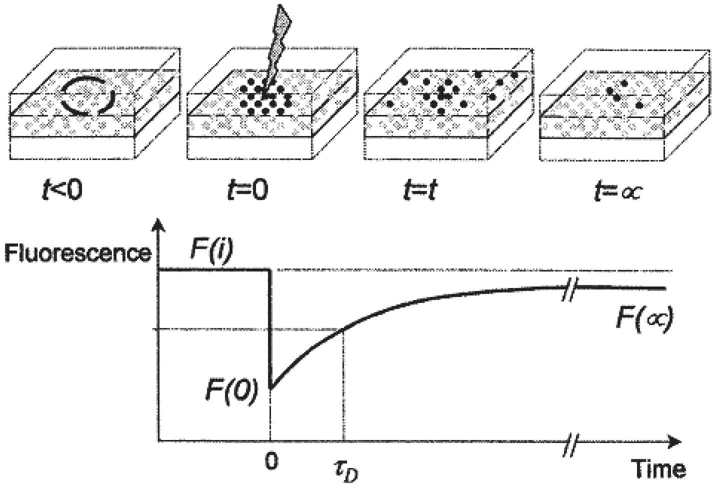

Figure 3.10: Schematical representation of FRAP experiment (Reprinted from [40])

The most common quantification method is to average the fluorescence intensity over the region of interest and plot it as a function of time. The “amount” of bleaching or degree of incomplete bleaching, the half time or time constant of recovery, and the immobile fraction can be determined as empirical parameters. They characterise the recovery, independent of the actual processes behind the redistribution of molecules. This is useful when only changes in mobility or binding properties are studied. In order to obtain the actual physical parameter of the processes involved, such as the diffusion coefficient, models must be applied that take into consideration Brownian motion, binding and immobilisation, cellular topology and the geometry of the region of interest. Axelrod et al. suggested an expression for the intensity recovering over time [41]. When recovery is dominated by diffusion the quantitative analysis yields the diffusion coefficient. The diffusion coefficient (D) of the fluorescent molecules can be derived from the recovery of the fluorescence in the bleached area. The diffusion coefficient:

$$D = (w^2/4\tau_{1/2})\cdot\gamma_F, \qquad (3.16)$$

where constant $\gamma_F \equiv \tau_{1/2}/\tau_D$ depends upon beam shape, type of transport and bleaching parameter K. For circular beams $\gamma_F = 0.88$, independent of K [41].

FRAP experiments are commonly performed on laser scanning microscopes, in which low laser power is used to image the sample in the pre- and post-bleach phases of the experiment. In the bleach phase, a region of interest is scanned at higher laser power to cause photobleaching. Temporal resolution may be improved if a wide-field system equipped with a laser for photobleaching is used.

Herein, the observations were carried out by using an Olympus FV1000 confocal laser scanning microscope (LSM) equipped with a diode Ar laser, oil immersion objective (60xO3 PLAPO) and spectral filtering system. Excitation wavelength was set at 488 nm, and emitted light was detected at 519 nm (micrographs) or in the spectral range 490 – 620 nm.

The detector gain was fixed at a constant value, and images were taken for all of the samples, at random locations throughout the area of protein adsorption as well as at the borderline between protein-exposed and bare surfaces, in order to compare quantitatively the fluorescence due to the antigen coverage and that to due background noise. The latter was analyzed to have control areas; therefore, the only difference between the control and target samples is the presence of protein.

The average fluorescence intensity was calculated by taking the mean pixel luminance intensity for all pixels within a 5 μm^2 area over at least 10 separate measurements. Intensity data were analyzed by one-way analysis of variance (ANOVA) with a Tukey – Kramer multiple comparisons test.

For the fluorescence recovery after photobleaching (FRAP) investigations, the data were normalized to the initial (pre-photobleach) value, which enables the percentage of photobleaching and the percentage fluorescence recovery within the laser region to be determined. For each sample,the emission recorded from the bleached spots was compared with that coming from contiguous non-bleached areas. Bare glass substrates were used for comparison. The samples were bleached for 1 min using high intensity (95% power) on the laser, immediately after a micrograph was taken every 1 min up to 10 min. By translating the sample stage, an average of 15 spots per substrate were photobleached in a given experiment.

References

1. G.Malandrino, M.Blandino, L.M.S. Perdicaro, I.L. Fragala, P.Rossi, and P. Dapporto, Inorg. Chem. 44 (2005) 9684-9689.
2. M. E. Fragala, G. Malandrino, and O.Puglisi, Chem. Mater. 12 (2000) 290-293.
3. A.C. Jones, M.L. Hitchman (Eds.), Chemical vapour deposition: precursors, processes and applications, RSC, 2008, 600 p.
4. N. Reschaner, U. Spreter, W. Brozia, A. Piehler, K.F. Rennk, Appl. Phys. Lett. 68 (1996) 1000-1002.
5. M.P. Siegal, E.L. Venturini, D.L. Overmeyer, P.P. Neweomer, J. Supercond. 11 (1998) 135-138.
6. E. Bauer, Z. Kristallogr. 110 (1958) 395-431.
7. F.C. Frank and H.J. van der Merwe, Proc. Roy. Soc. London, Ser. A 198 (1949) 205-216.
8. O.D. Pagni, On the MOCVD growth of ZnO, PhD Dissertation, University of Port Elizabeth, 2004.
9. I.N. Stranski and L. Krastanov, Sitzungsber. Akad. Wissenschaft Wien 146 (1938) 797-810.
10. M. Volmer and A. Weber, Z. Phys. Chem. 119 (1926) 277-310.
11. G. Malandrino, M. Blandino, M.E. Fragalà, M. Losurdo, and G. Bruno, J. Phys. Chem. C 112 (2008) 9595-9598.
12. D. Lincot and G. Hodes (Eds.), Chemical Solution Deposition of semiconducting and non-metallic films, Electrochemical Society, Pennignton, 2006, 235 p.
13. C.D. Lokhande, P.M. Gondkar, R.S. Mane, V.R. Shinde, S.H. Han, J. Alloys Compd. 475 (2009) 304-311.
14. Z. Burghard, L.Zini, P. Bellina, P.A. van Aken, and J. Bill, Nano Lett. 9 (2009) 4103-4108.
15. K. Govender, D. S. Boyle, P.B. Kenway and P. O'Brien, J. Mater. Chem. 14 (2004) 2575–2591.
16. S. Xu and Z.L. Wang, Nano Research 4 (2011) 1013-1098.
17. A. Greiner and J.H. Wendorff, Angew. Chem. Int. Ed. 46 (2007) 5670-5703.
18. J.C.Hulteen, D.A. Treichel, M.T. Smith, M.L. Duval, T.R. Jensen, and R.P. Van Duyne, J. Phys. Chem. B 103 (1999) 3854-3863.

19. S.-M. Yang,S.G. Jang,D.-G. Choi, S.Kim, H.K. Yu, Small 2 (2006) 458-475.
20. http://www.purdue.edu/rem/rs/sem.htm
21. G. Friedbacher, H. Bubert, H. Jenett (Eds.), Surface and Thin film Analysis: A compendium of principles, instrumentation, and applications,Wiley, 2011, 558 p.
22. L.D. Hanke (Eds.), Handbook of Analytical Methods of Materials, Materials Evaluation and Engineering, Inc., Plymouth, 2010, 54 p.
23. F.J. Giessibl, Rev. Mod. Phys. 75 (2003) 949–983.
24. P. Eaton and P. West (Eds.), Atomic Force Microscopy, Oxford University Press, 2010, 248 p.
25. C. Suryanarayana, M. Grant Norton X-Ray diffraction: a practical approach, Plenum Press, New York, 1998, 281 p.
26. P.V. Naik (Ed.), Principles of physics, 4th Ed., PHI Learning Private Ltd., New Dheli, 2010, 351 p.
27. P. v.d. Heide (Ed.), X-ray Photoelectron Spectroscopy: An introduction to principles and practices, John Wiley and Sons Inc., 2011, 256 p.
28. http://www.chem.qmul.ac.uk/surfaces/scc/scat5_3.htm
29. A.I. Martin-Conception, F. Yubero, J.P. Espinos, J. Garcia-Lopez, S. Tougaard, Surf. Interface Anal. 35 (2003) 984-990.
30. G.M.L. Messina, C. Satriano, G. Marletta, Colloids Surf., B 70 (2009) 76-83.
31. Z.L. Wang, J. Phys. Chem. B 104 (2000) 1153-1175.
32. D.L. Reimer, H. Kohl (Eds.), Transmission electron microscopy: physics of image formation, 5th ed., Springer, 590 p.
33. A.M. Fox (Ed.), Optical properties of solids, Oxford University Press, 2010, 396 p.
34. Di B. J. Clark,T. Frost,M. A. Russell (Eds.), UV spectroscopy: techniques, instrumentation, data handling, Chapman & Hall, London, 1993, 146 p.
35. D.L. Pavia, G.M. Lampman, G.S. Kriz, J.R.Vyvyan (Eds.), Introduction to spectroscopy, Brooks/Cole, 2009, 727 p.
36. B. G. Yacobi,D. B. Holt (Eds.), Cathodoluminescence microscopy of inorganic solids, Springer, 1990, 292 p.
37. D.M. Togashi, Colloids Surf., B 72 (2009) 219-229.
38. A. Subramanian, J. Hommerding, J. Chromatogr. B 818 (2005) 89–97.
39. A. Ljunglof, R.Hjorth, J. Chromatogr. A 743 (1996) 75-83.

40. T.K.L. Meyvis, S.C. De Smedt, P. Van Oostveldt, and J. Demeester, Pharmac. Res. 16 (1999) 1153-1162.
41. D. Axelrod, D.E. Koppel, J.Schlessinger, E.Elson, and W.W. Webb, Biophys. J. 16 (1976) 1055-1069.

4. Metal-Organic Chemical Vapor Deposition of ZnO

Introduction

ZnO has attracted considerable attention of scientific community in recent years due to its potential applications in piezoelectric, optoelectronic, catalytic, sensing devices and use in dye sensitizing solar cells [1-3]. Many research groups have tried to grow epitaxial ZnO films using various techniques in vapor phase or in solution. Among vapour phase approaches, vapor-solid (VS), vapor-liquid-solid (VLS) growth and metal-organic chemical vapor deposition (MOCVD) are the most commonly used techniques for ZnO film preparation [4-6].

MOCVD which follows a catalyst-free growth mechanism, which is preferred to reduce the impurity incorporation, represents an alternative to VLS growth. It is well known that, the success of an MOCVD process depends critically on the availability of volatile, thermally stable precursors that exhibit high and constant vapour pressure.

In particular, metal β-diketonates [$M(RCOCHCOR)_x$ (where R=alkyl, aryl etc)] have been widely used in the fabrication of metal oxide thin films, since among metal coordination compounds they are most volatile, thus present adequate characteristics in terms of mass transport properties [7]. Recently, novel diamine adduct of zinc bis-2 thenoyl-trifluoroacetonate ($Zn(tta)_2$·tmeda), where H-tta=$CF_3COCH_2COC_4H_3S$, tmeda=N,N,N′,N′ - tetramethylethylenediamine (Fig. 4.1) was reported for the MOCVD growth of ZnO [8-10]. This adduct has been chosen to be used as metal organic precursor due to its high stability, volatility, promoting high and stable vapor pressures with respect to commonly used precursor systems such as diethyl- and dimethyl- zinc, acetate-, alkoxide-, and acetylacetonate- zinc complexes normally used for ZnO deposition [11-16]. Moreover, this adduct was employed in MOCVD fabrication of transparent ZnO films using $Zn(tta)_2$·tmeda on various substrates including quartz, $SrTiO_3$ (100), Si (100) and Al_2O_3 (0001) was reported [9,10]. The films were deposited in the range of temperatures from 400 to 750 °C for 60 min in reduced pressure hot-wall MOCVD reactor keeping the Ar (150sccm) and O_2 (150 sccm) as carrier and reaction gases, respectively. Indeed, ZnO layers grown with this technique, under given growth conditions, polycrystalline films constituted of rounded grains having sizes ranging from 80 nm (at 400 °C) to 400 nm (at 750 °C) in size. Additionally, the crystallinity of the films was improved with increasing the substrate temperature.

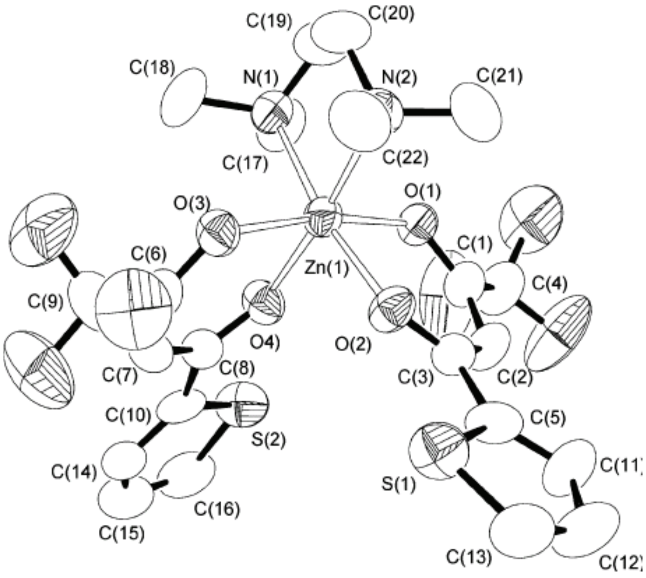

Figure 4.1: Chemical structure of diamine adduct of zinc bis-2 thenoyl-trifluoroacetonate ($Zn(tta)_2\cdot tmeda$) (Reprinted from [8])

In this Chapter, the morphology and properties of ZnO nanostructured layers obtained at “standard” deposition conditions by MOCVD using β-diketonate precursor are described. Special focus is put on the temperature and deposition time.

Results and Discussion

ZnO deposition has been performed on silicon substrates using a total gas flow of 500 sccm keeping an Ar/O_2 ratio of 1:1 (Ar/O_2 250/250 sccm). The substrate temperature has been maintained in the 600 - 700 °C range, and the deposition time was kept at 60 - 90 min.

In the MOCVD process, growth temperature is one of the most important factors affecting the high quality of ZnO material. The effect of growth temperature on crystalline properties was investigated using X-ray Diffraction. Figure 4.2 represents an XRD θ–2θ scans of ZnO film grown by an MOCVD process at substrate temperatures of 600 °C and 700 °C. Film deposited at 600 °C exhibits sharp diffraction peak at 34.42° that may be associated with the (002) reflection and small peaks observed at 36.25° that may be associated to (101) reflection and at 47.53° attributed to (102) reflection. With increasing the substrate temperature to 700 °C small peak at 31.77° associated with (100) reflection appears. In each case, the diffraction pattern is dominated by the (002) reflection of the wurtzitic phase (*P6₃mc*) [14].

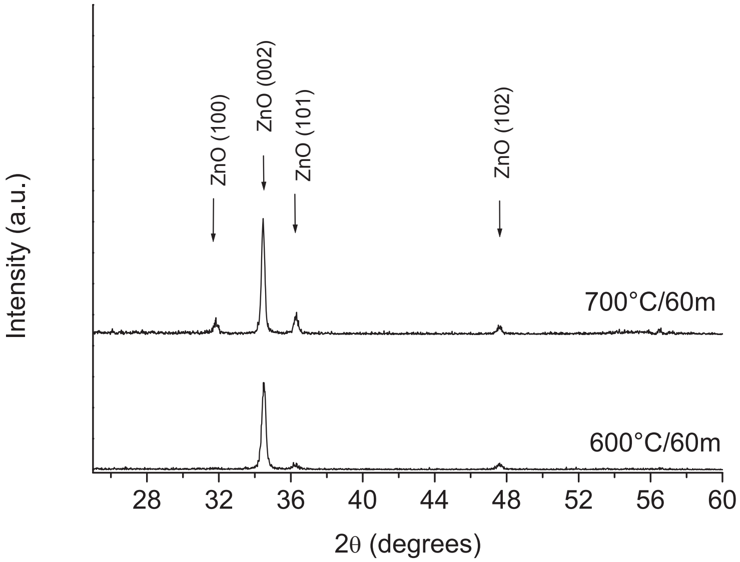

Figure 4.2: XRD patterns of ZnO deposited on silicon at T=600 and 700 °C for 60min

As growth temperature increased, the growth mode changed from kinetics-limited to mass-transfer-limited and the observation of the strong (002) peak indicates that the highly c-axis oriented film is grown. The films have other peaks, which may correspond to granular structure of the film. It has to be mentioned that at 700°C, the morphology of ZnO layer changes from nanostructured film to nanostructure (nanorods), thus explaining the contribution of the other growth directions in the XRD pattern.

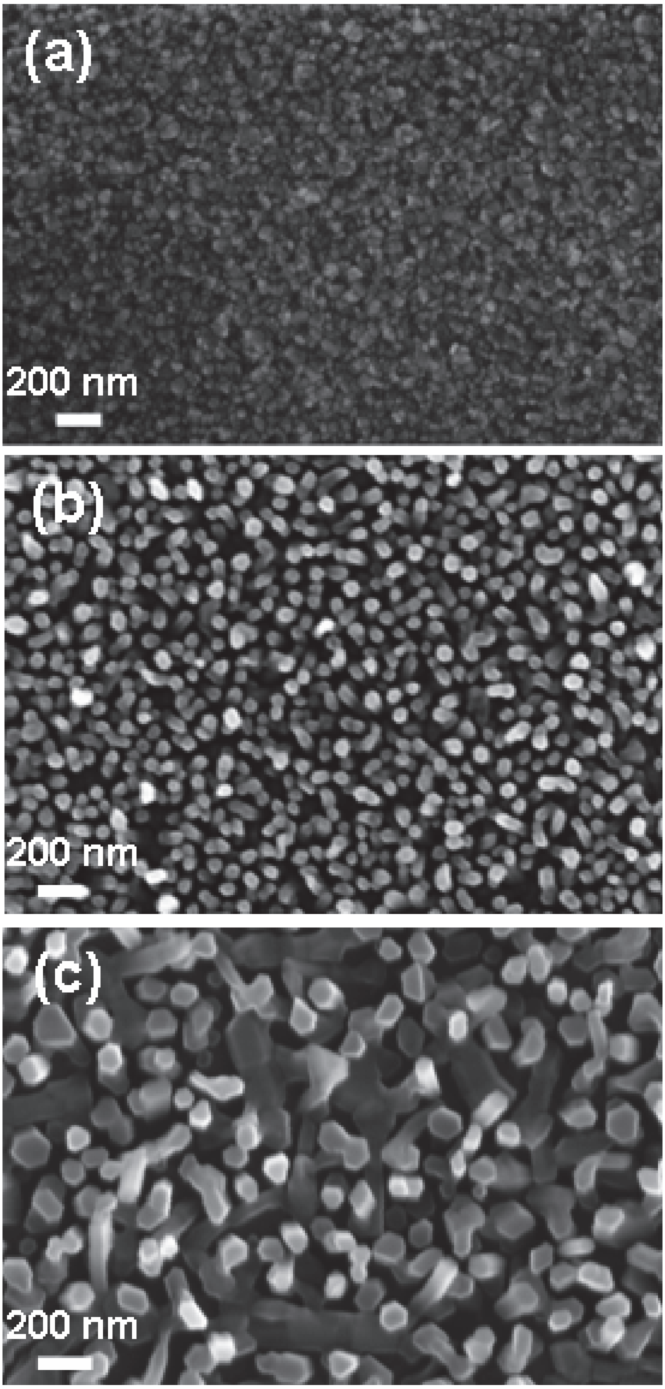

Figure 4.3: SEM top-view images of ZnO film deposited on Si at (a) 600 °C/60 min; (b) 600 °C/90 min; and (c) 700 °C/60 min

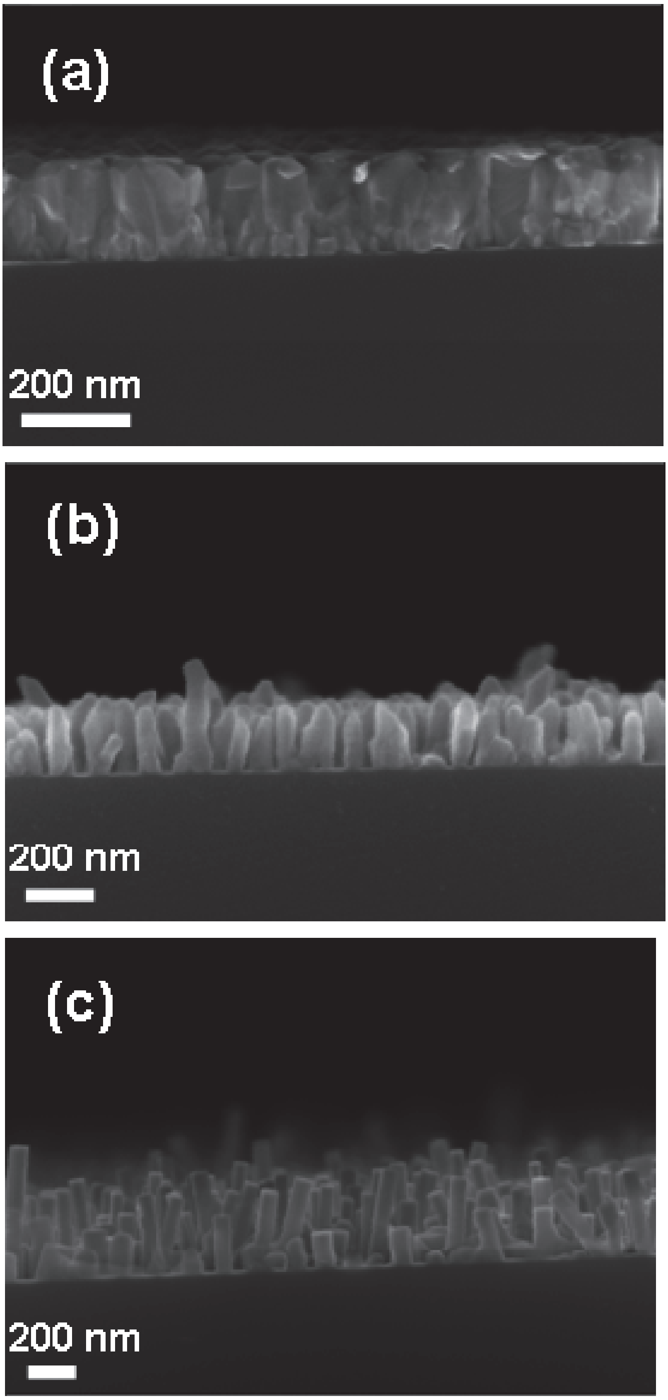

Figure 4.4: SEM cross-sectional view images of ZnO film deposited on Si at (a) 600 °C/60 min; (b) 600 °C/90 min; and (c) 700 °C/60 min.

SEM top-view images represent the morphology of as grown ZnO material (Fig. 4.3 (a-c)). The role of deposition temperature and time on the ZnO surface structure was studied. At deposition temperature 600 °C and shorter deposition time (60 m) continuous layer consisting round grain-like structures of ~ 80 - 120 nm in diameter is grown (Fig. 4.3 (a)). By changing the nucleation time, the morphology changes from continuous layer to nanorod formation (Fig.4.3 (b)) with the dimensions reduced to ~ 50 - 80 nm. Further increase of the deposition temperature to 700 °C keeping the growth time at 60 min resulted in formation of hexagonal rods with the diameters of ~ 120 - 150 nm. At the initial stage of growth, ZnO nano-crystallites are formed by random nucleation process, thus for high deposition rates and lower temperatures the growth is very close to the ideal 2D layer-by-layer growth mode, leading to a smoother surface morphology. When the growth temperature is increased the nano-crystals are elongated due to a higher growth rate along the c-axis direction, the three-dimensional (3D) growth begins to appear and becomes completely dominant when the temperature reaches 700 °C [17].

Figure 4.4 shows the cross-sectional SEM images of the ZnO layers deposited using $Zn(tta)_2$·tmeda were investigated over the temperature range 600 – 700 °C deposited for 90 and 60 min respectively. It is apparent that morphology and growth rate is critically dependant on chosen deposition regime. The growth rate of ZnO increases in the studied temperature range. Thus, at 600 °C, the growth rate is about ~ 200 nm per hour. With increase of the deposition time from 60 m (Fig. 4.4 (a,b)) to 90 min, the densely packed round grains start evolving into layer containing porous rod-like structures having length of ~ 300 nm with round tips. While, the increase of the substrate temperature to 700 °C and reducing the growth time to 60 min resulted in the formation of smooth rod like structures with hexagonal flat tops. However, it was found that the growth at high temperature (700 °C) was less uniform and produced rods having lengths of ~ 200 - 800 nm. In all the cases studied, the ZnO structures were vertically oriented. This finding matches well with XRD data.

The formation of ZnO nanostructures is dependent on the mobility of precursor species such on the substrate surface. It is a pre-requisite for the Zn adsorbate to have sufficient surface lifetime to migrate to the tip of the growing nanorod. The surface lifetime of an adsorbate molecule is determined by substrate temperature and its thermal stability [18].

From the data presented here, at lower substrate temperatures (i.e. 600 °C) and shorter deposition time (60 min) the Zn(tta)$_2$·tmeda species have insufficient surface mobility for nanorod growth, and incorporation at the growth surface occurs to yield a continuous film consisting of round grains (Fig. 4.5). By increasing the deposition time to 90 m the precursor complex has sufficient mobility and lifetime to allow efficient surface diffusion for the growth of ZnO rod-like structures. At higher temperatures (i.e. 700 °C), rapid decomposition of precursor occurs. This reduces the surface lifetime of the adsorbate, preventing surface diffusion and leading to the rapid deposition of ZnO rods.

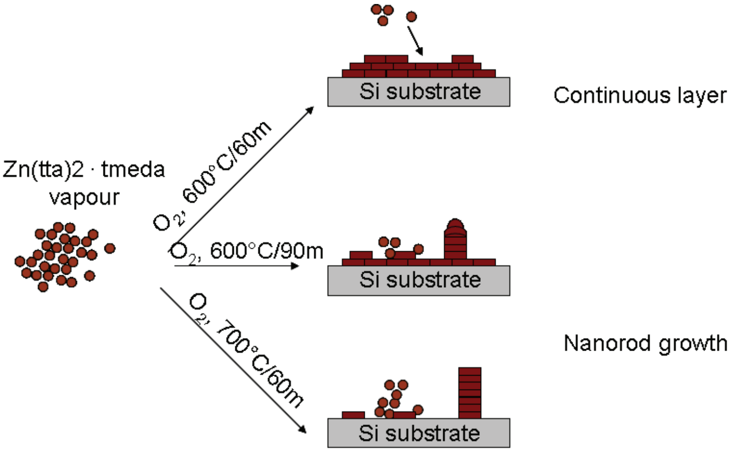

Figure 4.5: Scheme of time-temperature dependant ZnO growth mode

The deposited films are transparent. In particular, the transmission spectrum of a ZnO film grown on quartz at 600 °C is shown in Figure 4.6. This spectrum shows that ZnO films are highly transparent in the visible region (~ 90% between 400 and 800 nm).

To conclude, the growth of ZnO structures via MOCVD process employing β-diketonate adduct Zn(tta)$_2$·tmeda was demonstrated in the range of temperatures 600 – 700 °C. It was found deposition time and deposition temperature plays a crucial role in the formation of ZnO. Longer deposition time or high deposition temperature are required to promote the growth of 1D structures. This gives an insight to the production of high surface area ZnO nanomaterial that can be used in optical, piezoelectric and sensing technologies.

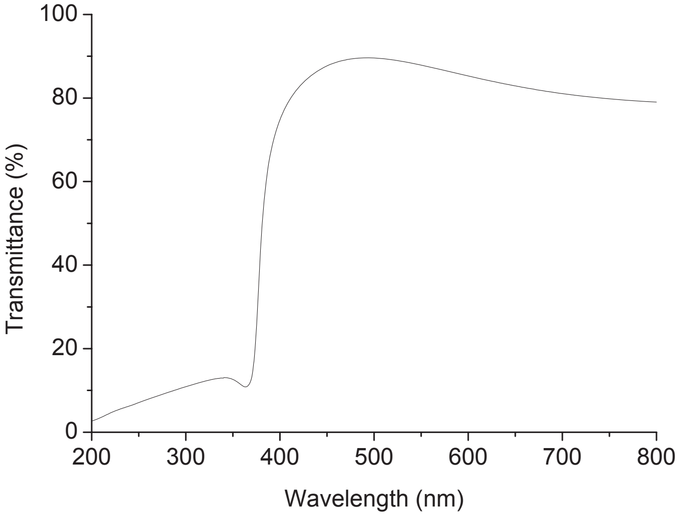

Figure 4.6: UV-visible transmission spectrum of ZnO film deposited at T=600 °C for 60m

References

1. C.F. Klingshirn,B.K. Meyer, A. Waag, A. Hoffmann, J.M.M. Geurts (Eds.), Zinc Oxide: From Fundamental Properties Towards Novel Applications, Springer, 2010, 300 p.
2. H. Morkoç, Ü. Özgür (Eds.), Zinc Oxide: Fundamentals, Materials and Device Technology, Wiley-VCH, 2009, 477 p.
3. C. Jagadish, S. J. Pearton (Eds.), Zinc Oxide bulk, thin films and nanostructures: processing, properties and applications, Elsevier, 2006, 589 p.
4. A. Umar, S.H. Kim, Y.-S. Lee, K.S. Nahm, Y.B. Hahn, J. Cryst. Growth, 282 (2005) 131-136.
5. Y.C. Kong, D.P. Yu, B. Zhang, W. Fang, and S.Q. Fen Appl. Phys. Lett. 78 (2001) 407-409.
6. J.L. Yang, S.J. An, W.I. Park, G.-C. Yi, W. Choi, Adv. Mater. 16 (2004) 1661-1664.
7. G.Malandrino, R.G. Toro, R. Lo Nigro, I.L. Fragalà, ECS Transactions 25 (2009) 125-134.
8. G. Malandrino,P. Rossi, M. Blandino,P.Dapporto, L. M. S. Perdicaro,I. L. Fragalà, Inorg. Chem. 44 (2005) 9684-9689.

9. A.A. Scalisi, R.G. Toro, G. Malandrino, M.E. Fragalà, G. Pezzotti, Chem. Vap. Deposition 14 (2008) 115–122.
10. G.Malandrino, M.Blandino, M.E.Fragalà, M. Losurdo, and G. Bruno J. Phys. Chem. C 112 (2008) 9595-9599.
11. S.T. Tan, B.J. Chen, X.W. Sun, W.J. Fan, H.S. Kwok, X.H. Zhang, S.J. Chua, J. Appl. Phys. 98 (2005) 013505.
12. F. Jiang, J. Dai, L. Wang, W. Fang, Y. Pu, Q. Wang, Z. Tang, J.Lumin. 122-123 (2007) 162-164.
13. F.A. Cotton, G. Wilkinson, C.A. Murillo, M. Bochmann (Eds.), Advanced Inorganic Chemistry, 6th ed.; Wiley-Interscience, New York, 1999, 1355 p.
14. S. Jain, T.T. Kodas, M. Hampden-Smith, Chem. Vap. Deposition 4 (1998) 51–59.
15. J. Auld, D.J. Houlton, A.C. Jones, S.A. Rushworth, M.A. Malik, P. O'Brien,G.W. Critchlow, J. Mater. Chem. 4 (1994) 1249– 1253.
16. H. Sato, T. Minami, T. Miyata, S. Takata, M. Ishii, Thin Solid Films 246 (1994) 65–70.
17. B.P. Zhang, K. Wakatsuki, N.T. Binh, N. Usami and Y. Segawa,Thin Solid Films 449 (2004) 12–19.
18. K. Black, P.R. Chalker, A.C. Jones, P.J. King, J.L. Roberts, and P.N. Hey, Chem. Vap. Deposition 16 (2010) 106–111.

5. Silver catalyst assisted Metal-Organic Chemical Vapor Deposition of ZnO nanostructures

Introduction

Controlled growth of metal oxide semiconductors has stimulated great interest in the research community due to their importance in basic scientific research and potential technological applications [1]. Recently, ZnO nanostructures have started to emerge as very promising nanoscale building blocks due to their outstanding properties, diverse functionalities and chemical/thermal stability [2,3].

On the other hand, the interest in developing multifunctional material aiming at enhancing the surface-to-volume ratio, exploring the novel opto-electrical properties and enabling high-density device integration is critically important. This has stimulated the realization of growth of ZnO nanostructured material using catalysts. In particular, ZnO nanowires and nanorods represent spatially controlled, highly functional nanostructures having remarkable physical and chemical properties [4-7]. Among the used synthetic strategies, catalyst-assisted growth of ZnO nanowires has been reported [8]. In this approach, metallic nanoparticles play a crucial role in nanowire growth and have profound consequences on nanowire morphology and their physical properties. Therefore, the metal selection is crucial to achieve the desired nanowire morphology and to avoid any potential detrimental contamination [9]. Catalyst particles, deposited on a substrate, act as a preferential sites for adsorption of vapor of the desired source material. The source material is adsorbed into the catalyst and once the catalyst particle becomes supersaturated, the excess source material precipitates out and a 1D nanostructure grows [10].

The growth of nanostructures using a catalyst and a vapor phase source is often described in terms of the vapor-liquid-solid (VLS) mechanism. Any unidirectional growth with a liquid mediating phase and precursors supplied from a vapor phase is considered to grow by the VLS growth mechanism. It involves the dissolution of growth species in a liquid catalyst droplet at the tip of the nanostructure, followed by precipitation and growth at the catalyst-nanowire interface.

The formation of catalyst droplets and its durability during the growth process avoiding oxidation or nitridization has become the leading interest. Different catalysts (e.g. Au, Sn, Pt, Ni) were reported to grow ZnO nanowires [11-13], among them Au [14,15] is the most used for ZnO nanowire growth. Recently, Zhang et al. have reported the change in morphology of ZnO nanostructures due to the introduction of silver into the system [16.] and shown that the silver itself directly influences the final grown morphology. Thus, silver can be used to specifically control the morphology of the grown ZnO to achieve a specific type of nanostructure. In fact, the use of Ag as alternative catalyst has the drawback of temperature limitation (up to 500 °C) related to fast Ag oxidation forming Ag_2O or AgO layer which results in low-quality nanowires [10]. For this reason Ag has been much less explored as a catalyst for the growth of ZnO nanostructures. Despite this, Ag has generally similar properties to Au in terms of the formation of nanoclusters from a melted thin film. Therefore, silver-based films have also been used for the growth of ZnO nanostructures. Panda and Jacob have reported on the sword-like growth of ZnO on annealed (200 °C) silver film at 800 °C on patterned and unpatterned Si wafers [17,18]. Li et al. studied vapor phase synthesis of ZnO material grown on silver nanoislands [19].

Generally, the route adopted for the catalyst assisted fabrication of metal oxide films implies a two-step process. In the first step, the catalyst layer is prepared, and successively, the metal oxide is deposited onto the film surface by different processes, such as vapour-solid growth, vapor–liquid–solid growth or chemical and metal organic vapour deposition [20-23].

Herein, the metal-organic silver compound has been chosen as a catalyst to promote ZnO growth via MOCVD process. To note, the nature of the silver precursor is of crucial importance and it must satisfy certain prerequisites such as clean decomposition pathways to metallic silver, low decomposition temperatures, and controlled oxidation. Moreover, it must be easily synthesized and purified allowing cost-effective procedures [24].

In this chapter the process optimization to tailor the growth of ZnO nanostructures with desired morphologies focusing on the relationship between initial concentrations of silver catalyst metal-organic precursor and ZnO metal-organic deposition (MOCVD) process parameters (temperature and time) is reported.

In particular the obtained results suggest the optimal experimental conditions for an effective colloidal lithography (NSCL) - MOCVD process integration as a valuable bottom up method to fabricate 2D ordered ZnO nanohole arrays.

A wide number of techniques has been developed for the fabrication of patterned nanoparticle arrays. Among these techniques, directed self-assembly of nanoparticles onto templated substrates has been well studied [25,26]. Typically, the templates are generated with lithographic techniques such as nanosphere colloidal lithography (NSCL), e-beam lithography, and nanoimprint lithography [27].

Nanosphere colloidal lithography is emerging as an effective and flexible approach where self-assembled 2D colloidal nanoparticles act as template or mask for producing 2D regular and nearly homogenous arrays of the desired materials. In particular, formation of self-assembled monolayer of PS nanospheres [28] is an effective bottom up approach to pattern materials [15,29]. Recently, Fragala et al. reported on a “bottom-up” approach to fabricate 2D periodic ZnO arrays through a hybrid method of nanosphere colloidal lithography and MOCVD, based on silver and platinum catalyst controlled ZnO growth [30].

The proposed hybrid approach represents a valuable bottom up method to fabricate 2D ordered ZnO nanohole arrays. The obtained results appear promising in the perspective of surface nanostructuring of metal oxide films in two-dimensional (2D) porous substrates as intriguing strategy for various applications including microelectronics, sensing, catalysis, optics and biomedical science and as templates for the growth of nanomaterials [31,32].

Results and discussion

Herein implemented adduct, Ag(hfa)·tetraglyme (Fig. 5.1), was synthesized from a tetrahydrofuran (THF) suspension of Ag_2O, at which two coordination ligands have been added, the 2,5,8,11,14-pentaoxatetradecane (tetraglyme) and the 1,1,1,5,5,5-hexafluoro-2,4-pentandione (H-hfa) [33].

The Ag(hfa)·tetraglyme adduct has been successfully applied to the deposition of both silver and silver containing polymer nanostructured thin films [24,33]. The catalyst deposition parameters and MOCVD parameters used in this work are presented in Table 5.1.

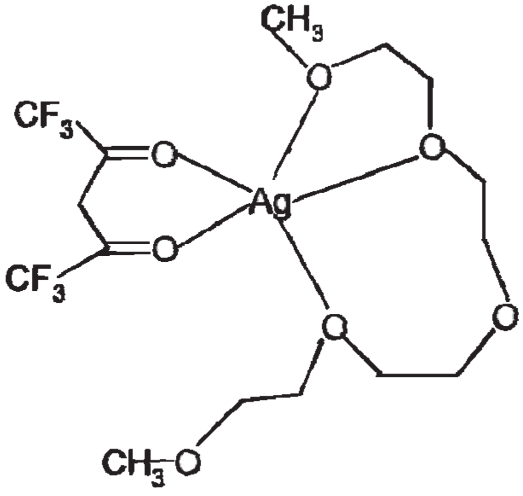

Figure 5.1: Chemical structure of Ag(hfa)tetraglyme adduct

Table 5.1: Deposition conditions employed for ZnO growth

C_{cat}, M	T_{ann}, °C	t_{ann}, m	T_d, °C	t_d, m
0.1	-	-	600	60
0.1	400	30	400	30
0.1	400	30	600	30
0.1	400	30	600	60
0.01	400	30	400	30
0.01	400	30	400	60

The seed layer was obtained by drop casting of Ag(hfa)·tetraglyme [24] ethanolic solutions onto Si substrates. The obtained precursor layer is shown in Fig. 5.2 (a). Annealing at 400 °C for 30 min in air was performed in order to decompose the precursor and reduce Ag^+ to metallic silver. The obtained nanostructured films are composed of discrete silver grains with average dimensions ranging from to 300 nm up to microns (Fig. 5.2 (b)) attributed to grains coalescence effect [34].

Figure 5.3 shows top-plane view of ZnO nanostructures deposited on not annealed and annealed silver catalyst layers. It is clearly seen that growth on not annealed catalyst layer resulted in bi-modal growth consisting of sparsely distributed ZnO nanobundles and small ZnO grains covering the catalyst grains (Fig. 5.3 (a)). On the other hand, ZnO grown on annealed catalyst layers resulted in the massive formation of ZnO wire-like structures (Fig. 5.3 (b)). Such different morphology can be attributed to a different silver grain agglomeration process induced by different annealing ramp rate and time. In fact, it is noteworthy that in both cases silver precursor layer undergoes an annealing treatment. In fact, during ZnO deposition, temperature ramps up from 25 °C (room temperature) to 600 °C in about 20 minutes (ramp rate 30 - 40 °C/min). During this time, the silver precursor is decomposed, reduced and melted. If the precursor layer is preliminary annealed before the ZnO deposition it experiences a second thermal treatment during MOCVD.

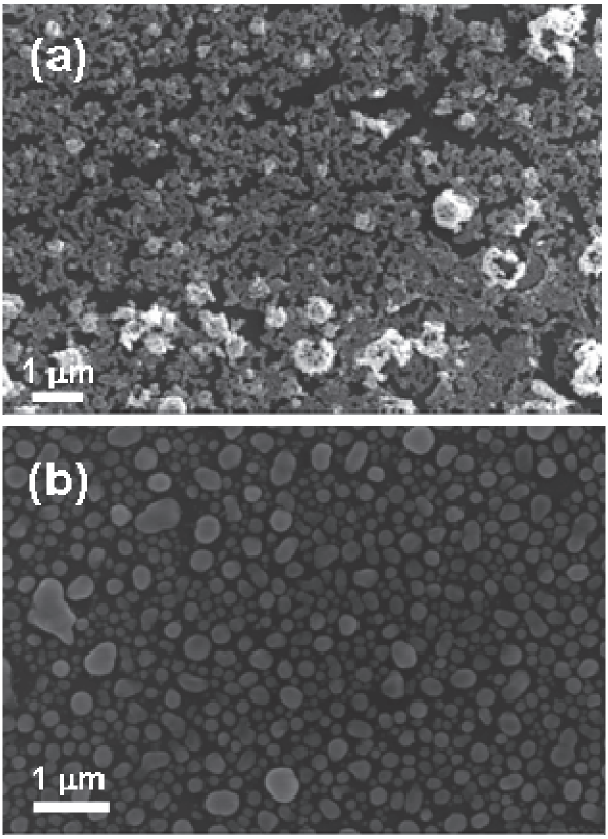

Figure 5.2: SEM images (a) not annealed and (b) annealed at 400 °C layer of of silver catalyst (0.1 M) deposited by drop casting on Si substrate

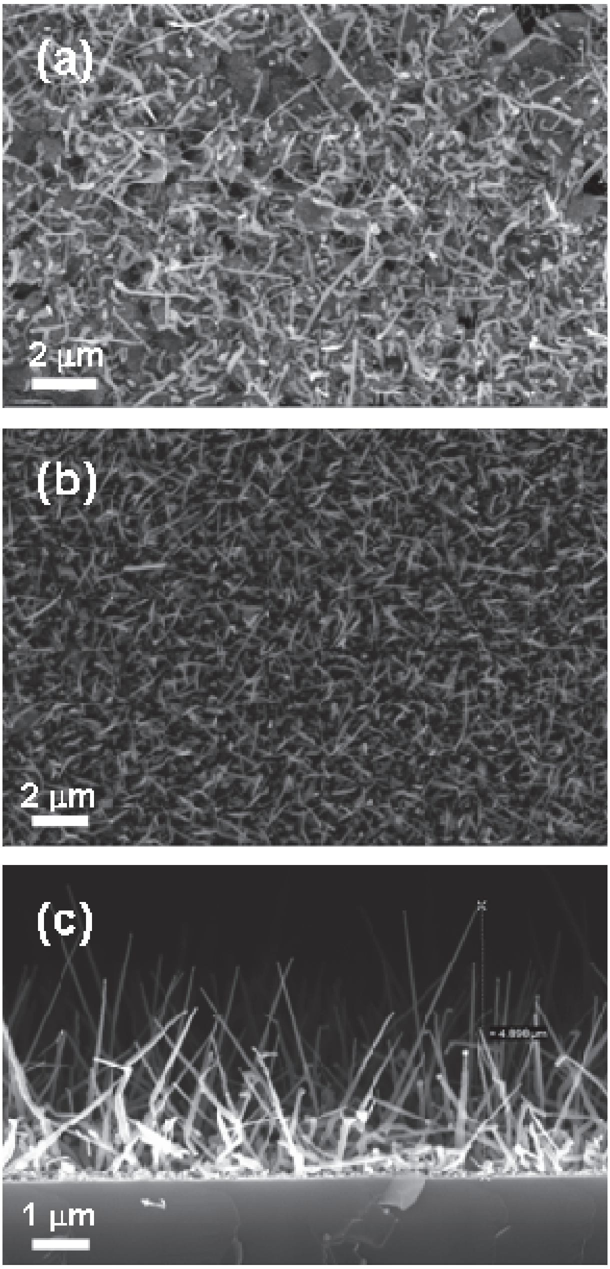

Figure 5.3: SEM images of ZnO grown by MOCVD at T=600 °C for 60 min on (a) not annealed (b) annealed at 400 °C layer of silver catalyst (0.1 M) deposited by drop casting on Si substrate and (c) cross-sectional image of ZnO grown by MOCVD at T=600 °C for 60 min on layer of silver catalyst (0.1M) layer deposited by drop casting on Si substrate (T_{ann}=400 °C)

The SEM cross-sectional image taken for the latter sample confirmed the catalytic role of Ag in the ZnO growth as the as grown wires were up to 6-8 µm in length and 80 – 120 nm in width (Fig. 5.3 (c)). This suggests that the growth rate is 30 times higher with respect to one reported for catalyst–free growth (~ 200 nm/h (see Chapter 4)).

The catalyst assisted growth mechanism is thus related to the formation of liquid droplet of the Ag-Zn alloy during the temperature ramp-up. The continued feeding of the precursor into the liquid droplet leads to supersaturation resulting in nucleation of the solid ZnO and related ZnO grows on the formed solid–liquid interface, thus explaining the alloy droplet on the top [35].

XRD patterns of the annealed seed layer and subsequently grown ZnO (600 °C/60 min) are presented in Fig. 5.4. Fig. 5.4 illustrates the XRD pattern of metallic silver films, which revealed that Bragg angle peaks located at $2\theta =$ 38.10° and 44.28° for drop casted Ag metallic films that can be assigned to the (111) and (200) reflection metallic silver cubic structure respectively (JCPDS#03-0931) and represent the main evidence of the crystalline quality of these films. Moreover, no significant Ag_2O formation is detected after annealing.

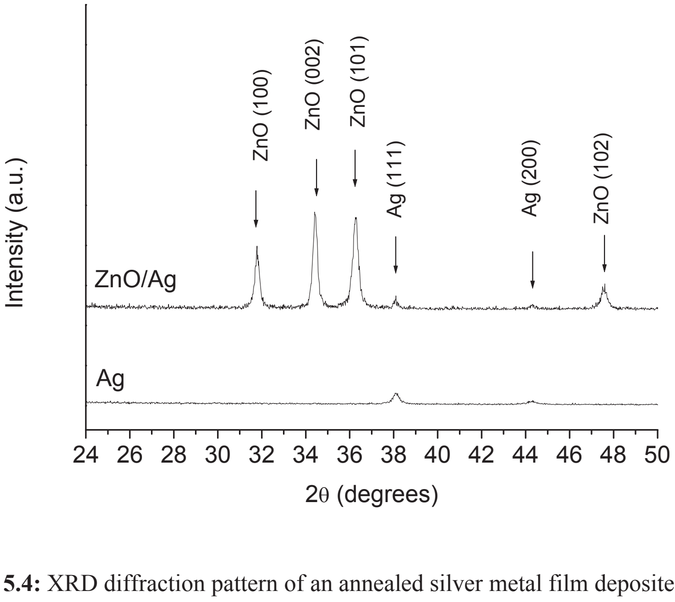

Figure 5.4: XRD diffraction pattern of an annealed silver metal film deposited on Si

Furthermore, Fig. 5.4 displays typical XRD patterns of the ZnO nanostructures that were grown on the metallic silver films on Si substrates. All of the diffraction peaks in the patterns can be exactly indexed as the hexagonal wurtzite ZnO. Moreover, both (111) and (200) silver phase were detected after ZnO deposition suggesting that no Ag_2O formation is detected after the ZnO deposition by MOCVD at reduced pressure in an Ar–O_2 atmosphere and temperatures up to 600 °C, which was also confirmed by previous studies [30].

Different process conditions have been used to control the catalytic effect and tailor the ZnO morphology. A massive ZnO nanowire production (Figure 5.5 (a,b)) is promoted by high deposition temperature (600 °C), despite the process deposition times (30 or 60 min).

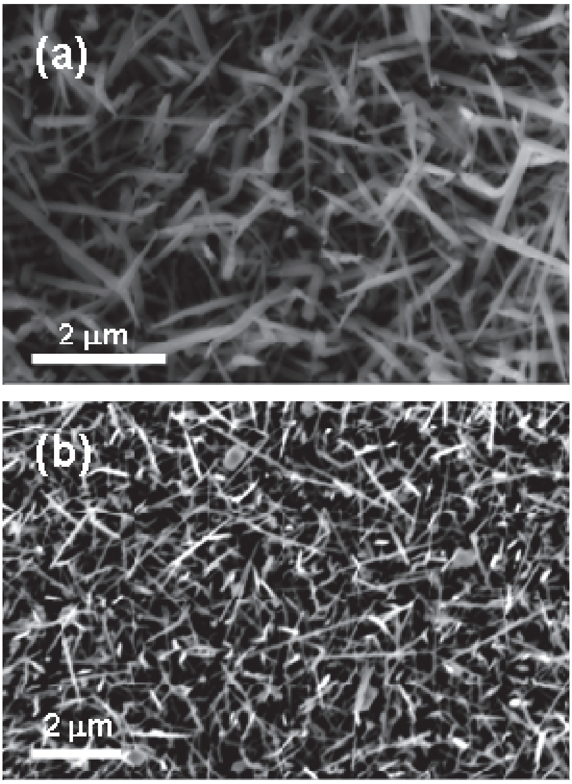

Figure 5.5: ZnO nanowires growth (on silver catalyst) at 600 °C after 60 minutes deposition (a) and 30 minutes deposition (b).

Following the decrease of the deposition temperature to 400 °C (30 min) the ZnO morphology changes significantly, thus, replicating the original catalyst nanostructure. Therefore, the overall ZnO nanostructure morphology appears affected by both catalyst initial concentration and ZnO deposition time (Fig. 5.6 (a-c)). In fact, after 30 min of ZnO deposition on silver catalyst, whose solution concentration was 0.01 M, the pristine Ag grain distribution is still visible and no significant ZnO growth is observed between the grains. A more extensive nanowire production is observed when deposition time is in-creased up to 60 minutes (Fig. 5.6 (b)) and/or when a higher concentration (0.1 M) is used (Fig. 5.6 (c)).

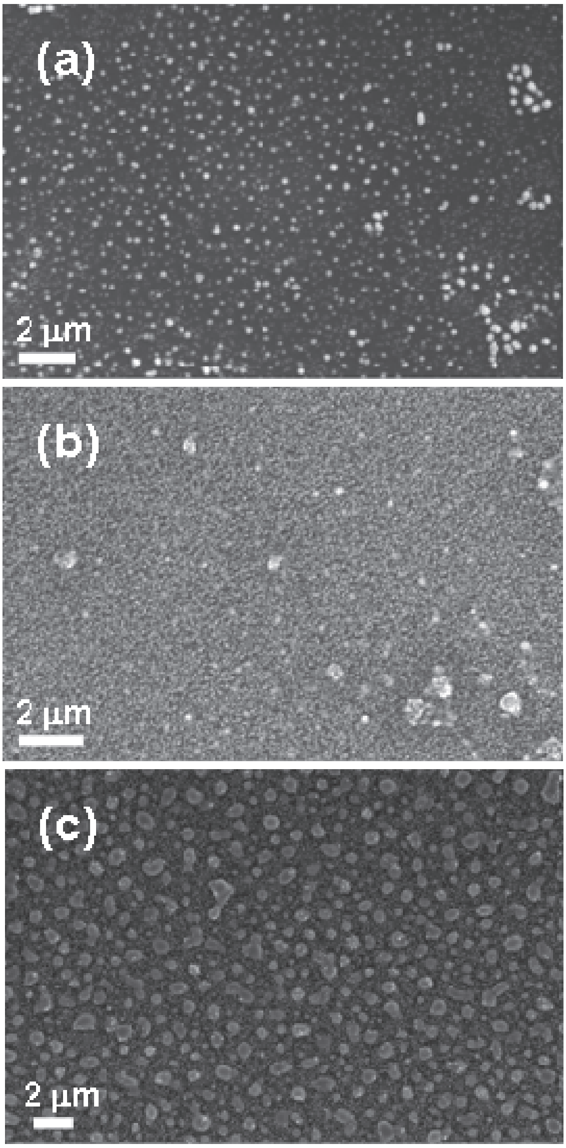

Figure 5.6: SEM images of ZnO films deposited on Ag catalyst layer (0.01 M initial Ag catalyst concentration) at 400 °C (a) 30 min (b) and 60 min (c) ZnO film deposited on Ag catalyst layer (0.1 M initial Ag catalyst concentration) at 400 °C/30 min.

The obtained data indicate a strong catalytic effect of the silver metal-organic precursor on ZnO growth and suggest that a proper tuning of the deposition process parameters (i.e., low catalyst concentrations, deposition temperature below 400 °C, short process time) limits and controls the high yield production of ZnO nanowires. Moreover, the accurate matching of both catalyst precursor initial concentrations and ZnO deposition process conditions are required for an effective integration of the presented approach with colloidal lithography to obtain ordered ZnO nanohole arrays [30].

The present data are promising to fabricate nanoring patterned ZnO/SiO_2 structures, obtained by a colloidal lithography-catalyst assisted MOCVD approach [12], as suitable nanoplatforms for a selective protein immobilization. It has been reported how polystyrene monodisperse nanospheres, self-assembled in hexagonally packed monolayers on silica substrate, have been employed to spatially confine a metal catalyst (i.e. Pt) which is used to assist the MOCVD deposition of ZnO at temperature below 400 °C (30 min).

The process sequence adopted to produce an ordered two-dimensional (2D) ZnO nanohole array includes 2 steps:

- Silver metal-organic precursor deposition on 2D PS close-packed array self assembled on Si substrate.
- The obtained patterned catalyst precursor patterned polystyrene layer is then used as substrate during the following ZnO MOCVD deposition.

The evidence of the proposed sequential steps is proven by the SEM images (Fig. 5.7 (a-c)). The pattern of the PS nanospheres monolayer (Fig. 5.7 (a)) is transferred onto the Si substrate by covering with silver catalyst film (Fig. 5.7 (b)). In fact, topographical patterns of silver catalyst, as obtained by drop casting of silver solution (0.01M) on a self-assembled monolayer of polystyrene colloids, are still discernible. The subsequently MOCVD growth at 400 °C (30 min) resulted in the formation of cheerios – like array of ZnO (Fig. 5.7 (c)). However, short deposition time is required to prevent the ZnO growth on bare silicon, as well as small concentration of precursor in order to obtain good patterning and avoid masking of polystyrene spheres with silver grains.

The presented results demonstrate an easy route for tailoring the morphology of ZnO films deposited by MOCVD. Herein, the evolving role of Ag metallic film layer during ZnO nanowire growth is investigated. Indeed the formation of ZnO nanowire arrays can be finely tuned through the proper choice of catalyst

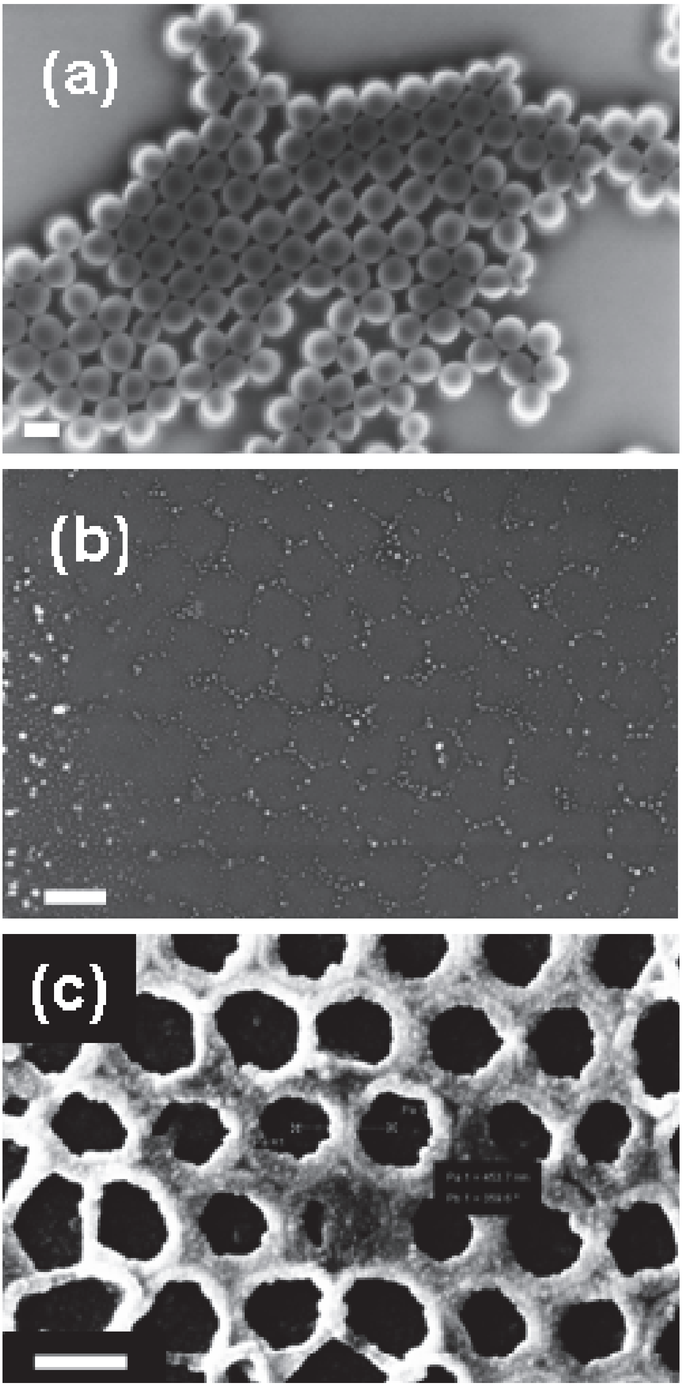

Figure 5.7: SEM images of PS colloidal nanospheres monolayers self assembled on Si (a); Ag catalyst patterned films after PS nanosphere removal (b); ZnO nanoholes ordered bidimensional array on patterned Ag catalyst. Size bar 200 nm

deposition technique and accurate control of the initial concentration of Ag catalyst precursor as well as of the ZnO growth process parameters, such as temperature and deposition time. Thus, it was shown that metal-organic silver precursor drastically enhances the ZnO nanowire growth rate. The possibility to simply play with both the concentration of metal-organic precursor solutions, easily deposited on any kind of substrate and the ZnO MOCVD process conditions, makes the proposed hybrid approach valuable to fabricate nanoporous ZnO based layers with remarkable high surface areas. Such nanostructures would be very promising for a wide variety of applications including bioengineering, catalysis, environmental engineering and sensor systems.

References

1. P. Yang, H. Yan, S. Mao, R. Russo, J. Johnson, R. Saykally, N. Morris, J. Pham, R. He, and H.-J. Choi, Adv. Funct. Mater 12 (2002) 323-331.
2. X. Wang, J. Song, Z. L. Wang, J. Mater. Chem. 17 (2007) 711–720.
3. Z.L. Wang, ACS Nano 2 (2008) 1987–1992.
4. X. Duan, Y. Huang, Y. Cui, J. Wang, C. M. Lieber, Nature 409 (2001) 66–69.
5. Y. Huang, X. Duan, Y. Cui, L. Lauhon, K. Kim C. M. Lieber, Science 294 (2001) 1313–1317.
6. J. H. Song, X. D. Wang, E. Riedo, Z. L. Wang, Nano Lett. 5 (2005) 1954–1958.
7. F. Patolsky, C. M. Lieber, Mater. Today 8 (2005) 20–28.
8. Z.M. Zhu, T. Chen, Y. Gu, J. Warren, R.M. Osgood, Chem. Mater. 17 (2005) 4227-4234.
9. Z. Zhang, S. J. Wang, T. Yu, T. Wu, J. Phys. Chem. C 111 (2007) 17500-17505.
10. M. Kirkham, X. Wang, Z. L. Wang, R. L Snyder, Nanotechnology 18 (2007) 365304-365308.
11. X. Wang, J.Song, C.J. Summers, J. H. Ryou, P. Li, R.D. Dupuis, Z. L. Wang, J. Phys. Chem. B 110 (2006) 7720-7724.
12. C. Li, G. Fang, Y. Ren, Q. Fu, X. Zhao, J. Nanosci. Nanotechnol. 6 (2006) 1467–1473.

13. J. Rybczynski, D. Banerjee, A. Kosiorek, M. Giersig, Z. F. Ren, Nano Lett. 4 (2004) 2037-2040.
14. M.H. Huang, Y. Wu, H. Feick, N. Tran, E. Weber, P. Yang, Adv. Mater. 13 (2001) 113-116.
15. X. Wang, C. J Summers, Z. L. Wang, Nano Lett. 4 (2004) 423-426.
16. Y. Zhang, J. Mu, J. Colloid Interface Sci. 309 (2007) 478-484.
17. S.K. Panda C. Jacob, Bull. Mater. Sci. 32 (2009) 493-498.
18. S.K. Panda and C. Jacob, Physica E 41 (2009) 792–796.
19. C. Li, G. Fang, Y. Ren, Q. Fu, X. Zhao, J. Nanosci. Nanotechnol. 6 (2006) 1467-1473.
20. A. Umar, S.H. Kim, Y.-S. Lee, K.S. Nahm, Y.B. Hahn, J. Cryst. Growth, 282 (2005) 131-136.
21. Y.C. Kong, D.P. Yu, B. Zhang, W. Fang, and S.Q. Fen Appl. Phys. Lett. 78 (2001) 407-409.
22. J.-J. Wu, C.-S. Liu, Adv. Mater. 14 (2002) 215-218.
23. J.L. Yang, S.J. An, W.I. Park, G.-C. Yi, W. Choi, Adv. Mater. 16 (2004) 1661-1664.
24. M.E. Fragalà , G.Malandrino, O. Puglisi, C. Benelli, Chem. Mater. 12 (2000) 290-293.
25. B. Gates, Q. Xu, M. Stewart, D. Ryan, C.G. Willson, G.M. Whitesides, Chem. Rev. 105 (2005) 1171-1196.
26. M.R.Jones, K.D. Osberg, R.J. Macfarlane, M.R.Langille, and C.A. Mirkin, Chem Rev. 111 (2011) 3736-3827.
27. H.J. Fan, P.Werner, and M. Zacharias, Small 6 (2006) 700-717.
28. S.-M. Yang, S. G. Jang, D.-G. Choi, S. Kim, H. K. Yu, Small 2 (2006) 458 – 475.
29. J.-H. Lee, I.-C. Leu, Y.-W. Chung, M.-H. Hon, Nanotechnology 17 (2006) 4445–4450.
30. M.E. Fragalà, C. Satriano, G. Malandrino, Chem. Commun. 7 (2009) 839–841.
31. J.H. Moon, W.S. Kim, J.-W. Ha, S.G. Jang, S.-M. Yang ,J.-K. Park, Chem. Commun. 32 (2005) 4107-4109.
32. L.S. McCarty, A. Winkleman, G.M. Whitesides, Angew. Chem., Int. Ed. 46 (2007) 206-209.
33. M.E. Fragalà, G. Compagnini, G. Malandrino, C. Spinella and O. Puglisi, Eur. Phys. J. D 9 (1999) 631-633.

34. Z. Zhang, S. J. Wang, T. Yu and T. Wu, J. Phys. Chem. C. 111 (2007) 17500-17505.
35. W. Lu and C.M. Lieber, J. Phys. D: Appl. Phys. 39 (2006) R387–R406.

6. Catalyst-free MOCVD fabrication of ultrathin ZnO films

Introduction

High quality ZnO films grown on Si substrates pave the way towards the integration with silicon technology-based devices [1-3]. Also, amorphous substrates, such as SiO_2 and glass substrate, have obvious technological advantages and potential applications [4]. Furthermore, decrease of deposition temperature remains a key technological challenge in integration with soft lithographic techniques, flexible device technologies and cost reduction for mass production.

Within the recent past few decades interest in ZnO-based sensors [5,6] has multiplied and there are still large areas of current technology in which the sensing potential of ZnO has not been explored at all. To a large extent, the selectivity, sensitivity and reproducibility of ZnO-based sensor will depend on surface chemistry, morphology and crystallinity of the material. Examples of the use of nanoscale ZnO materials in the enhanced fluorescence detection of protein interactions have shown that ZnO nanomaterials can serve as excellent signal-intensifying substrates for a wide range of protein systems and that the signal-enhancing capability is not influenced by the specific emission wavelength of fluorophores that are linked to protein molecules [7].

Interaction of biomolecules with nanomaterials is the area of fundamental interest due to their immense biological importance. Nanomaterials, which possess novel optical, electronic and chemical properties absent in bulk materials, have promising applications in biotechnology and life sciences [8,9]. Moreover, nanostructure materials exhibited interesting properties such as large surface to volume ratio, high surface reaction activity, high catalytic efficiency and strong adsorption ability that makes them potential candidate materials to play an important role in biomolecules immobilization [10]. The large surface area of nanomaterials provided better matrix for the immobilization of biomolecules leading to increased biomolecule loading per unit mass of particles.

In the previous chapter, we reported on the silver catalyst-assisted growth of ZnO nanostructures at low temperature (400 °C) [11]. However, the use of metal catalyst promoting the growth may result in the incorporation of metal into the ZnO structure as catalysts often remain on the tips and, therefore affect the purity, crystallinity and optical properties of the material [12,13]. Moreover, in terms of the integration with lithographic techniques the accurate choice of concentration of the catalyst and deposition strategies is crucial to achieve uniform spatial distribution of catalyst allowing the controlled patterned growth. In this respect, a catalyst-free low-temperature deposition of ZnO material has been investigated.

Recently, the ZnO nanoneedles and nanotips growth was reported on Si substrates by MOCVD applying diethylzinc as a precursor at a substrate temperatures in the range of 300 to 500 °C [12,14]. Later, Kim et al studied ZnO deposition via MOCVD on sapphire substrates using diethylzinc and they reported that below 200 °C no ZnO formation was observed [15],while other authors reported on the columnar structures formation on Si substrates in the growth range 100 - 250 °C [4]. However, the use of diethylzinc exhibits a disadvantage as it is highly pyrophoric and needs extreme care in terms of handling due to extreme sensitivity towards air and moisture [16]. Moreover, being highly reactive it causes the formation of powder in the cold zone of the reactor which degrades film quality [17]. In this aspect, bidentate ligands based metal-organic precursors offer an advantage which allows to avoid fluctuations during the experiment as they are water-free, thermally-stable, volatile, and in liquid state at processing temperatures. However, the reported MOCVD deposition conditions applying such precursors are in the 400 – 650 °C range [18].

Herein, catalyst-free low temperature MOCVD growth of ZnO on Si substrates is introduced. A study on the effects of the deposition temperature on the formation of ZnO films has been carried out. In particular, ZnO films have been deposited from a $Zn(tta)_2 \cdot tmeda$ precursor on Si (100) substrates at temperatures ranging from 250 to 400 °C up to 60 min. Moreover, the ZnO nanoring arrays fabrication on silica substrates by colloidal lithography assisted metal-organic chemical vapor deposition was scrutinized. Scanning electron microscopy, atomic force microscopy and X-ray photoelectron spectroscopy have been applied to characterize the structure, morphology and composition of as grown films to define time/temperature deposition threshold. The obtained results allow to set up the optimal experimental conditions for an effective colloidal lithography/catalyst-free MOCVD process integration, in order to fabricate bi-dimensional ordered ZnO nanohole arrays. Furthermore, the study of spontaneous immobilization of model analyte proteins to ZnO surfaces is presented. The discussed approach is based on the electrostatic interaction dependent on the isoelectric point concept, namely that at high isoelectric point ZnO favors the immobilization of low isoelectric point biomolecules in neutral pH media [19]. Herein, the interaction of ZnO with fluorescein-labeled albumin, used as model analyte biomolecule, was investigated by means of x-ray photoelectron spectroscopy, confocal microscopy and fluorescence recovery after photobleaching (FRAP) experiments. Fluorescein isothiocyanate–labeled albumin (FITC-albumin) has been chosen as model protein because it is the most abundant plasma protein and, hence, it is the first protein involved in the protein cascade process onto solid surface immersed in a biological medium and it will play a critical role in the following evolution of the adsorption process [20].

The results demonstrate that such ultrathin films have great potential as innovative fluorescence-sensing substrates, offering the possibility of sizing the two-dimensional (2D) vs. three-dimensional (3D) design of the ZnO – SiO_2 array (through the fine tuning of NSCL and MOCVD conditions), which, in turn, affects the individual addressability of the biomolecular detection.

Results and discussion

The ZnO films were prepared by Metal-Organic Chemical Vapor Deposition onto unpatterned silicon substrates. In order to understand how deposition temperature affects the growth and quality of the MOCVD-deposited ZnO films, the growth was carried at temperatures below 400 °C (Table 6.1).

Table 6.1: Deposition condition of catalyst-free MOCVD of ZnO films

Sample	T_d, °C	t, min
ZnO-1	250	40
ZnO-2	300	40
ZnO-3	400	5
ZnO-4	400	60

AFM and SEM were used for monitoring the morphological changes at the surface that result from ZnO deposition at different conditions. Fig. 6.1 shows the planar SEM images of ZnO thin films deposited on Si substrates at growth temperatures in the range of 250 – 400 °C. According to SEM images, the MOCVD deposition process is strongly affected by the deposition temperature of ZnO films. It should be noted that previously studied MOCVD deposition temperatures range from 400 °C to 700 °C and normally used deposition time is 1h [21].

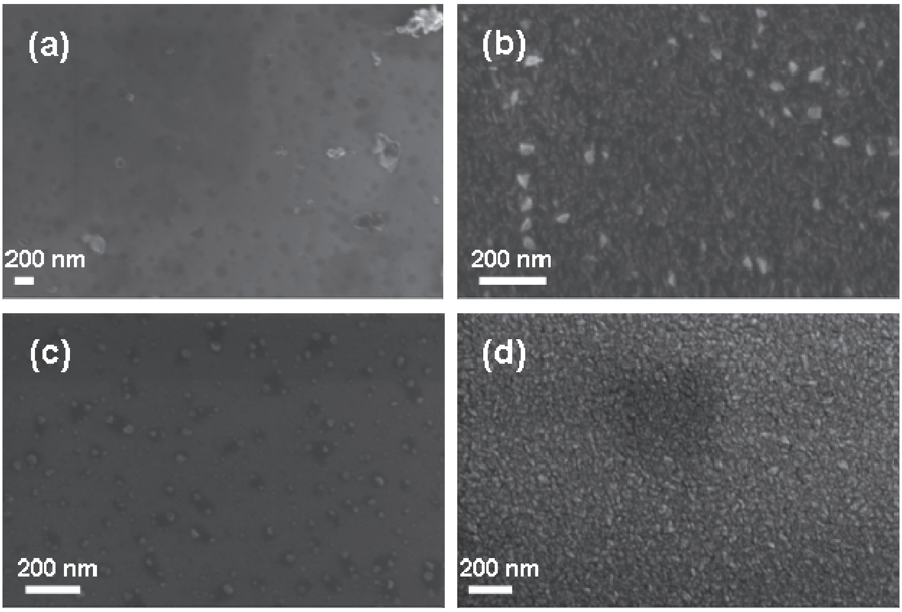

Figure 6.1: SEM images of ZnO film deposited on Si at (a) 250 °C/40 min; (b) 300 °C/40 min; (c) 400 °C/5 min and (d) 400 °C/60min

Therefore, the use of mild deposition conditions (low temperatures and short deposition time) resulted in ultra thin film formation having a granular structure. In particular, ZnO deposition at 250 °C/40 min (herein referred to as ZnO-1 sample) consists of sporadic and randomly distributed grains along the substrate surface (Fig. 6.1 (a)). As the deposition temperature is increased at 300 °C/40 min (herein named as ZnO-2), the sample morphology is characterized by a granular structure with a bimodal ZnO grain distribution, showing a predominance of small grains (about 15 nm of average dimension) and few large grains (about 50 nm of average diameter) randomly distributed over the surface (Fig. 6.1(b)). Upon further increasing the deposition temperature to 400 °C and reducing the deposition time to 5 minutes (herein referred to as ZnO-3 sample) a smoother morphology is well evident with about 50 nm large grains clearly visible on the substrate (Fig. 6.1 (c)). Finally, the sample deposited at 400 °C/60 min (herein named as ZnO-4), used as control thick film, shows a homogeneous granular morphology characterized by fairly well defined round grains having average dimensions of about 10 – 15 nm (Fig. 6.1 (d)). The morphological results provide confidence about two different ZnO deposition mechanisms, depending on the used deposition temperature. In particular an island-like ZnO layer formation (3D growth mode) can be hypothesised for the films deposited at the low temperature (< 300 °C). In this regime a limited ad-atom migration lengths at the substrate surface during the MOCVD process is likely to be responsible of the observed spot-like and non uniform deposition. On the other hand, upon increasing the deposition temperature (400 °C), the formation of a continuous layer is favoured, both kinetically and thermodynamically, due to coalescence of the isolated ZnO grains (growth mode transition from 3D to 2D), thus, resulting in smoother surface morphology of ZnO films.

These findings are in good agreement with AFM data. The topographies of the silicon substrate before and after ZnO deposition are shown in Fig 6.2. The results were observed at 5 different locations across every single sample, and a set of 3 samples was prepared at each processing condition. Figure 6.2 (a,b) shows the AFM scans of Si substrate surface topography and ZnO-1. The roughness of the ZnO-1 surface (0.47 nm) remains comparable to that of the substrate (0.44 nm) strongly supporting a negligible ZnO deposition. For ZnO-2 sample, an increase in surface roughness to 5.73 nm was observed (Fig. 6.2 (c)). Upon increasing the deposition temperature to 400°C, the ZnO-3 sample exhibits an overall smoother surface and the roughness being decreased to 1.93 nm, as shown in Fig. 6.2 (d). Finally, the thick control ZnO-4 sample represented in Figure 6.2 (e) shows the characteristic cobblestone appearance of the surface, with round grains that have fairly-well defined boundaries. For this ZnO control sample, the mean surface roughness is approximately 2.84 nm.

One likely explanation to the observed morphological evolution is that the ZnO layer deposited at 250 °C is characterized by a flat morphology with large isolated ZnO islands randomly distributed on silicon. At 300 °C ZnO grains almost completely cover the silicon substrate and a bimodal ZnO grain distribution characterized by small grains and large structures is evident. At 400 °C, if deposition time is limited to 5 min, ZnO growth is limited and more critical to be controlled. A smoother morphology is well evident from both SEM and AFM analyses, with well identifiable small grains distributed on silicon surface. Finally, the typical morphology of ZnO thick film is observed at 400 °C. This arises from the different ad-atom mobility attributed to the variation in deposition temperature which leads to different growth modes. Thus, at high temperatures, the atoms have enough diffusion activation energy to occupy the correct site in the crystal lattice so that grains with lower surface energy will become larger at high temperature. Then, the growth orientation develops in the one crystallographic direction of the low surface energy.

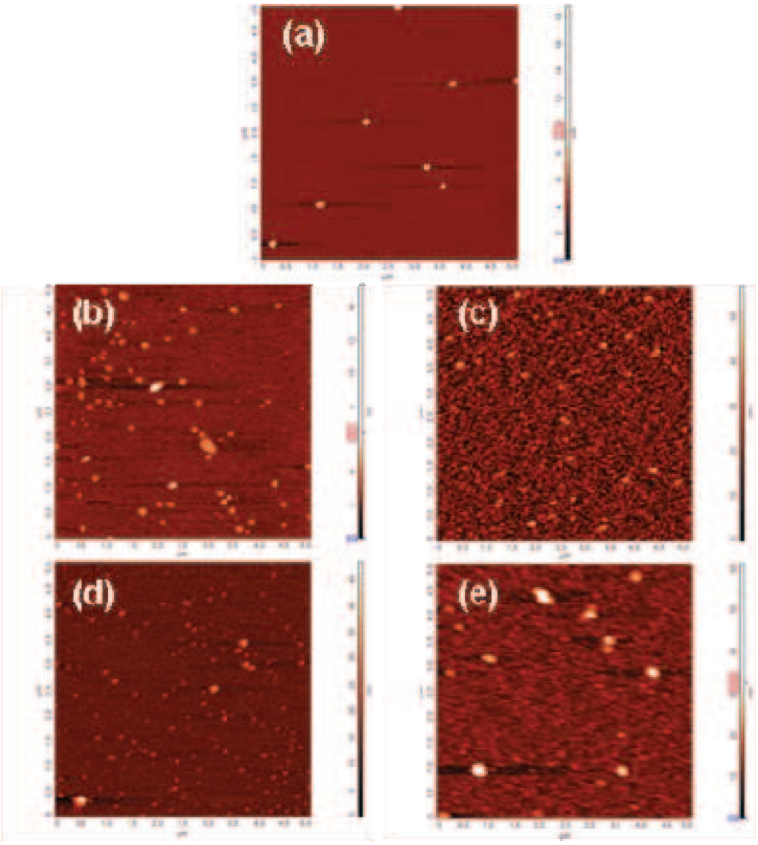

Figure 6.2: AFM images in tapping mode in air of homogeneous ZnO films (a) Si substrate (b) ZnO-1; (c) ZnO-2; (d): ZnO-3; (e) ZnO-4

In order to investigate the chemical structure of the MOCVD-deposited films XPS was employed. The XPS spectral results confirm a similar surface chemical composition for all the investigated ZnO samples. The expected signals related to Zn, C and O and other impurities have been detected. The average atomic compositions from XPS analysis are reported in Table 6.2.

Table 6.2: Surface average atomic compositions of samples before of ZnO films deposited at various temperature.

Sample	Zn, at%	O, at%	C, at%	Si, at%	Zn/Si	C/Zn
Si	N/A	14	33	53	N/A	N/A
ZnO-1	2	22	39	37	0.1	24.6
ZnO-2	14	51	35	0.1	140.0	2.5
ZnO-3	20	44	25	11	1.8	1.3
ZnO-4	29	45	26	0.1	290.0	0.9

The Zn content increases upon increasing the deposition temperature from 2 % (ZnO-1 sample) to 29 % (ZnO-4 sample). It is to note that the zinc signal detected for sample deposited at 250 °C remains within the significance of experimental error at the used conditions, i.e. 2% of atomic composition, strongly supporting the negligible ZnO deposition at this deposition temperature and in good agreement with AFM results. Therefore, ZnO deposition temperature threshold can be set above 250 °C. It must be noted an increase in oxygen composition from 22 to 51 % upon increasing the deposition temperature. Furthermore, it should be noted, that the silicon signal is clearly visible for ZnO-1, in good agreement with a limited surface coverage, whilst it becomes negligible for ZnO-2 and ZnO-4, thus indicating good substrate surface coverage. On the contrary, the detected silicon signal for ZnO-3 is 11% which is about 80% of silicon attenuation detected for bare silicon substrate. These findings confirm the observations from AFM and SEM data, i.e. the formation of randomly distributed ZnO small grains with a reduced average surface coverage.

As a consequence of the mild ZnO-2 deposition conditions, a relatively low zinc content and a corresponding high C/Zn ratio point to significant carbonaceous residuals at the surface, which are mostly attributed to unreacted precursor as well as unavoidable surface hydrocarbon contamination. In fact, the intensity of the lower energy peak, positioned at 285.0±0.2 eV in the C 1s which can be attributed to C-H bonding, is higher for ZnO-2 than ZnO-3 and ZnO-4 [22].

Moreover, in the case of ZnO-3 sample, notwithstanding the significant silicon signal detected, both the C/Zn atomic ratio and the zinc atomic content point to a surface chemical composition comparable to that of ZnO-4 sample (i.e. temperature-driven efficiency to control the precursor decomposition), but with a lower film thickness and uniformity (i.e. insufficient deposition time to attain the complete coverage).

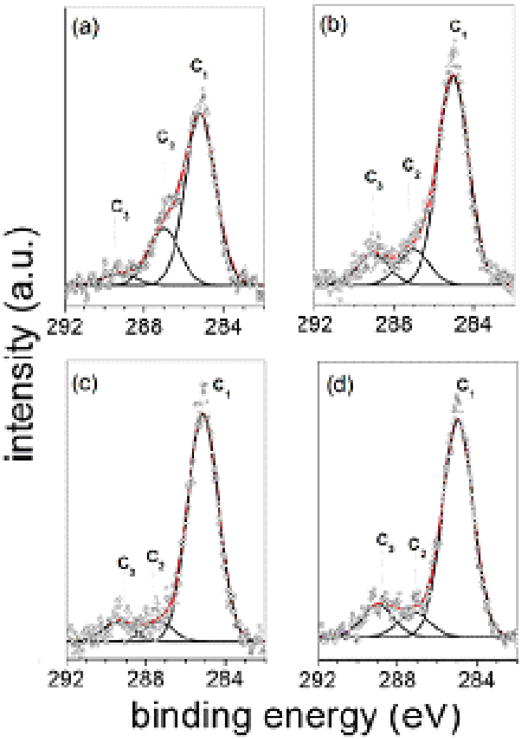

Figure 6.3: XPS high resolution spectra in the C 1s binding energy region for (a) Si, (b) ZnO-2, (c) ZnO-3 and (d) ZnO-4

Figure 6.3 shows the high energy resolution carbon C 1s photoelectronic spectra of the Si substrate and three deposited films, namely ZnO-2, ZnO-3 and ZnO-4. Three components (C_1, C_2, C_3) result from the C 1s peak de-convolution. The main component, C_1, centered at 285.0±0.2 eV is related to C-C and C-H groups, the second one C_2 at 286.5±0.2 eV is related to C-O bonds at surfaces and third component C_3 at 288.8±0.2 eV has been assigned to carbon doubly bonded to oxygen such as C(=O)O or O-C-O bonds [23].

Noticeably, ZnO-2 surfaces exhibit a higher content of polar linkages than the ZnO-3 and ZnO-4 ones, as evidenced by the relative ratio of carbon–heteroatom bonds (i.e. C_2 + C_3 components) with respect to the hydrocarbon species (C_1 component) represented in Figure 6.4.

To conclude, XPS analysis evidences that ultrathin ZnO films were deposited at all deposition parameters chosen. However, the information on the chemical composition suggested that the deposition temperature above 300 °C is required to grow films with fairly good surface coverage and reduced presence of carbon-related species.

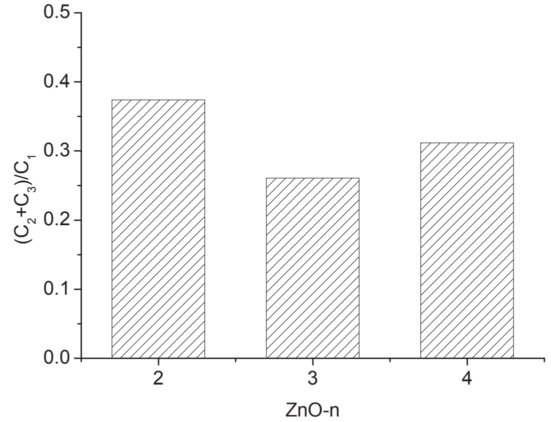

Figure 6.4: Relative ratio of carbon–heteroatom bonds (i.e., $C_2 + C_3$ components) with respect to the hydrocarbon species (C_1 component) calculated for ZnO-n (n=2,..,4)

By applying the above discussed deposition conditions to deposit ZnO on silicon substrates patterned by colloidal lithography, the formations of ZnO nanohole arrays were successfully achieved. ZnO-n-NP (n=2,3,4) corresponds to the conditions used in order to fabricate ZnO-n (n=2,3,4) substrates as shown in Table 6.1 on polystyrene (PS) nanopatterned silicon substrates respectively.

Table 6.3: XPS average atomic concentrations and characteristic atomic ratios for PS nanospheres treated samples

Substrate	Zn, at.%	O, at.%	C, at.%	Si, at.%	C/O
ZnO-2-NP	5	33	54.	8	1.7
ZnO-3-NP	13	43	31	13	0.7
ZnO-4-NP	30	41	29	0.1	0.7

The average surface atomic composition of the colloidal lithography assisted ZnO nanostructured films was evaluated in order to reveal the effect of the temperature on the growth mode (Table 6.3). From these data, the Zn content detected for the PS-ZnO-2 sample (~ 5%) is lower than that of ZnO-3-NP and ZnO-4-NP (~ 13% and ~ 30%, respectively). Moreover, Zn content for samples

ZnO-2-NP and ZnO-3-NP is reduced by 64% and 36% with respect to unpatterned grown films. On the contrary, for ZnO-4-NP sample the average surface composition after nanopatterning is almost similar to that of the unpatterned sample, thus suggesting a less controllable integration strategy.

The morphological conformations of obtained ZnO nanostructured layers were estimated by SEM and AFM. Figure 6.5 demonstrates the formation of ZnO nanohole arrays resulted from two-step colloidal lithography – MOCVD approach using different deposition conditions. The polystyrene nanospheres of 1 μm in diameter were used to prepare the template.

Tailoring of ZnO deposition at this low deposition temperature range (300-400°C), close both to precursor decomposition temperature and PS nanospheres template decomposition temperature, is extremely critical and therefore, slow growth rate and low efficiency deposition can be assumed.

It must be noted, that polystyrene underlayer is partially remained on the substrate surface, therefore further sonication in non-polar solvent (toluene was used in this case) is needed for the polystyrene removal. When the deposition temperature is set to 300 °C clear film morphology representing ZnO honeycomb-like layer can be identified by SEM (Figure 6.5 (a,b)). The obtained honeycombs are characterized by even round boundaries having ring diameter of about 1 μm. By further increasing the temperature to 400 °C and reducing the deposition time to 5 minute residues of polystyrene spheres are still visible as the time is not enough to fully decompose the organic matter (Fig. 6.5 (c)). Moreover, the diameter of the fabricated ring is shrunk to 800 nm. The height of the rings was estimated from the AFM images. The height of the ring increases from about 80 nm to 90 nm for ZnO-2-NP and ZnO-3-NP samples respectively. The diameter of the rings also changes with the increase of the deposition temperature.

In order to investigate the interface between such ZnO based thin films and biomolecules, albumin has been used as model analyte. In fact, in accordance with the different isoelectric point (IEP) values, at the physiological pH of 7.4 albumin (negative surface charge) is expected to irreversibly bind on ZnO surfaces (positive surface charge) by spontaneous adsorption driven by electrostatic interactions [19].

XPS and confocal microscopy with the application of the FRAP technique were used to study (i) the change in emission properties of ZnO; (ii) the biomo-

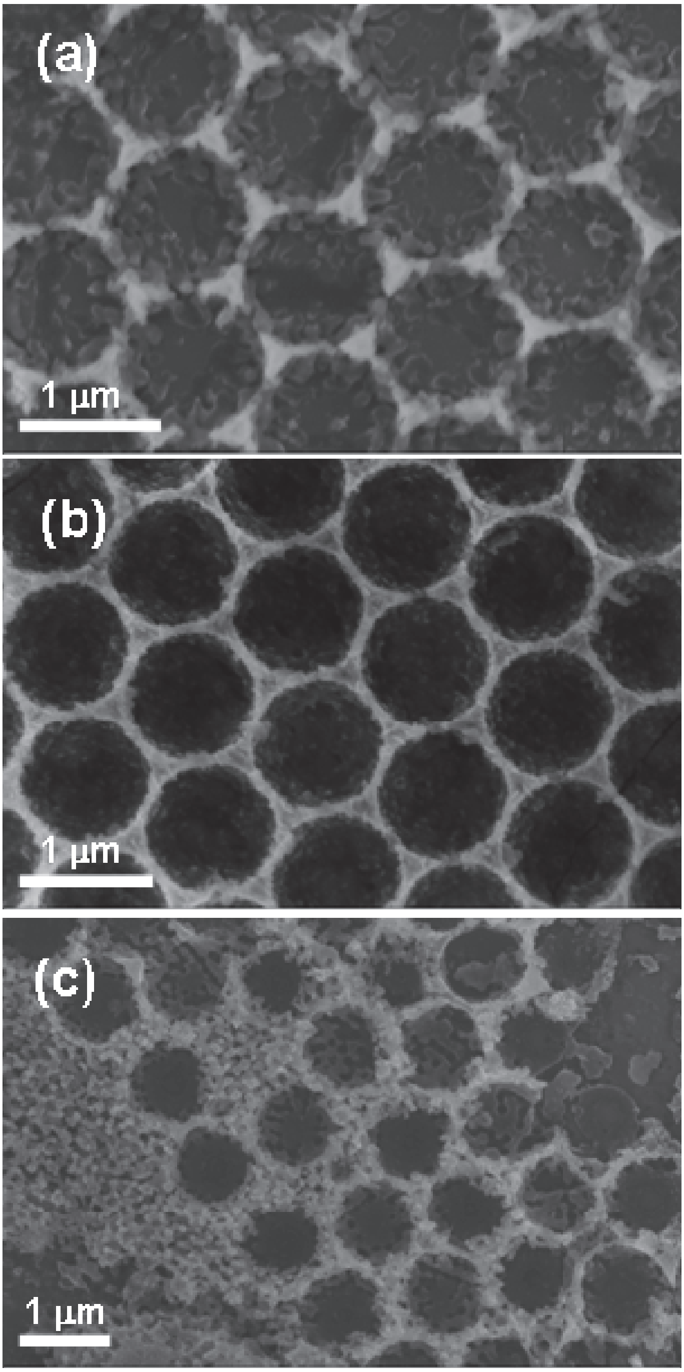

Figure 6.5: SEM images of ZnO film deposited on Si substrates patterned with PS nanosphere: (a) 300 °C/20 min,(b) 300 °C/40 min, and (c) 400 °C/5 min

lecule lateral mobility in the adlayer and (iii) the protein surface coverage and its average orientation.

The adsorption of FITC-albumin was carried from aqueous solutions at pH=7.4 on ZnO ultrathin films (patterned and unpatterned) deposited by catalyst –free MOCVD approach in mild time-temperature regime as stated in Table 6.1. XPS was applied to characterize the chemically modified ZnO unpatterned surfaces after the protein immobilization. The appearance of a strong peak at 400.0 eV corresponding to the N (1s) electrons clearly indicates the presence of a protein layer on ZnO surface after incubation with FITC-albumin solution (Table 6.4).

Table 6.4: XPS quantitative analysis in terms of average atomic composition (at.%) for the different ZnO films after albumin absorption

Sample	Zn, at%	O, at%	C, at%	Si, at%	N, at%
S i+ FITC-albumin	-	37	41	14	6
ZnO-2 + FITC-albumin	2	29	58	6	5
ZnO-3 + FITC-albumin	7	40	37	10	6
ZnO-4 + FITC-albumin	8	48	38	-	6
FITC-albumin	-	58	28	-	14

After the spontaneous protein adsorption followed by rinsing out of the weakly bound molecules, a certain amount of irreversibly immobilized protein is detected at the surfaces of all the ultrathin ZnO-based films as well as the two reference controls, namely bare silicon (i.e., about 10 nm-thick native silicon oxide on silicon) and ZnO-4 (about 50 nm-thick ZnO).

The comparison between the protein-characteristic nitrogen signals detected at the surfaces of all the above-mentioned samples ranging from 5 to 6% and the value of about 14% found for an ideally thick FITC-albumin adlayer (at least for the sampled depth of about 1.4 nm at the used experimental conditions) indicates a protein coverage roughly corresponding to the half of a monolayer [19].

Figure 6.6 shows the characteristic atomic ratio N/(Zn+Si) giving some insight to protein adsorption on the surface. It is clearly seen that less protein

(N/(Zn+Si)=0.5) is adsorbed on silicon substrate and ZnO-2 sample. Conversely, ZnO-2 and ZnO-4 show a high affinity towards the protein.

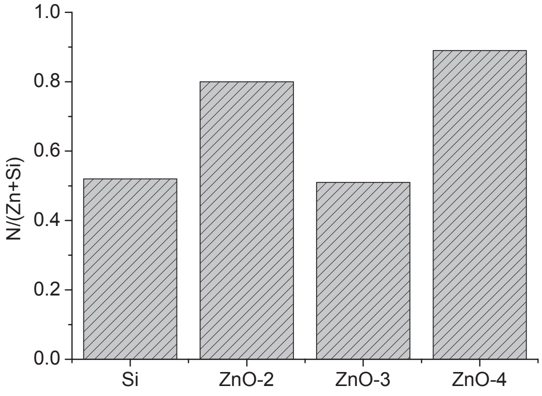

Figure 6.6: Characteristic atomic ratio N/(Zn+Si) calculated for silicon substrates and as deposited ZnO films after protein adsorption

These results can be related to variation of surface roughness. In fact, it is reported that ZnO rough surfaces are more hydrophobic than smoother surfaces and, therefore, result in higher albumin adsorption [24]. Accordingly, ZnO films having higher surface roughness (ZnO-2 and ZnO-4) have shown better affinity towards the protein therefore promoting the adsorption. However, it should be mentioned that the analytical quantification of protein coverage on the investigated surfaces is surely affected by the expected partial surface dissolution of ZnO. In fact, the biodegradation of ZnO in aqueous media and biofluids is a well-known process with important implications for biomedical applications [25]. ZnO is poorly soluble in water, but it can slowly dissolve in both acidic and strong basic conditions [26]. However, presence of biological components such as proteins and amino acids can also enhance the oxide dissolution through the complexation of the Zn^{2+} free ions released from the material surface [26-28].

By comparing Table 6.4 with Table 6.2 an increase of the Si contribution of ZnO-2 sample after protein uptake (from 0.1% to 6%) is clearly detected. Fig. 6.6 shows, for that sample, the large concentration of unsaturated bonds, -OH groups and polar moieties that can readily interact with the protein molecules, thus promoting a prompt biodegradability.

The detailed analysis of the spectra of carbon and oxygen 1s energy level respectively might be able to describe the behaviour behind the interaction between the albumin molecule and ZnO surface.

After the protein immobilization, a broadening of C 1s peak is observed for all the investigated samples (6.7 (a-d) respectively) with respect to the pristine surfaces (Fig. 6.7 (a'-d'); a new component (C_4) at BE of 288.3± 0.2 eV indicates the presence of peptide bond (-C(=O)-NH)-) [20].

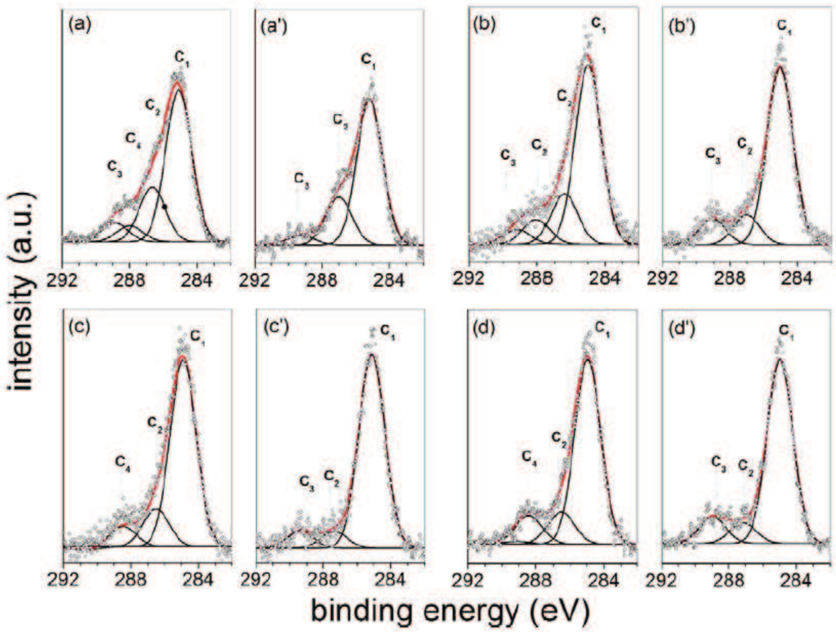

Figure 6.7: XPS high resolution spectra in the C (1s) binding energy region for (a) Si, (b) ZnO-2, (c) ZnO-3 and (d) ZnO-4 after the protein adsorption and, as comparison, for (a') Si, (b') ZnO-2, (c') ZnO-3 and (d') ZnO-4 before the protein adsorption

Moreover, the spectral comparison shows that the C_2/C_4 ratio is about 2 for ZnO-2, ZnO-3 and reference Si surfaces, while it is reduced to 1 for control ZnO-4 sample. This fact indicates that, notwithstanding the comparable protein mass uptake, the average orientation of C-O, C-N, C-S bonds (C_2) with respect to C=O species (C_4) of the protein adlayers is different at the interface with the thin ZnO–SiO_2 and Si substrates with respect to the thick ZnO-4 control film. This evidence suggests that SiO_2 uncovered areas in both ZnO-2 and ZnO-3 thin films contribute significantly to the actual surface termination, thus consisting in hybrid ZnO–SiO_2 biointerface. The evidence of hybrid ZnO–SiO_2 active surfaces for the newly deposited ZnO ultrathin layer is further supported by the O

1s high-resolution spectra as shown in Fig 6.8.

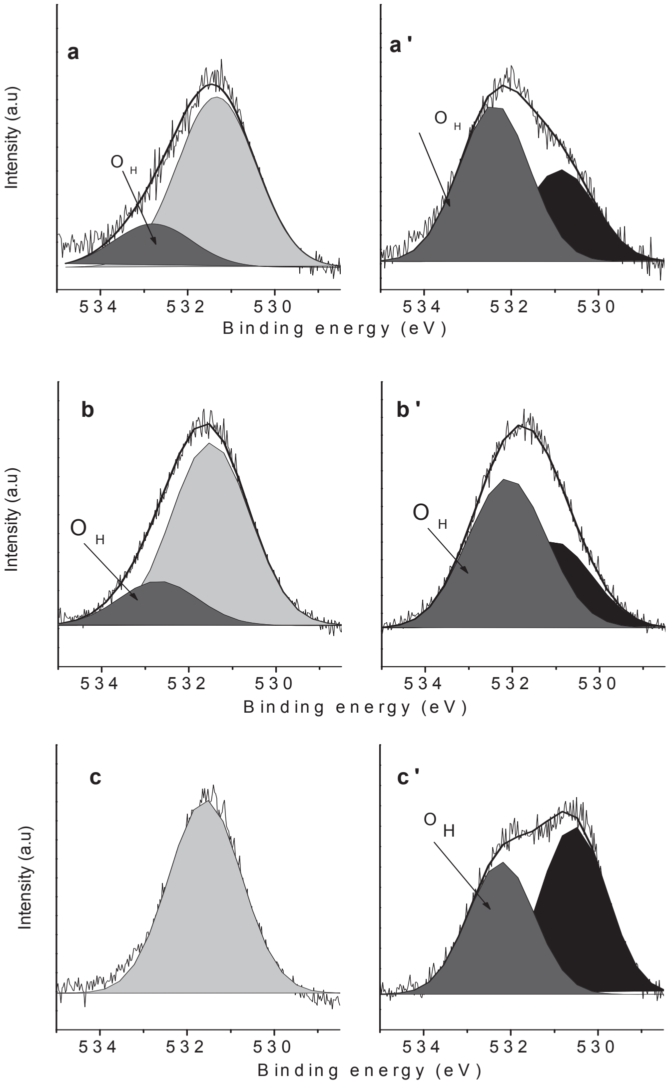

Figure 6.8: XPS high resolution spectra in the O (1s) binding energy region for (a) ZnO-2, (b) ZnO-3, and (c) ZnO-4 after protein adsorption and, for comparison, for (a’) ZnO-2, (b’) ZnO-3, and (c’) ZnO-4 before protein adsorption

For the as-deposited ZnO films, the O 1s photoelectron peak can be consistently decomposed into two components (Fig. 6.8 (a’-c’)), respectively, at 530.5 ± 0.2 eV (OM) and 532.0 ± 0.2 eV (OH). The lower binding-energy component is attributed to O^{2-} ions of the crystalline network, which is identified as originating from O 1s core level of Zn-O [29], while the higher binding-energy component is usually attributed to O^- species, i.e., the presence of loosely bound oxygen on the surface of ZnO film [30]. The surface-related component is prevailing in the ultrathin films ZnO-2 and ZnO-3 (OH/O_{tot}, respectively, of 66% and 63%), while it is slightly lower than the OM component in ZnO-4 film (OH/O_{tot} ~ 45%). After the protein immobilization process (Fig. 6.8 (a-c)), the OM component is hindered by the predominance of a new component centered at BE = 531.5 ± 0.2 eV, which is related to the protein C=O bonds. This protein-related component is comparably higher than the OH one for both the ultrathin ZnO – SiO_2 films (about 3:1), while it is the only one visible for the control ZnO-4.

To summarize, evidence of comparable protein mass uptakes onto the different ZnO-based films is provided by the attenuation of the substrate-related signals (Zn, Si and OM component of the oxygen peak) as well as the appearance of protein-related signals (nitrogen and (C_4) component of the carbon peak). The average protein orientation at the interface with the ultrathin ZnO-based films seems to be affected by the hybrid ZnO–SiO_2 character of the surfaces with respect to the control ZnO-4 sample.

Fluorescence microscopy was employed to scrutinize the response of the various ZnO deposited films to the binding of fluorescein-conjugated albumin as well as to implement data from XPS analysis about protein surface coverage, density and uniformity. Indeed, fluorescence analysis allowed determining in a semiquantitative way the protein uptake for the different ZnO films as well as the lateral mobility of the protein at the protein–zinc oxide interface.

Fig. 6.9 shows the representative LSM images recorded in fluorescence mode at the borderline between protein-exposed (brighter area) and masked (darker area) regions for control SiO_2 (Fig. 6.9 (a)), ultrathin ZnO – SiO_2 film (ZnO-3, Fig. 6.9 (b)) and thick ZnO control (ZnO-4, Fig. 6.9 (c)) samples. As our experimental scheme involves non specific adsorption of the protein molecules onto substrates, the protein molecules were randomly distributed over the entire protein-exposed surface area. Indeed, an enhanced fluorescence, related to the enhancement of emission recorded at 519 nm of wavelength, is observed for all the ZnO films as well as the control glass (SiO_2) upon the uptake of fluorescein-labeled protein. By assuming that the uniformity of the antigen coverage can be correlated with the standard deviation in pixel luminance for each of the samples, it appears that the protein coverage is less homogeneous on the ultrathin ZnO–SiO_2 films than on the thick ZnO sample.

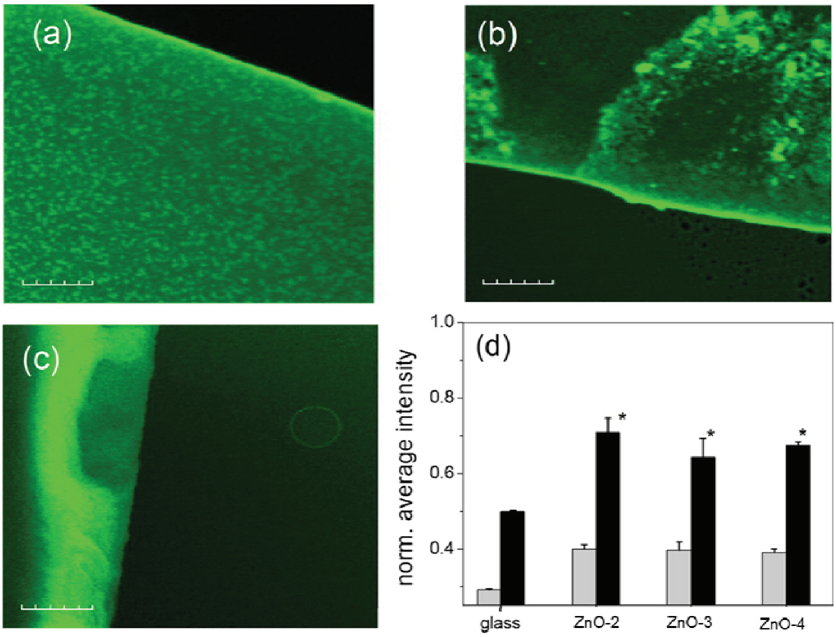

Figure 6.9: LSM results for protein ZnO-SiO2 biointerfaces: (a-c) Characteristic fluorescence at the borderline between masked and albumin exposed regions for: (a) glass, (b) ZnO-3 and (c) ZnO-4, (d) average emission intensity at 519 nm for each surface after protein immobilization (black columns) vs. incubation with buffer (gray columns) significant difference with respect to glass, as calculated with ANOVA, $p < 0.001$ (average of 15 photobleached spots per substrate in each experiment, error bars = standard deviation).

What is more, the comparison of the fluorescence intensity for the differently protein-exposed films normalized vs. the corresponding control bare substrate and subtracted of the background emission (Fig. 6.9 (d)) evidences roughly a twofold increase in average fluorescent intensity ($p < 0.001$) of the ZnO-based samples compared with SiO_2, notwithstanding the comparable amount of immobilized protein as estimated by XPS. This fact points to the capability of our deposited ultrathin ZnO films to work as nanoplatform for fluorescence enhancement upon interaction with the protein.

The laterally homogeneous and ultrathin ZnO-based films have been compared with ZnO – SiO_2 nanoplatforms in order to scrutinize the lateral diffusion properties of protein adlayers on the patterned micropore arrays vs. the unpatterned ZnO films.

As matter of fact, the reduced critical dimensionality of ZnO materials at the nanoscale, either by topographic or by chemical structuring, such as ZnO nanorods or SAM-modified planar ZnO, is known to play a fundamental role in the fluorescence enhancement effect [7]. Therefore, the dimensional control of ZnO nanomaterials is very critical to trigger fluorescence detection from proteins. In this context, it has been reported that ZnO nanoplatforms, consisting of thin films of hexagonally patterned ZnO nanoring arrays and SiO_2 circular areas, as obtained by colloidal template-assisted MOCVD process, are effective for immobilization of albumin [19]. As the effective process integration of colloidal lithography with MOCVD performed at extremely mild conditions has been demonstrated at the temperature/times of deposition as those used in the case of ZnO-3 samples [11,31], the ultrathin ZnO-3 films have been patterned into dense and regular micropore arrays (ZnO-3 NP samples).

The mobility properties of the protein molecules adsorbed on the two types of ZnO substrates have been assessed by FRAP experiments, which consist in using a focused laser beam at high power to intentionally photobleach quickly and locally fluorescently tagged proteins. Mobile proteins can exchange with their unbleached counterparts, leading to the recovery of fluorescence in the photobleached area at rates proportional to protein mobility.

FRAP is commonly employed to measure long-time two-dimensional diffusion of proteins adsorbed at solid–liquid interfaces, which depends on both protein–surface and protein–protein interactions [32,33].

Fig. 6.10 shows the results of the FRAP experiment performed on the protein adlayer onto both unpatterned (Fig. 6.10 (a)) and patterned (Fig. 6.10 (b)) ZnO-3 samples. It is worth of note that both types of protein – ZnO bio-interfaces exhibit an extremely dynamic character, as well addressed by the micrographs taken at $t \sim 0$. In fact, the initial fluorescence before bleaching ($t < 0$) is expected to be quenched in a well-defined circular area by the high-intensity laser beam (circles drawn in Fig. 6.10 (a,b), $t < 0$).

However, due to very fast random motion/diffusion of bleached protein molecules exchanging their position in the bleached area with non-bleached molecules from the surrounding, the bleached circles are not well defined already within the time required to record the first micrograph ($t \sim 0$). This finding suggests that the albumin aggregates on the ZnO substrates have a relatively fast diffusion at the surfaces and move around independently.

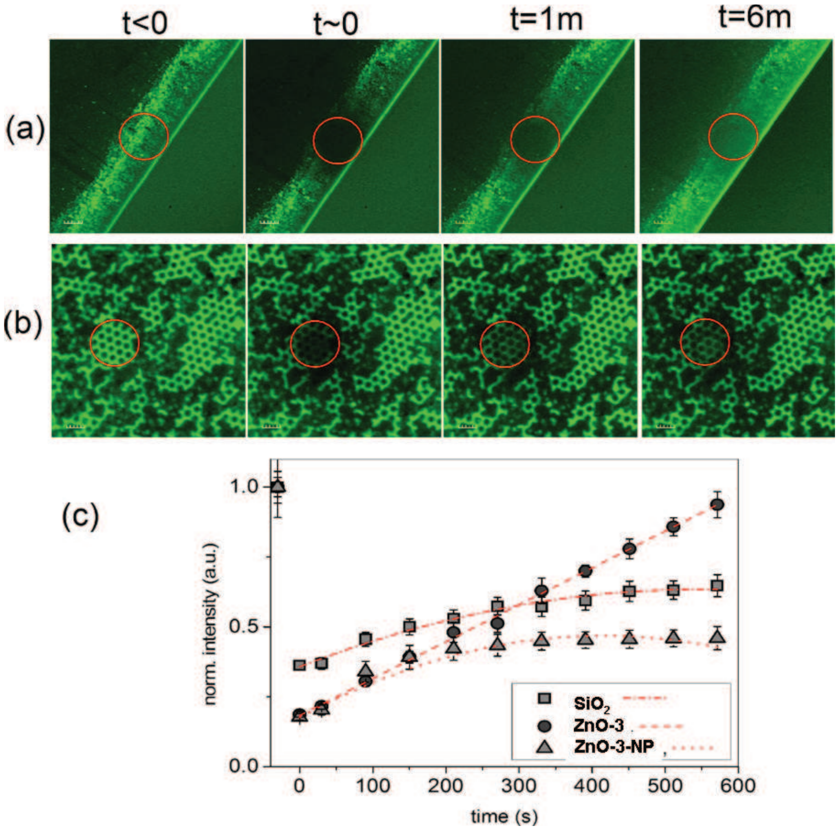

Figure 6.10: Fluorescence recovery after photobleaching for albumin in adsorbed on: (a) unpatterned ZnO-3 and (b) patterned ZnO-3 NP. Images are shown (from left to right) for pre-bleach, beach, after 1m After 1 m and 6 m of time lapse, (c) Time-solved fluorescence from samples shown in (a and b), as well as control albumin adsorbed on SiO_2 (glass). Average of 12 photobleached spots per substrate in each experiment were investigated.

As to the fluorescence recovery (t > 0), two different kinetics are observed for the unpatterned and micropore-patterned ZnO-based films, corresponding to linear and polynomial fits, respectively (Fig. 6.10 (c)). In particular, the protein molecules adsorbed on the ZnO-3 NP exhibit only a partial recovery and a lower effective diffusion than those adsorbed on the ZnO-3 surfaces. It is noteworthy that the fluorescence recovery from the protein adlayer on the reference glass substrate exhibits a polynomial curve trend similar to that observed for the hybrid ZnO–SiO_2 micropore sample.

The diffusion coefficients calculated by using the Axelrod's algorithm [34] are, respectively, of $2.4 \cdot 10^{-10}$ cm^2/s on glass, $1.5 \cdot 10^{-10}$ cm^2/s on ZnO-3 and

$1.0 \cdot 10^{-11}$ cm^2/s on ZnO-3 NP. These findings indicate that, apart from the obvious enhanced friction suffered by the molecules moving inside the pore rims of the patterned ZnO-3 film in comparison with the unpatterned sample (i.e., topographic effect), the presence of SiO_2 areas confined by the ZnO is relevant to trigger the protein mobility at the biointerface (i.e., chemical effect).

Similar results, pointing to a friction-reduced lateral diffusion on pore rims compared with that of the area within the pore, have been reported for lipid membranes on ordered porous silicon substrates [35]. In our case, the protein diffusion rate on the hybrid ZnO–SiO_2 surface is likely be affected not only by the topography but also by the surface chemistry and charge. In fact, the latter are crucial factors for the strength of interaction and the protein conformation at the protein–solid interface, thus affecting the transport process elucidated by FRAP [33,36,37].

It must be also mentioned that, since the ZnO isoelectric point is higher than that of SiO_2 (i.e., IEP 9.5 vs. 2 [38]), it is consistent that the fraction of immobile and laterally diffusing molecules at the solid–liquid interface is locally different on the hybrid ZnO– SiO_2 system.

To conclude, in this chapter the procedure to fabricate ultrathin unpatterned and patterned ZnO films on silicon substrates was described. Particular attention was devoted to the growth of ZnO in mild deposition time ($\leq$ 60 min) - temperature (250 - 400 °C) regime.

The conducted depositions on unpatterned silicon substrates resulted in the formation of ZnO films having grain-like structure. In particular, the study of morphology of as grown films revealed that longer deposition time and higher temperatures are required to grow smoother films. Moreover, the analysis of the composition suggested that higher deposition temperatures result in better substrate coverage along with less carbon contamination of the films obtained. Therefore the lower deposition temperature threshold was set to 300 °C.

In case of ZnO films grown on patterned substrates, the structured ZnO nanohole arrays were obtained, consisting of ZnO confined rings on SiO_2 surface. Composition analysis revealed that growth at 400 °C for 60 min resulted in formation of continuous layer fully covering silicon substrate. Tailoring of time-temperature parameters allowed to control thickness of nanohole arrays and the inner diameter of the rings. The described two-step approach represent a bottom-up approach allowing to obtain ZnO/SiO_2 ultrathin films which are promising for use as nanoplatforms for biological sensing.

The combined use of PS nanospheres template and catalyst-free MOCVD or CBD can benefit in growing ZnO nanoring arrays (at low temperature and short time), characterised by very large surface areas, which replicate the template of the PS monolayer assembly. The designed fabrication procedure leads to formation of porous materials having a wide variety of applications in bioengineering, catalysis, environmental engineering, and sensor systems because of their high surface-to-volume ratio.

This study is offered as an initial investigation for the preparation of ZnO-based sensors, by elucidating on an integrated MOCVD–CL deposition strategy to produce hybrid ZnO–SiO_2 platforms having tunable chemistry and topography, which in turn enables different fluorescence detections during biomolecule binding events. The electrostatic interaction based technique provides an easy and fast-responding optical platform for a “signal-on” detection of proteins, which might be applicable for the real time assay of proteins.

Further studies with a wide range of new patterns, for instance by changing the density and/or the area of the ZnO–SiO_2 pore arrays, will allow the tuning of the surface reactivity towards transport processes at the biointerface to be used as models in biological studies or in applications such as biosensors.

References

1. N. H. Nickel. Zinc oxide – a material for micro- and optoelectronic applications, Springer, 2005, 240 p.
2. K. Ellmer, A. Klein, B.Rech (Eds.), Transparent conductive zinc oxide: basics and applications in thin film solar cells. Series:Springer Series in Materials Science, Vol. 104 2008, XIV, 446 p.
3. X. Wang, C.J. Summers, and Z.L. Wang, Nano Lett. 4 (2004) 423-426.
4. H.W. Kim, N.H. Kim, and C. Lee, J. Mater. Sci. Lett. 22 (2003) 1117–1118.
5. J. Xu Q. Pan, Y. Shun, Z. Tian, Sens. Actuators, B 66 (2000) 277-279.
6. F. Zhang, X. Wang, S. Ai, Z. Sun, Q. Wan, Z. Zhu, Y. Xian, L.Jin, K. Yamamoto, Analitica Chimica Acta 519 (2004) 155-160
7. A. Dorfman, N. Kumar, and J. Hahm, Adv. Mater. 18 (2006) 2685–2690.
8. C.S.S.R. Kumar (Ed.), Nanomaterials for the life sciences, V.1, Wiley-VCH, Weinheim, 2008, 572 p.

9. C.S.S.R. Kumar (Ed.), Nanomaterials for biosensors, V.8, Wiley-VCH, Weinheim, 2007, 408 p.
10. H.C. Yoon, M.Y. Hong, H.S. Kim, Anal. Chem. 72 (2000) 4420–4426.
11. M.E. Fragalà, C.Satriano, Y.Aleeva, G. Malandrino, Thin Solid films 518 (2010) 4484-4488.
12. W.I.Park, G.C. Yi, M. Kim, S.J. Pennycook, Adv. Mater. 14 (2002) 1841-1842.
13. P. Yang, H. Yan, S. Mao, R. Russo, J.Johnson, R.Saykally, N.Morris, J.Pham, R.He and H.-J. Choi, Adv. Funct. Mater. 12 (2002) 323-332.
14. S. Muthukumar, H. Sheng, J. Zhong, Z.Zhang, N. W.Emanetoglu, and Y. Lu, IEEE Trans. Nanotechnol. 2 (2003) 50-54.
15. J.Y. Park, D.J. Lee, Y.S. Yun, J.H. Moon, B.-T. Lee, S.S. Kim, J. Cryst. Growth, 276 (2005) 158-164.
16. D. Bekermann, D .Pilard, R.A. Fischer, A. Devi, ECS Transactions 25 (2009) 601-608.
17. D.-K. Hwang, M.-S. Oh, J.-H. Lim and S.-J. Park, J. Phys. D: Appl. Phys. 40 (2007) R387–R412.
18. A.A. Scalisi,R.G. Toro,G. Malandrino,M. E. Fragalà,G. Pezzotti, Chem. Vap. Deposition 14 (2008) 115-122.
19. M.E. Fragalà, C. Satriano, J. Nananosci. Nanotechnol. 10 (2010) 5889-5893.
20. A. Auditore, C. Satriano, U. Coscia, G. Ambrosone, V. Parisi, G. Marletta, Biomol. Eng. 19 (2002) 85-90.
21. G. Malandrino, M. Blandino, M.E. Fragalà, M. Losurdo, G. Bruno, J. Phys. Chem. C 112 (2008) 9595-9599.
22. K.H. Tam, C.K. Cheung, Y.H. Leung, A.B. Djurisic, C.C. Ling, C.D. Beling, S. Fung, W.M. Kwok, W.K. Chan, D.L. Phillips, L. Ding and W.K. Ge, J. Phys.Chem. B 110 (2006) 20865-20871.
23. K.G. Saw, K. Ibrahim, Y.T. Lim and M.K. Chai, Thin Solid Films, 515 (2007) 2879-2884.
24. D. D. Deligianni, N. Katsala, S. Ladas, D. Sotiropoulou, J. Amedee and Y. F. Missirlis, Biomaterials 22 (2001) 1241-1251.
25. J. Zhou, N. Xu and Z.L. Wang, Adv. Mater. 18 (2006) 2432-2435.
26. I. Lynch and K.A. Dawson, Nanotoday 3 (2008) 40-47.
27. T. Xia, M. Kovochich, M. Liong, L. Madler, B. Gilbert, H.B. Shi, J.I. Yeh, J.I. Zink and A.E. Nel, ACS Nano 2 (2008) 2121-2134.

28. A.E. Nel, L. Mädler, D. Velegol, T. Xia, E.M.V. Hoek, P. Somasundaran, F. Klaessig, V. Castranova and M. Thompson, Nat. Mater. 8 (2009) 543-557.
29. J.-C. Dupin, D. Gonbeau, P. Vinatier and A. Levasseur, Phys. Chem. Chem. Phys. 2 (2000) 1319-1324.
30. K. Kotsis and V. Staemmler, Phys. Chem. Chem. Phys. 8 (2006) 1490-1498.
31. M.E. Fragalà, C. Satriano and G. Malandrino, Chem. Commun. 7 (2009) 839-841
32. R.D. Tilton, A.P. Gast, C.R. Robertson, Biophys. J. 68 (1990) 1321-1326.
33. E.P. Vieira, S. Rocha, M.C. Pereira, H. Möhwald, M.A.N. Coelho, Langmuir 25 (2009) 9879-9886.
34. D. Axelrod, D.E. Koppel, J. Schlessinger, E. Elson, W.W. Webb, Biophys. J. 16 (1976) 1055-1069.
35. D. Weiskopf, E.K. Schmitt, M.H. Klühr, S.K. Dertinger, C. Steinem, Langmuir 23 (2007) 9134-9139.
36. W. Norde, Macromol. Symp. 103 (1996) 5-18.
37. C.K. Choi, J.D. Fowlkes, S.T. Retterer, P. Siuti, S. Iyer, M.J. Doktycz, ACS Nano 4 (2010) 3345-3355.
38. G.A. Parks, Chem. Rev. 65 (1965) 177-198.

7. Chemical bath deposition of ZnO nanostructured arrays

Introduction

In the previous chapters the vapour phase growth of ZnO in the range of temperature from 300 to 700 °C allowing the formation of thin films and nanorods is presented. Nevertheless, the present technological demand presses towards flexible, low cost, easily scalable and reproducible approaches. Therefore, solution growth methods involving liquid phase deposition strategy are currently attracting considerable efforts of research activity as bottom-up strategies to form one-dimensional ZnO nanostructures [1,2]. In fact, wet chemistry based methods are versatile, low cost, environmental friendly techniques and allow large-scale production on almost every kind of substrates [3]. Even more important, CBD favours an accurate control of the morphology and the orientation of ZnO nanostructures by tuning the process parameters through the relevant equilibria that are established in the solution [4]. Although various shapes of ZnO are obtained via CBD, the systematic control of crystal shape still remains a challenge [5,6].

The basic idea of solution growth involves multistep “nucleation-growth” processes. Lowering the interfacial energy barrier is the central consideration for heterogeneous nucleation.

The methodology of the solution growth of crystals on a seed is the establishment of growth conditions in which the process is represented by the sum of macro- and micro-processes occurring between the interface boundary of the solution and the crystal. The composition and concentration of the solution, temperature and pressure, hydrodynamic conditions, and surface contact of the phases are some of the basic physical and chemical parameters which determine the regime and rate of dissolution of the nutrient, mass transport, and possibility of the formation of new phases.

One way to reduce the interfacial energy can be the use of organic additives, called capping agents or structure-directing agents, were proven efficient in tuning the size and shape of nanocrystals, mainly by manipulating the surface activity [1,2]. The role of capping agents is to introduce secondary nucleation sites on initial structures by reducing the interfacial activation energy.

Epitaxial growth is another way of lowering the interfacial barriers. Substrates with small lattice mismatch to the overlayer materials have been extensively chosen to guide the assembly of one-dimensional (1D) nanoarchitectures.

Lately, homoepitaxy routes are commonly used for ZnO nanoarrays formation and a homologous seed layer is often required to promote the uniform growth of oriented nanorods from aqueous solutions. Although it has been shown [7] that hydrothermal ZnO growth can occur without seed layers, most of the literature related to aqueous solution hybrid approaches has been focused on the formation of nanorods using homoepitaxial ZnO seed layer, such as crystals or thin films [8-11].

In fact, the presence of nucleation sites lowers the CBD thermodynamic barrier, improves the aspect ratio of the obtained nanorods [9, 10] and favours a better uniformity [11]. Nucleation sites can be introduced through a seed layer of ZnO deposited by drop casting, sputtering or spin coating of Zn (II) sols onto the substrates, with a following post-annealing to favour ZnO crystal growth. Recently, the decomposition of zinc acetate at 200 – 350 °C has been proposed to produce nucleation sites for ZnO nanowires [12-14]. Moreover, it has been shown that pre-coating of glass and silicon substrates via sol-gel/spin coating [14-18], annealing of either RF sputtered [19] or MOCVD [20-22] deposited seed layers enhances texturing and crystallinity and is crucial for the formation of aligned ZnO nanowire/nanorod overlayers with improved properties.

To realize the preferable growth along a longitudinal direction, especially to regulate the aspect ratio of the produced nanorod/nanowire structures, the degree of supersaturation of the solution also has to be taken into the consideration, so that the growth of the pre-existing particles is favourable compared to the formation of new nuclei [4].

In fact, the general procedure for the solution based growth requires the substrate coating with a ZnO seed layer (thin film). Later, the substrate is immersed into a water solution supersaturated with zinc salt, amines (complexing agent) and other ions. When the solution is heated up (50-90°C) micro/nano structured ZnO is formed on the seed layer by heterogeneous nucleation and growth from the hydrolysis of zinc salts. However, supersaturated solutions form unstable clusters that can produce precipitates either on the substrate or in solution. Therefore, according to classical crystallization theories, the supersaturation degree is a significant parameter affecting the nucleation process, for both homogeneous or heterogeneous nucleation. In fact, homogeneous precipitation is favoured under a high supersaturation degree, while heterogeneous nucleation growth would be favoured in a lower supersaturation region. It competes with the heterogeneous mechanism that favours the deposition at the solid/solution interface. The heterogeneous process prevails during the initial step of CBD while, upon increasing the growth time, the homogeneous growth acts as a stopping process, thus inhibiting the further growth of nanostructures. In fact, at the end of the CBD process, the grown ZnO nanostructures present bimodal morphology consisting of an underlying nanorod arrangement covered with porous and poorly adherent, microstructure agglomeration (Fig. 7.1). However, rinsing with distilled water has proven to be effective to remove homogeneously deposited ZnO agglomerates from the substrates and to obtain clean and well adherent nanorod arrays.

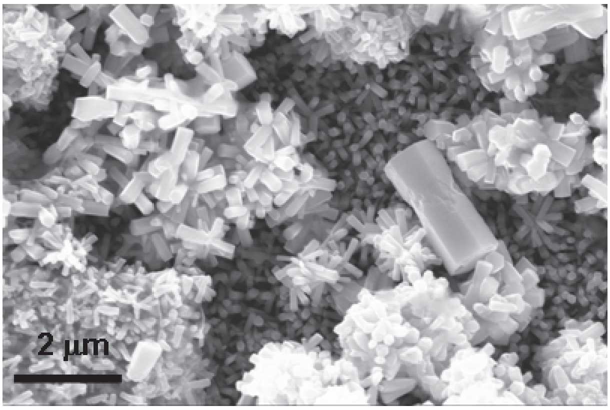

Figure 7.1: SEM image of ZnO nanostructures deposited on ZnO seeded substrates at the end of the CBD process, before washing steps.

In principle, the primarily formed structure could serve as substrate to initiate the secondary heterogeneous nucleation on the condition that the remaining concentration is sufficiently high to initiate nucleation and the interfacial energy of nucleus/substrate is lower than that of particle/solution. However, the research on such in situ hierarchical organization is limited probably due to the complicated kinetic processes. [23].

In addition, the low-temperature aqueous solution strategies used to grow ZnO nanostructures are fully compatible with emerging strategies devoted to the patterned growth of ordered ZnO nanostructure arrays by employing monolayer colloidal crystals. In fact, colloidal lithography has been proven to be a flexible and cost-effective technique for the patterning of nanostructured arrays with long-range periodicity in a large scale [24].

Herein, a systematic study of effects of morphologies of ZnO seed layers, deposited via thermal reduction of drop casted zinc acetate ethanolic solution and MOCVD grown ZnO films on Si substrates in a wide temperature ranges (300 °C–600 °C) and deposition times (10 – 60 min), on the properties of ZnO nanorods fabricated using a following CBD process is presented.

Moreover, a new method to obtain ZnO nanoplatform on glass substrates by integration of metal - organic chemical vapour deposition (MOCVD) with nanosphere colloidal lithography (NSCL) and chemical bath deposition (CBD) approaches is suggested. Ordered ZnO nanoplatforms have been recently investigated to study protein adsorption processes and have demonstrated interesting potentialities as fluorescence based sensor [25,26]. The interaction of the newly deposited materials with a model biomolecule (fluorescein-labeled albumin) was investigated by fluorescence recovery after photobleaching (FRAP) experiments.

Results and discussion

Herein, we demonstrate the growth of ZnO nanostructures at 70 °C and in near-neutral pH conditions using various seed layers. It is well known that growth of any overlayer requires uniform and well oriented seeds underneath [27-29]. Seeding, in turn, involves stringent requirements to favour one-dimensional monocrystal growth without lateral transport of matter. In fact, the ZnO nanorods nucleate directly on the ZnO seeds or at their boundaries and, therefore, the vertical alignment of the nanorods heavily depends on the orientation of the seeds. Generally adopted seeding strategies include sol-gel spin coating or dip-coating followed by high temperature treatments or, perhaps, physical methods, like sputtering [19,27]. Seeding from chemical vapour deposition, has been poorly investigated despite it represents a low cost, viable and easily tuneable source using a large variety of operational parameter and sources. It requires simple and low/ambient pressure apparatus, while favouring conformal deposition well suited for complex shapes.

Nevertheless, despite some systematic studies have investigated the effects of annealing treatments of the ZnO buffer layers deposited by MOCVD in the perspective of improving the properties of the subsequently deposited CBD ZnO main layer [21,22], the impact of changes of buffer layer properties upon varying the MOCVD deposition temperature on the final morphology of the CBD grown ZnO nanorod arrays has been never scrutinized.

In the present case the growth of ZnO nanorods from seed layers deposited from ethanolic solutions containing zinc acetate dehydrate or via MOCVD of ZnO films on quartz and silicon substrates (see Chapter 3) is studied. ZnO buffer layers were obtained by annealing at 150 ^{o}C the substrates drop casted with ethanolic zinc acetate salt solution, whereas ZnO buffer layers grown by MOCVD were deposited within 300 °C - 600 °C range from the $Zn(tta)_2 \cdot tmeda$ precursor [30].

Although the deposition temperature represents the most critical parameter of any CVD process, other parameters, including the precursor evaporation temperature and the O_2 reacting gas partial pressure, no doubt can be explored to tailor structure, morphology and properties of growing film. Experimental data have clearly demonstrated that clean and pure ZnO films require setting of the evaporation source temperature at 170° C and of the flow of the O_2 reacting gas at 250 sccm (see Chapter 4).

Effects of seed deposition approach and MOCVD deposition temperatures on morphology and on crystal structure of ZnO buffer layer have been further studied by SEM and AFM microscopies, and XRD.

Figure 7.2 (a) revealed that seed layer obtained by drop casting method with post-annealing represents thin film non-uniformly distributed on the substrate surface. As to the MOCVD grown seed layers, SEM images provide evidence that ZnO growth proceeds through an island mode growth (Fig. 7.2 (b)). At low temperature (300 °C) a discontinuous film structure, characterised by hexagonal flakes, is therefore well evident. As the temperature increases, in particular in the 400 °C- 600 °C range, the films become continuous as a consequence of island coalescence and the granular structure changes from smaller (Fig. 7.2 (c)) to larger and more geometrically defined grains (Fig. 7.2 (d,e)). The inferred thickness ranges from ~ 50 nm for the samples deposited at 400 °C to ~ 150 nm for those deposited at 600 °C. The thickness of samples deposited at 300 °C can be hardly detected due to the flaky nature of the layer.

The AFM analyses (Fig. 7.3) match well SEM morphologies. It, therefore, transpires that 300 °C represents a temperature threshold between two dif-

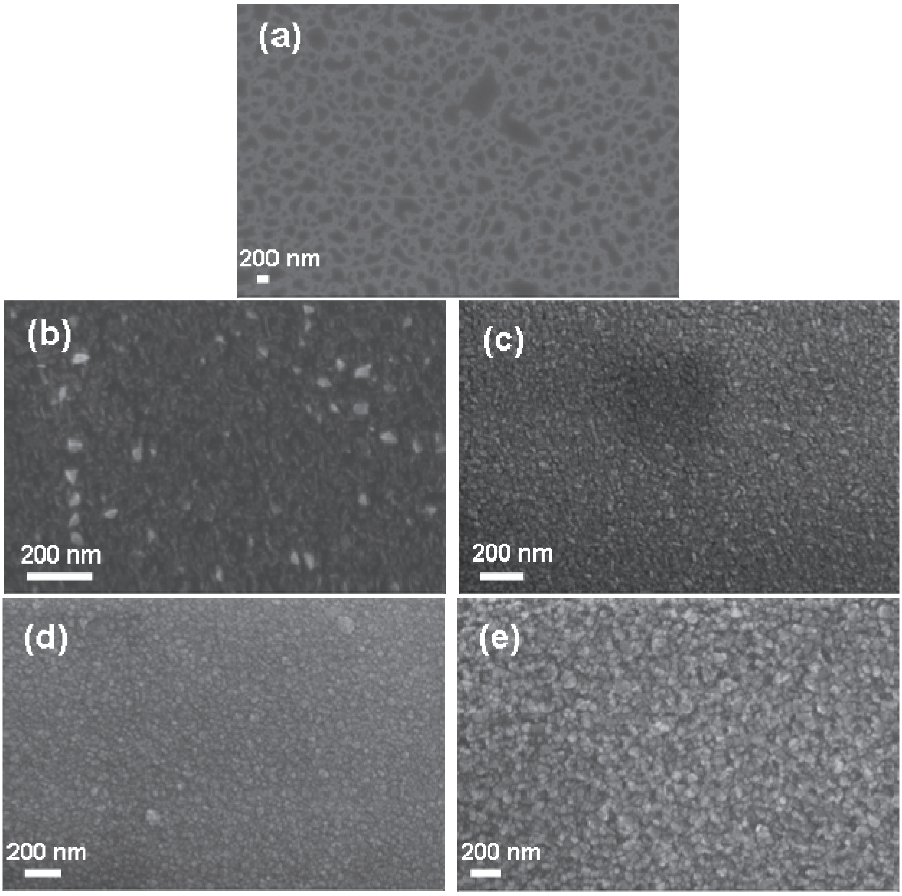

Figure 7.2: SEM images of ZnO buffer layers deposited on Si substrates by drop casting (a), MOCVD at 300 °C (a), 400 °C (b), 500 °C (c) and 600 °C (d).

ferent MOCVD growth modes. In fact, at this temperature, disordered flakes are associated with an island growth involving a partially covered substrate and, hence a high surface root mean square (RMS) roughness (~ 12 nm). Above this threshold, a continuous layer becomes predominant and the smoother morphology (RMS ~ 2–4 nm) appears controlled by the deposition temperature with greater grains and related RMS values linearly increasing parallel to the temperature evolution (Figure 7.4). These findings match well previously reported data [30].

This behaviour can be related to quality of films. XRD data show that drop casted annealed seed is amorphous (Fig. 7.5), whereas MOCVD grown seeds are crystalline. The crystallinity becomes better upon increasing the temperature and, hence, upon increasing the mobility of ad-atoms over the substrate.

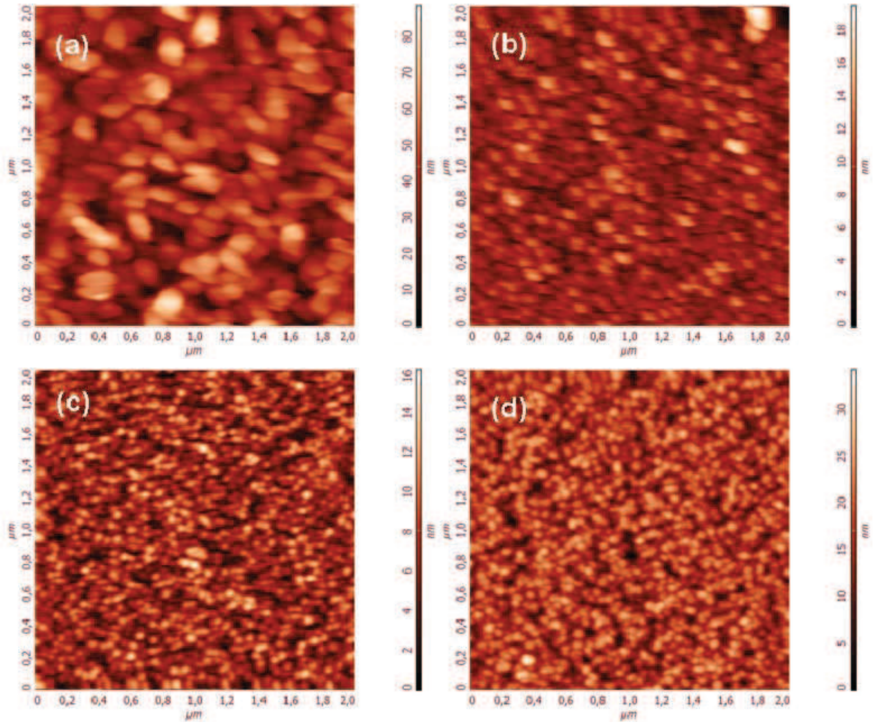

Figure 7.3: AFM images of ZnO buffer layers deposited on Si substrates by MOCVD at 300 °C (a), 400 °C (b), 500 °C (c) and 600 °C (d).

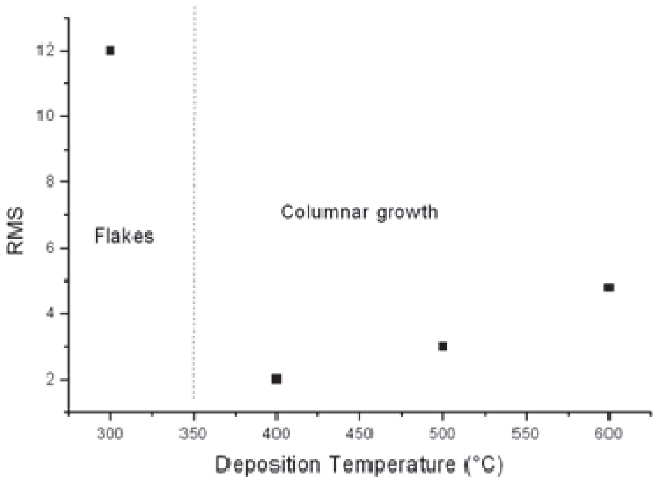

Figure 7.4: Root Mean Square (RMS) roughness of ZnO buffer layers vs MOCVD deposition temperature

Therefore, under low temperature/mobility regimes, full crystallization of films is precluded in accordance with the slightly discernible XRD pattern of films deposited at 300 °C and 400 °C (Fig. 7.5). Note, however, that the negligible thickness of films must be considered to account for the poor XRD signal. Upon increasing the temperature, a high mobility is favoured and ad-atoms arrange in well suited positions for crystal growth. Thus, at 500 °C the (002) peak ($2\theta = 34.40°$) becomes narrow (0.30°). The peak further shifts to $2\theta = 34.50°$ at 600 °C, with an even narrow FWHM (0.25°) [20,31].

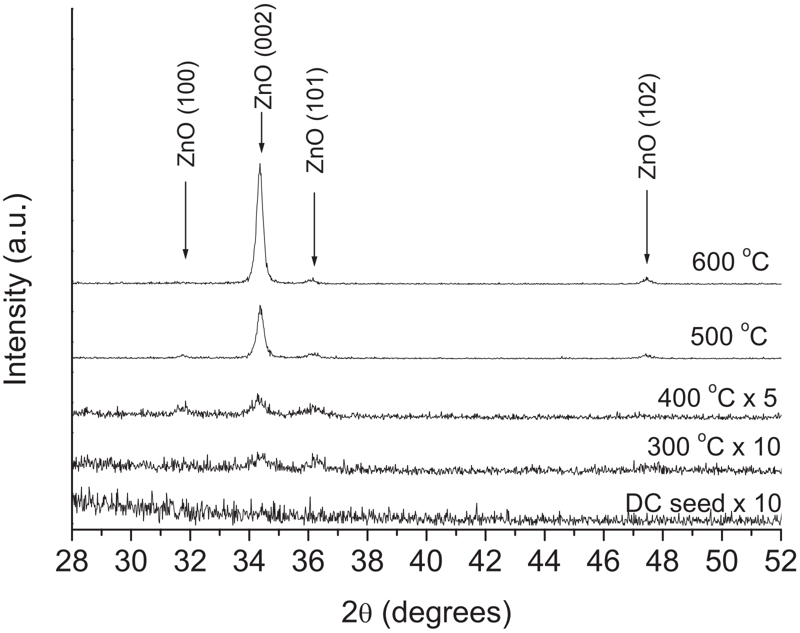

Figure 7.5: XRD patterns of ZnO buffer layers obtained by drop casting and MOCVD at different temperatures respectively

ZnO nanostructures have been grown on these seeded Si substrates by chemical bath deposition method (CBD). Hexamethylenetetramine (HMT) is one of the most used ligand in ZnO CBD process [4,16,19]. ZnO nanorod formation is promoted by HMT thermal decomposition, that provides hydroxide ions (OH^-) and ammonia molecules (NH_3) to the solution [4,32], but the control of the several equilibria involved in the process is critical. Other Lewis bases, such as ethylenediamine (EDA) and triethanolamine (TEA), have been used in ZnO CBD as effective complexing agents for the Zn^{2+} ions and speciation calculations [4] have indicated the pH conditions required to form ZnO, according to zinc hydroxide supersaturation values. Despite pH of nutrient bath is another important factor that control CBD mechanism, it has been found that ZnO films and nanostructures can be formed also without pH adjustment of bath solution. In this context, literature reports on a wide selection of Zn complexing agents used in CBD [4,32-35].

As a matter of choice the N, N, N', N' -tetramethylethylenediamine, often used in the metal-organic precursor synthesis [36] and related MOCVD deposition [30] can be considered as an effective ligand for Zn^{2+}. This Lewis base is comparable to ethylenediamine, but its Zn^{2+} complexing capability is lower with respect to latter. The hydrolytic equilibrium of the related complex controls the overall CBD growth, by a gradual release of Zn^{2+} and OH^- reactants. At 70 °C the dissociation equilibrium of $[Zn(TMEDA)_n]^{2+}$ is perturbed and the amino-ligand undergoes basic hydrolysis [37,38]:

$$[Zn(TMEDA)_n]^{2+} \leftrightarrow Zn^{2+} + TMEDA \qquad (7.1)$$

$$TMEDA + H_2O \leftrightarrow TMEDA\text{-}H^+ + OH^- \qquad (7.2)$$

$$Zn^{2+} + OH^- \rightarrow Zn(OH)_2\downarrow \rightarrow ZnO\downarrow + H_2O \qquad (7.3)$$

Several authors [4,32,33,39] have reported on the buffer effect played by the amino-based ligand during the CBD. No doubt, in fact, that equilibria 7.1 and 7.2 regulate the concentration of the Zn^{2+} and OH^- ions in the solution. Thus, when their ionic product (IP) exceeds the $Zn(OH)_2$ solubility product constant (K_{ps}) the precipitation of ZnO nuclei becomes activated, due to the presence of free Zn^{2+} and OH^- ions. $Zn(OH)_2$ and ZnO are thus formed in the aqueous solution. The precipitates of $Zn(OH)_2$ are more soluble, compared to the ZnO precipitates, and therefore, they represent a reservoir of Zn^{2+} and OH^- ions, which, in turn, form the ZnO nuclei that represent the building blocks for the formation of the nanorods.

The variation of the concentration of the complexing agent, of course, modifies the OH^- concentration and, hence, enhances the film growth rate. On the other hand, it increases the solution supersaturation level [40] (which promotes an undesirable bulk precipitation), thus leading to the reduction of the film growth. In particular, it is known that in ZnO CBD, the homogeneous growth mechanism is promoted by the deposition of ZnO clusters formed in the solution [41]. It competes with the heterogeneous mechanism that favours the deposition at the solid/solution interface [42-44]. The heterogeneous process prevails during the initial step of CBD while, upon increasing the growth time, the homogeneous growth acts as a stopping process, thus inhibiting the further growth of nanostructures.

In this general context, a successful strategy has been presently developed and it has proven capable of growing, on seeded silicon substrates, ZnO nanorods, with a perfect hexagonal shape throughout their lengths and preferentially oriented along the c-axis direction. Particular attention has been devoted to study the effect of TMEDA ligand concentration, growth time, bath chemistry used on CBD of ZnO nanorods and to define clean and reproducible procedures to obtain nanostructures having tailored density and dimensions. There is evidence that the ligand above mentioned parameters affect both the length and the width of the ZnO nanorods, as well as shape, thus, resulting in a different nanostructure density.

The growing ZnO nanostructures show a strong correlation between their morphologies and those of the seed layer underneath. Figure 7.6 (a,a’) shows the SEM images of sample formed on the drop-casted annealed seed layer. The SEM cross section image indicates nanorod growth having diameter of ~ 200 nm. It is evident from the SEM images, that the top surface of these nanorods appears smooth and hexagonally shaped whilst the lateral sides look porous and not yet geometrically well defined. SEM data also point to nanorod length 500 mm (Fig 7.6 (a’)), unfortunately associated with the out-of-vertical alignment. As to the ZnO grown on MOCVD grown seed layers, the ZnO nanorods grown by CBD on seed layer deposited at 300 °C (Fig. 7.6 (b,b’)) also appeared to be slanted and geometrically not well defined. This can be related to flake-like buffer layer with an island morphology, not uniformly covering the silicon substrates. SEM cross section images (Fig. 7.6 (b)) estimate a mean diameter of ~ 100 nm. The seed layer is slightly visible in the cross section, due to the flaky nature and thickness discontinuity. The overall stack length is ~ 400 nm (Fig. 7.6 (b’)). On passing to ZnO buffer layers deposited at 400 °C, the related ZnO CBD nanorods show the expected hexagonal shape. Moreover, nanorods possess more homogeneous dimensions distribution with an average diameter of ~ 200 nm and a length of ~ 400 nm (Figure 7.6 (c,c’)). The seeding layer is well discernible in the cross section with a thickness of about 60 nm (overall stack length of ~ 460

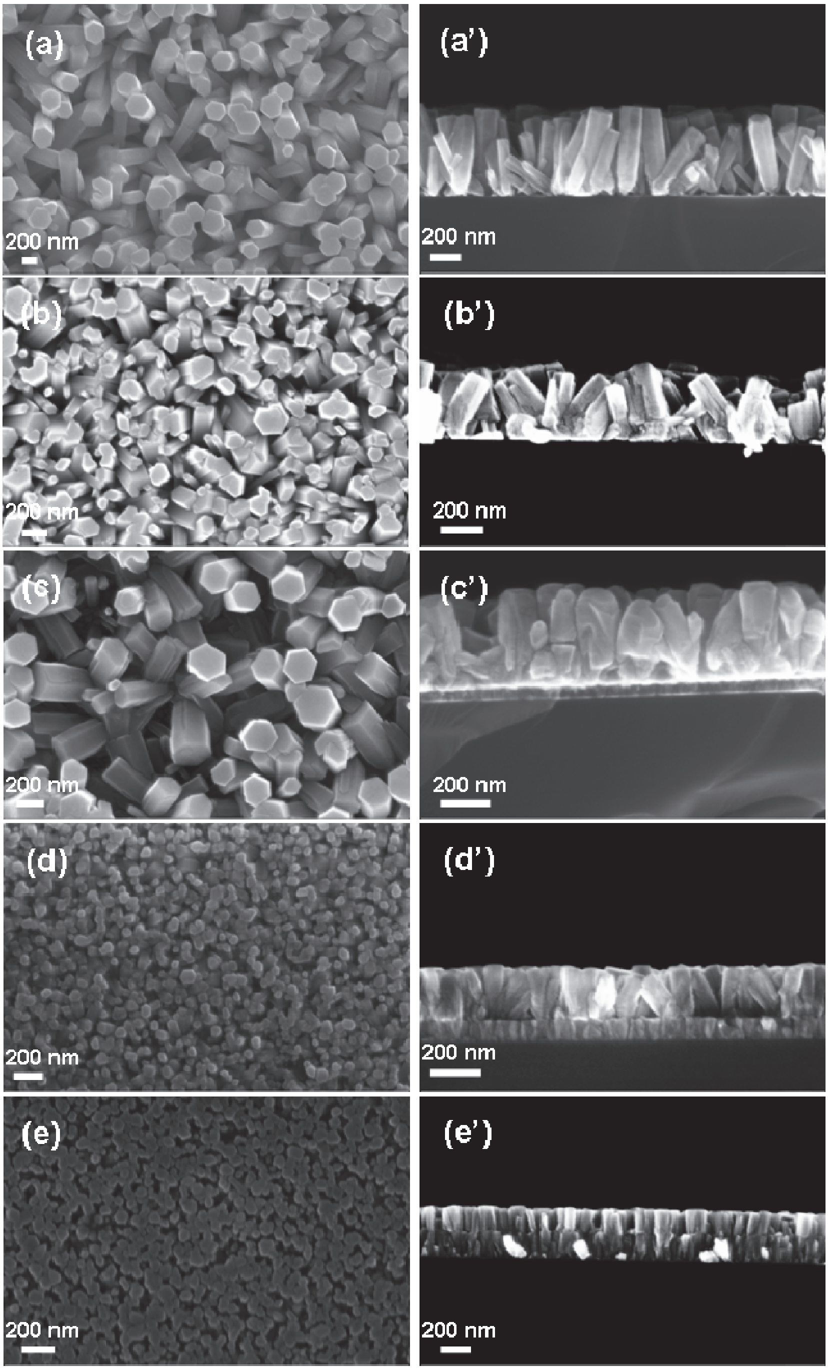

Figure 7.6: SEM plane view and cross-section view of ZnO nanorods grown by CBD (25 mM) for 2 h on: buffer layer deposited by drop-casting of zinc (II) solution (a, a'), buffer layer deposited by MOCVD at 300 °C (b, b'), at 400 °C (c, c'), 500 °C; (d, d'), at 600 °C (e, e').

nm). Despite the dense buffer layer, the CBD ZnO nanorods still result in poorly vertically oriented arrays. This observation matches well with the low crystallinity of the buffer layer, in accordance with the XRD analysis (Fig. 7.5). By increasing the deposition temperature at 500 °C, both the thickness (~ 110 nm) and crystallinity of the buffer layer increase, thus acquiring a columnar-like shape. As a consequence, the related CBD ZnO nanorods (Fig. 7.6 (d,d')) appear more vertically oriented, thinner (mean diameter ~ 60 nm) and somewhat shorter (~ 260 nm). In addition, due to the reduced diameter, the mean surface density (number of nanorods/surface unit) is dramatically increased and a dense ZnO nanorods array is formed after CBD (overall stack length of ~ 370 nm). Finally, there is evidence that at the highest deposition temperature (600 °C) the seed layer consists of a primary array of ZnO nanorods (length ~ 150 nm) on which a second array is replicated by CBD (Fig. 7.6 (e,e')). The almost perfect matching of both diameters (~ 100 nm) results in final CBD grown ZnO nanorods of about ~ 180 nm length (overall stack length of ~ 330 nm).It is noted that more structured seed layers lead to the growth, by CBD, of shorter and thinner (~ 100 nm) ZnO nanorods as consequence of the comparable mass transport (same bath concentration and growth times) over a remarkably increased number of active sites. Therefore, the surface roughness acts as nucleation sites for nanorods growth [45]. Similar arguments can be invoked to understand the increase of nanorods density upon increasing the MOCVD deposition temperatures of the ZnO seed layers.

It has been already noticed that the morphology of the seed layer evolves from a granular structure to nanorods upon increasing the related MOCVD deposition temperatures. This trend, conversely, increases both the related surfaces-to-volume ratio and the numbers of active centres responsible for the heterogeneous nucleation at the ZnO buffer surface and CBD solution interface, thus increasing the overall nanorods density. It, therefore, transpires that thinner nanorods find counterpart in more dense structures.

Results provide evidence of slower growth rates upon increasing the overall roughness and morphological complexity of seed layers. Meanwhile, the density of nanorods per unit area is larger as a consequence of the smaller diameter of the nanorods.

Of course, greater morphological complexities involve a large number of nucleation sites that can be accessed by the ZnO precursor in the CBD solution. In this case, the local precursor (Zn^{2+} and OH^-) concentration at the solution-substrate interface is decreased, thus slowing down the overall growth rate. It is worthy of note that CBD ZnO growth on thin amorphous ZnO seed layers have similarly found that the related growth rates are greater than those over crystalline substrates. It, therefore, transpires that, at higher nucleation densities, the gradient concentration experienced by each nucleation site fall-off, thus producing shorter and thinner nanorods.

Interesting enough, XRD patterns (Fig. 7.7) provide evidence of the influence of the crystallographic nature of underlying layers on c-axis texturing of CBD nanostructures upon increasing the MOCVD deposition temperature. In particular, for ZnO nanostructures grown on amorphous layer or on seeds deposited at 300 °C and 400 °C typical wurtzite diffraction pattern is slightly visible, while upon increasing the seed deposition temperature to 500 °C and 600 °C, the crystallynity improves and the (002) orientation becomes dominant with respect to (100), (101) and (102) peaks respectively. This is due to the fact that both the better orientation and crystallization of the nuclei of the seed layer favour a higher (002) texturing CBD nanorods.

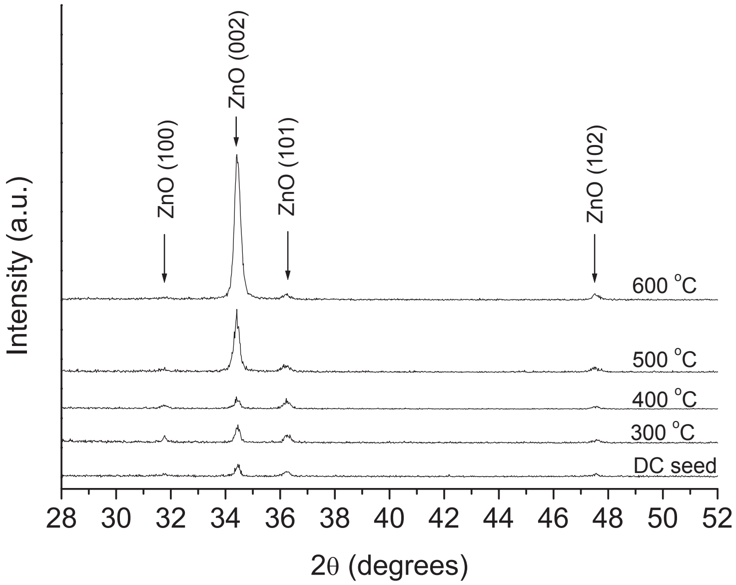

Figure 7.7: XRD patterns of ZnO nanorods grown by CBD (25 mM, 2 h) on various buffer layers

Nevertheless, both the better defined hexagonal geometry and the sidewall compactness point to some lateral mass uptake that competes with the top vertical elongation, after an induction period. The aspect ratio of the CBD ZnO nanorods is governed by the relative growth rates of the polar [001] and of the non-polar [101] and [100] surfaces [46-48]. ZnO, in fact, exhibits partial polar characteristics having the opposite ends of (001) plane of the zincite crystal positively (Zn^{2+}) and negatively (O^{2-}) charged. This leads to a high surface energy for these polar planes. Lower energy non-polar planes are thermodynamically more stable and, hence, the CBD growth process favours nanorods growth along the [0001] direction where the large facets are usually the non-polar planes. Nanorods are, therefore, c-axis textured to minimize the exposed surface area of the polar facets and to reduce the surface energy.

Additionally, seed layers having higher roughness might, in addition, cause nanorods coalescence effects. In fact, not enough smooth at the nanoscale level) substrates have nucleation seeds with the (001) planes not parallel to the substrate. Growing nanorods, therefore, mismatch the c-axial direction, merge with other nanorods and larger nanostructures are produced. Thus, nanorods grown over flake-like substrates appear extremely slanted with coalesced nanostructures and a wide size distribution. Therefore, we can conclude that seed layer deposited above 500 °C is effective to grow 1D ZnO crystalline nanorods, while seed deposited at lower temperatures or by drop casting result in more slanted and polycrystalline nanostructures.

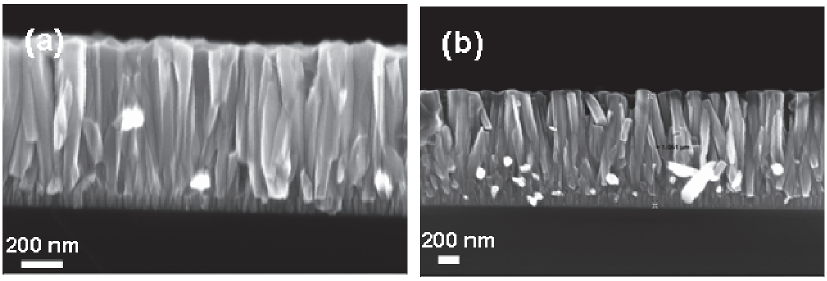

Figure 7.8: SEM cross-section view of ZnO nanorods grown by CBD (25 mM) on buffer layer deposited by MOCVD at 500 °C/60 m for 6h (a) and 8h (b).

Growth time is an additional factor that affects the nanorod density and their final length. Thus, the overall nanorod dimensions obtained using the 2 h growth are smaller than the structures grown in 6 h period, having a diameter of ~ 80 nm (Fig. 7.8 (a)). Moreover, the nanorod length increases from 260 nm to

750 nm (Fig. 7.6 (d) and 7.8 (a)) upon increasing growth time from 2h to 6h (using seed grown at 500 °C/60 min). Longer growth times (8 h) cause the densification of the nanorods having diameter of 100 nm and the length increase to 1 μm (Fig. 7.8 (b)).

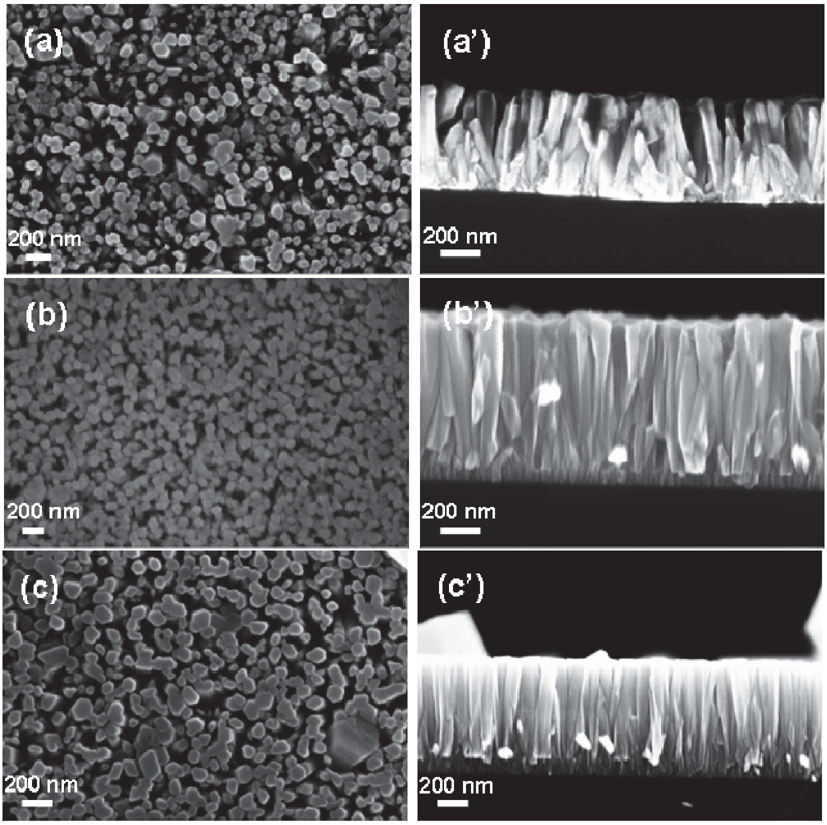

Figure 7.9: SEM images of ZnO nanorods grown by CBD (25 mM, 6 h) on buffer layer deposited by MOCVD at 500 °C for 10 min (a, a'); 30 min (b, b') and 60 min (c, c').

Moreover, a strong correlation has been presently found between the seed layer thickness and the CBD growth rate. Thus, ZnO buffer layers deposited by MOCVD at 500 °C for 10 minutes (Fig. 7.9 (a,a')) and 30 minutes (Fig. 7.9 (b,b')) have been subjected to 6 hours CBD growth and the length of the obtained ZnO nanorods has been compared to that obtained on the buffer layer deposited at the same temperature, for 60 minutes (Fig. 7.9 (c,c')). It has been observed that reduction of the MOCVD deposition time to 30 minutes results in a ~ 70 nm thick seed layer with an overall length of ZnO nanorods increased to 850 nm (*vs* 750 nm obtained on thicker seed layer deposited for 60 minutes, Fig. 7.9 (c,c') and the density of the ZnO nanorods similarly increased. The further reduction of the seeding time to 10 min certainly causes a thinner and not uniform buffer layer (not detectable in the SEM cross section), that leads to a reduction of the CBD growth rate. Therefore, the ZnO nanorods (Figure 7.9 (a,a')) growth over buffer layer deposited at high temperature (500 °C) and short deposition time (10 min) resembles that obtained on seeds deposited at lower temperature (300 °C, Fig. 7.6 (b,b')). This is the result of non uniform thickness due to less controlled MOCVD deposition conditions. The neo formations show, in addition a great dispersion of the sizes and a decreased nanorod densities.

To conclude, the thickness of the seed is an additional factor that impacts on the overall quality of the ZnO nanorods and on the related growth rates. In particular, greater growth rates are observed in the case of thinner seed layers [28], providing a totally uniform thickness over the whole substrate. In this context, drop-casted layer and MOCVD seed layers at lower deposition temperatures (300 °C) or at shorter process times (10 min), are poorly uniform and not suitable for high quality CBD ZnO nanorods growth. High quality and uniform MOCVD seed layer, with a strong c-axis orientation are, thus, required for high density and well aligned ZnO nanorods by CBD.

Table 7.1: Dimensions and growth rates of ZnO nanorods vs TMEDA concentration.

[TMEDA], mM	d, nm	l, nm	Growth rate, nm/h
15	60	530	90
25	80	850	140
50	100	1150	190

Nanorods length has been also tailored by changing the nutrient bath concentrations [4], namely by increasing the Zn acetate and TMEDA concentrations, keeping constant the (TMEDA/Zn^{2+}) ratio [38]. There is evidence that CBD growth(on ZnO buffer layer deposited at 500 °C for 30 min) promotes formation of ZnO nanorods whose growth rates, diameters and lengths vary upon changing the nutrient bath concentration (TMEDA 15mM, 25mM and 50mM). In particular, the nanorods aspect ratio (AR = length/diameter) increases upon increasing the concentration (Table 7.1) as shown in the prototypical SEM images reported in Figures 7.9 (b,b’) and 7.10.

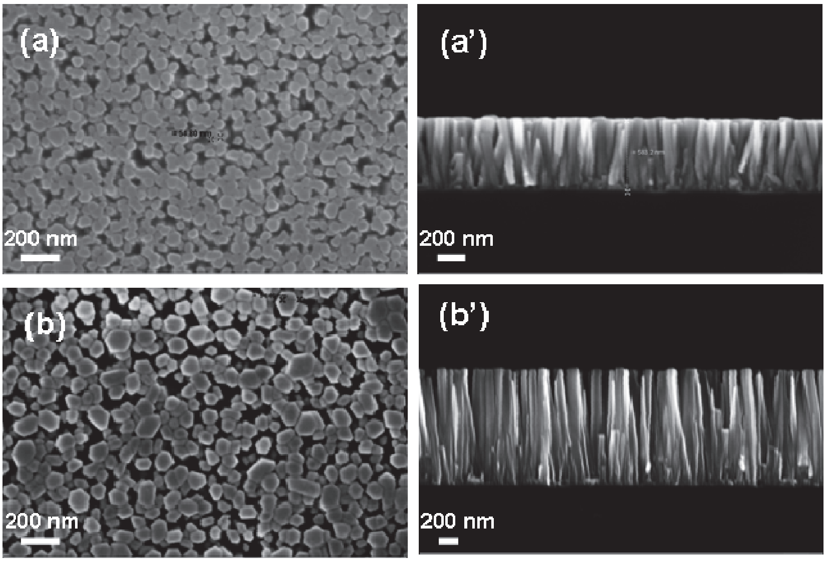

Figure 7.10: SEM images of ZnO nanorods grown by CBD (6 h on 500 °C/30 m buffer layer) at using different TMEDA concentrations, 15 mM (a, a’) and 50 mM (b,b’).

This observation agrees well with a prevalent c-axis oriented growth *vs* a lateral growth. Moreover, there is evidence that lower TMEDA concentrations (15mM) result in nanorod arrays of greater density (Figure 7.10 (a,a’)) compared to higher concentrations (50 mM) (Figure 7.10 (b,b’)). It is worthy of note that the higher precursor concentrations per unit area seems to promote the growth of nanorods having a larger diameter as a possible consequence of coalescence phenomena.

Precursor concentrations (Zn acetate and complexing agent/base) in the nutrient bath are also usually viewed as critical factors to control the aspect ratio and surface density of ZnO nanorods [4]. Present data agree well with a trend [49] of increasing rates upon increasing the concentration with structures having a predominant c-axis texturing and greater aspect ratio (see Table 7.1).

Ethylendiamine (EDA) and tetraethylenepentamine (TEPA) have also been used as alternative to TMEDA ligand. It has been observed that EDA promotes much slower ZnO growth comparable to TMEDA. On the contrary, TEPA has not led to any growth due to the high pH (~ 10) thus affecting the supersaturation regime of the nutrient solution.

The XRD patterns (Fig. 7.11) confirmed the crystalline nature of the nanorods with predominant c-axis orientation while using EDA and TMEDA as chelating agents.

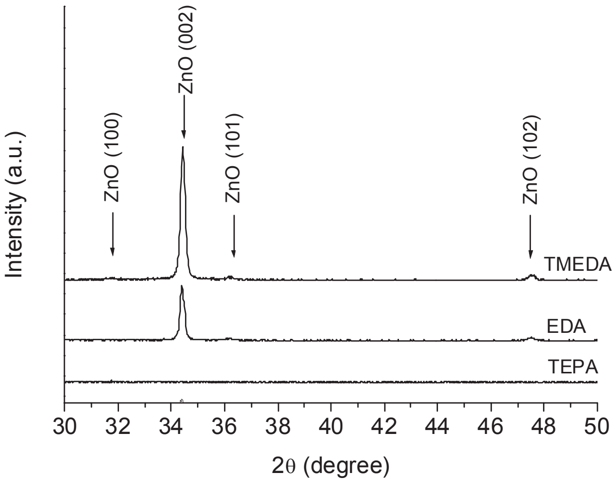

Figure 7.11: XRD patterns of ZnO nanorods grown by CBD (25 mM, 2 h) using various ligands

Comparison of SEM images of ZnO nanorods from TMEDA in the present study (Fig. 7.10 (a,a')) with those obtained from EDA (Fig.7.12), under similar bath chemistry, leads to the following conclusions. Firstly, the nanostructure morphologies are different. In the case of TMEDA the rods have flat smooth hexagonal surfaces (Fig. 7.10(a,a')), while in case of growth from EDA the sword-like nanostructures having conical tops formation is observed (Fig. 7.12). Moreover, the growth rate is reduced 3 times if the EDA is used instead of TMEDA leading to formation of nanostructures having length of ~ 200 nm.

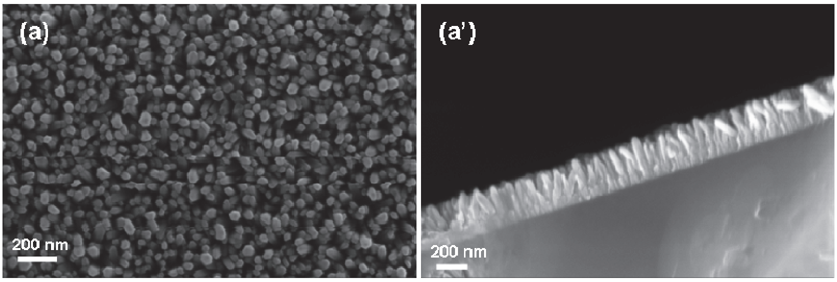

Figure 7.12: SEM plane (a) and cross-section (a') images of ZnO nanorods deposited using 15mM EDA ligand for 6 hrs on 500°C/30m grown seed layer

Photoluminescence measurements provide important information about the crystal quality of ZnO nanostructures. The optical response of the ZnO nanorods obtained by the combination of seed layer (400 °C) and CBD deposition conditions (TMEDA 50 mM) resulting in the faster growth rate has been scrutinised. Figure 7.13 shows the room-temperature photoluminescence (PL) spectra of ZnO nanorods grown on low temperature (400° C) MOCVD deposited seed layer. The poorly crystalline seed layer presents a wide weak ultraviolet band-edge emission peak centred at ~ 390 nm. After the CBD growth, despite the poor ZnO nanorod alignment, photoluminescence measurements show a strong UV emission at 377 nm along with a weak and broad green emission around 550 nm (Fig. 7.13). The band-edge emission is typically related to recombination of free excitons [50], while the visible green emission is associated with the structural defects of oxygen vacancies [51].

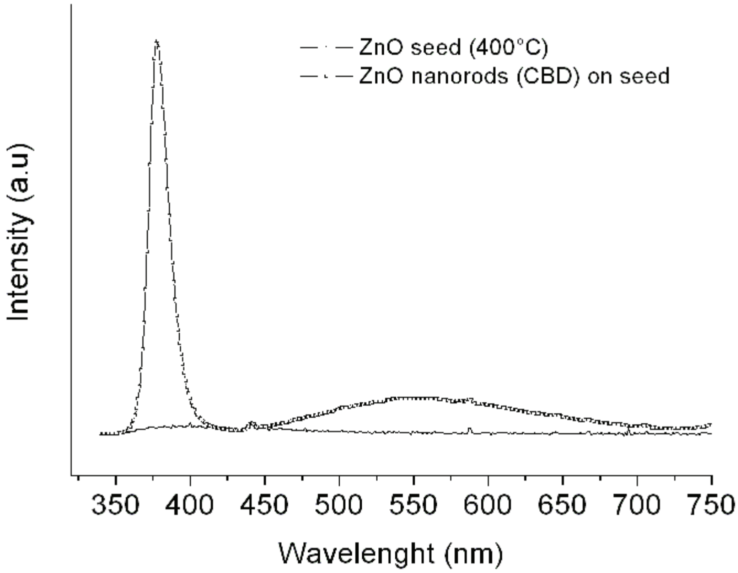

Figure 7.13: Photoluminescence spectrum of ZnO nanorods grown by CBD (50 mM, 2 h) on seed layer deposited at 400 °C.

The band-edge emission peak is very sharp and narrow (FWHM= 14 nm) and the large intensity ratio of UV to green PL points to the high crystal quality of ZnO nanorods, despite the low crystallinity of the seed layer. In fact, the relative high PL intensity ratio between the UV and green emissions (~ 10) indicates that ZnO nanorods have low deep level defect concentration. The predominance of the UV peak over the weak green band ($I_{UV}/I_{Green}=10$) provides a clear evidence of the high optical and crystalline quality of the ZnO neo-formations, despite their poor vertical alignment. It can be concluded that higher concentration of CBD bath can improve the crystal quality, growth rate and optical properties of the corresponding ZnO nanorods, despite the crystal quality of the ZnO seed layer.

To summarise, a simple two step-solution route is developed to grow ordered ZnO nanorod arrays (Fig. 7.14). Accurate control of growth parameters such as choice of seed and ligand, ligand concentration, growth time allow to fabricate high quality ZnO material having high surface to volume ratio.

In previous Chapter, the successful fabrication of nanostructured arrays is presented by two-step NSCL-MOCVD approach. Herein, particular efforts were concentrated to achieve a controlled growth of patterned ordered arrays in solution. To do so, we present 3 step fabrication strategy, involving MOCVD-NSCL-CBD strategies. The fabrication of the present ZnO nanoplatforms requires the initial formation of ZnO seed, obtained by MOCVD, followed by self-assembly of PS microsphere masks and subsequent CBD growth of ZnO nanorods (Fig. 7.14).

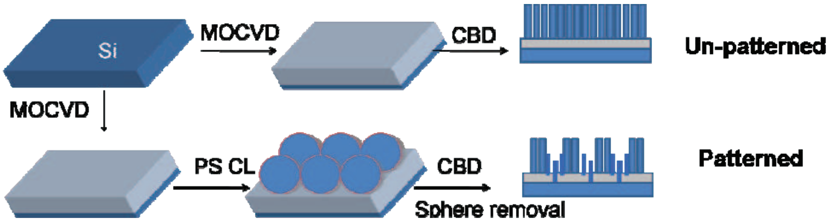

Figure 7.14: Graphical representation of the experimental steps for the MOCVD- CL-CBD synthetical route for ZnO fabrication: (a) unpatterned ZnO, (b) patterned ZnO

Figure 7.15 shows the effective fabrication of patterned ZnO nanostructures using TMEDA (Fig. 7.15 (a)) and EDA (Fig. 7.15 (b)) the colloidal polymeric masks removal. It is well visible that the extension of the pattern vacancies within the template defines different density areas of ZnO nanorods, whose dimensions are strictly connected to the available surface area of the underlying seed layer.

Fig. 7.15 (a,b) reveals the presence of ZnO nanotubes (mean diameter~ 40 ± 20 nm), as the result of a hindered growth process due to the confining effect of PS mask during the CBD growth [52] On the contrary, the external ZnO nanorods (mean diameter ~ 200 nm in case of TMEDA and ~ 100 nm in case of EDA respectively) are characterised by a higher density, better defined geometry and variable length according to the CBD growth parameters [38,53]. Moreover it should be noted that, external rods produced using TMEDA ligand resulted in formation of hexagonal rods with flat tops, while the use of EDA led to the formation of sword-like structures. From the SEM cross section (Fig. 7.15 (b')) an average value of ~ 600 nm (1h of growth) for the ZnO pores depth is measured suggesting that growth rate is enhanced due to spatial confinement.

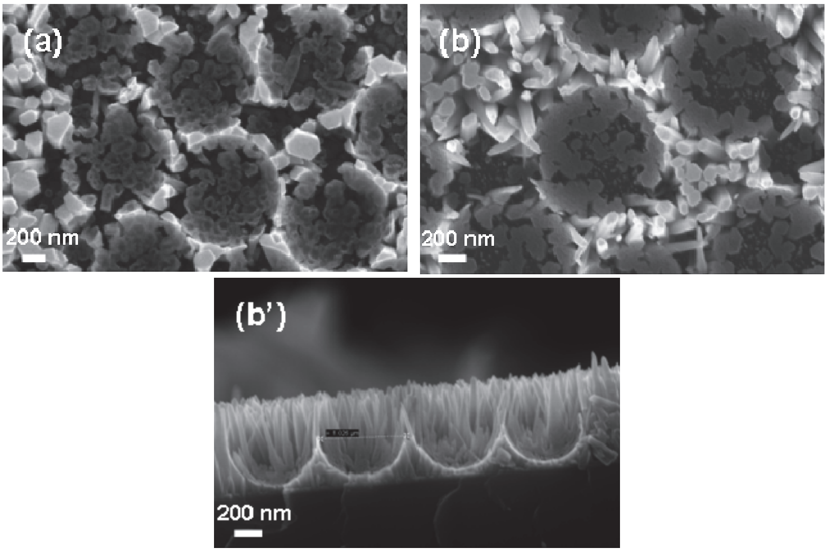

Figure 7.15: SEM plan view of ZnO nanoplatforms produced using TMEDA (a) and EDA ligand (b) and related cross section (b')

XPS analysis has been performed to study the surface composition of the obtained ZnO nanoplatforms (Table 7.2). The comparison between patterned and unpatterned ZnO samples evidences significant differences of surface chemical composition, within the sampling depth at the current analysis conditions. In particular a dramatic decrease of detected zinc signal is found for patterned samples (~ 7% of atomic concentration *vs* the ~ 23% detected for both seed and unpatterned layers), associated to the appearance of the silicon signal from the substrate. This finding is likely related to the porous nature of the ZnO nanotubes confined inside the interior area of the micropore array (see Fig. 7.15 (a)). In addition, solvent driven effects related to colloidal lithography micropatterning and resulting in a partial ZnO dissolution can be invoked [54].

Table 7.2: XPS quantitative analysis of patterned and unpatterned ZnO surfaces

	Zn	C	O	Si
MOCVD	23	35	43	-
Unpatterned	23	40	37	-
Patterned	7	38	43	12

The peak shape analysis of C 1s high-resolution spectra (Figure 7.16 (a)) for the three investigated surfaces, namely MOCVD seed layer, ZnO unpatterned nanorods and ZnO patterned nanotubes-nanorods, evidences a similar distribution of peak components. In particular, the C 1s peak is a convolution of three main different components, corresponding respectively to: (i) C-C and C-H bonds (binding energy (BE) = 284.8 eV), (ii) C-O bonds (BE = 286.5 eV) and, (iii) carbon doubly bonded to oxygen species such as C(=O)O or O-C-O bonds (BE = 288.8 eV) mainly due to surface adsorbed carbonates and hydrogen carbonates [55].

On the other hand, the O 1s high resolution spectra (Fig. 7.16 (b)) clearly evidence two main peak contributions, attributed to bulk Zn-O species (BE= 530.5 eV) and to adsorbed oxygen species (BE = 532.2 eV) respectively [56]. The latter, clearly prevailing in the patterned sample after PS sphere removal, is an indication of a high surface hydroxylation. Therefore, it can be reasonably argued that the patterned ZnO nanoplatforms are characterised by a higher contribution of surface polar moieties than the corresponding unpatterned surfaces. This evidence is explained by the high surface-to-volume ratio of the present nanoplatforms where the dimensionality of the ZnO nanorods is combined to the porous nature of the hemispherical arrays, thus suggesting a peculiar response in terms of protein behaviour at the investigated interfaces.

FRAP experiments have been performed to get more insights about the mobility of proteins adsorbed onto the ZnO investigated surfaces. In this context, albumin has been used as a model biomolecule whose adsorption on solid surfaces is known to be strongly influenced by the polar character of the substrate [57,58].

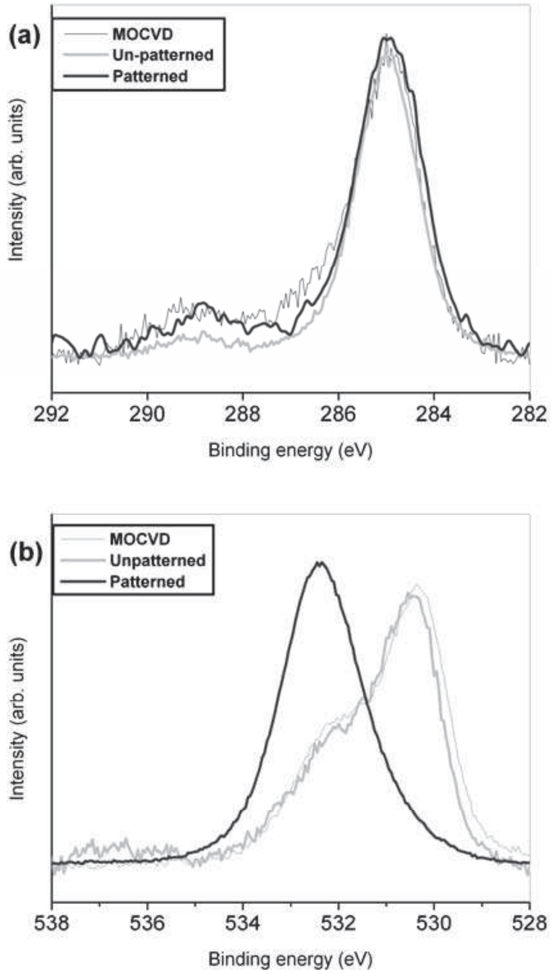

Figure 7.16: XPS peaks of C 1s (a) and O 1s (b) for seed layer (MOCVD, light gray line), ZnO unpatterned (dark gray line) and ZnO patterned (black line)

Some representative fluorescence images for a FRAP experiments for fluoresceine-labeled albumin adsorbed on patterned and unpatterned ZnO are shown in Figure 7.17. The fluorescence recovery, due to lateral diffusion of un-bleached/bleached protein molecules inside/outside the bleached spot, is, thus, related to the protein mobility at the bio-interface between the adsorbed protein layer and the ZnO surface. Only a partial recovery of fluorescence is obtained from both unpatterned and patterned ZnO nanorods.

However, the analysis of the emission intensities, normalized to the pre bleach values (Figure 7.18 (a)) evidences a faster recovery for unpatterned ZnO nanorods than the ZnO nanoplatforms. Moreover, the normalised fluorescence increments for specific emission recovery related to the ZnO nanotubes areas (i.e inside the micropores) is lower than that from the external ZnO nanorod areas (i.e. outside the micropores) (Fig. 7.18 (b)) as to the reported effect of topography on electrostatic and dispersion interactions at the solid-liquid interface [59].

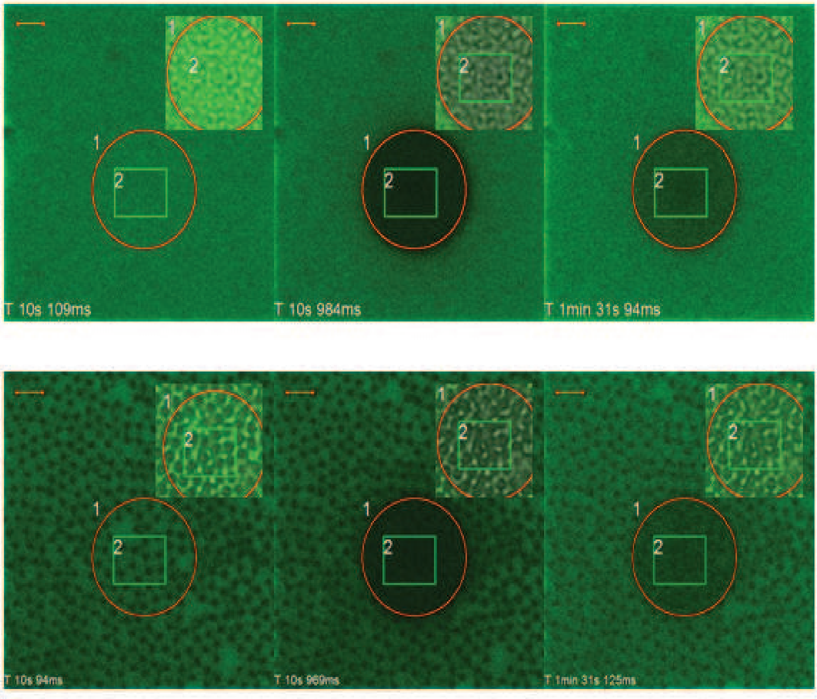

Figure 7.17: Confocal microscopy images (λex= 488 nm, λem= 531 nm) of unpatterned (a) and patterned (b) ZnO samples after FITC-alb adsorption. Images for the montage have been picked up immediately before bleach (left), immediately after (centre) and 80 s after bleach (left). In the insets the merged images of fluorescence and bright field from the bleached area. Scale bar = 2 μm

To summarise, the obtained results point to the effectiveness of chemical and/or topographical patterning of ZnO surfaces as a sensitive and tunable factor to control the response of biological molecules at the interface.

To conclude, a two steps MOCVD-CBD approach is presented as a successful strategy to fabricate c-axis oriented ZnO nanorods. Effects of the ZnO buffer layer, deposited by drop-casting of zinc (II) solution and by MOCVD, on

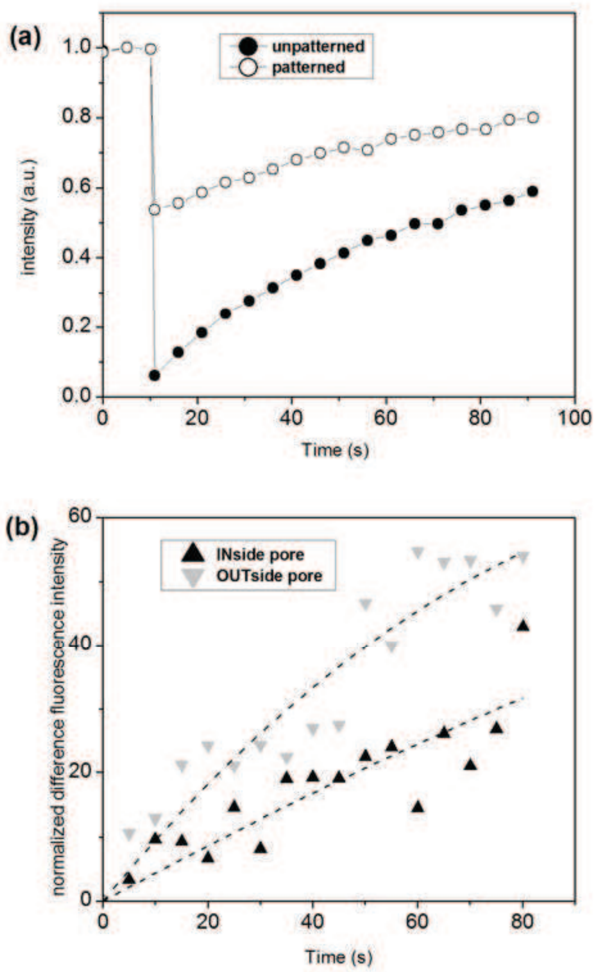

Figure 7.18: (a) Normalised fluorescence intensity over whole FRAP experiments for ZnO unpatterned (solid circles) and patterned (open circles); (b) Normalised fluorescence increments for emission recovery from INside (up triangles) and OUTside (down triangles) ZnO pore areas.

the subsequent CBD growth of ZnO nanorods have been scrutinised. The thickness and structural complexity of the ZnO buffer layer has a great impact on the nanorods growth rate and greater surface roughness slow down the CBD growth. In fact, the ZnO buffer layer acts as a nucleation template for the ZnO nanorods growth and, hence, more complex templates have more ZnO nuclei that favour a higher ZnO nanorods density. Nevertheless the corresponding growth rate appears slowed down due to an overall decrease of the Zn^{2+} and OH^- concentration at the substrate-CBD solution interface.

Moreover, the good crystalline grade of seed layers appears strongly related to the MOCVD deposition temperature and represents an important parameter to improve texturing of ZnO nanorods.

Additionally, the effect of nutrient bath concentration on CBD growth rate has been scrutinised. Lower nutrient bath concentrations are associated with slower ZnO growth rate. Upon increasing the concentration, the CBD process is faster and the global nanorods aspect ratio is increased thus supporting the preferential 1D growth along the c-axis of the ZnO nanostructures. Furthermore, the choice of ligand allows to control the supersaturation of the solution promoting the nucleation and also affects the morphology of the resultant nanostructures.

Moreover, it has been demonstrated that the present approach is effective to grow, even over low quality buffer layers, deposited *via* MOCVD at low (400 °C) process temperature, long and crystalline ZnO nanorods possessing, at room temperature, a strong ultra-violet (UV) photoluminescence edge emission at about 3.28 eV and a weak green contribution. This is evidence of limited defect densities of the obtained ZnO nanostructures.

Finally, nanotube-nanorod hybrid networks have been successfully assembled as dense ZnO micropores arrays by an effective integration of MOCVD-CL-CBD processes. The intrinsic porosity inferred by topographical patterning affects, in turn, the surface chemical structure, as measured in terms of surface polar moieties. Proof of working measurements of protein lateral diffusion after adsorption onto the ZnO nanoplatforms evidence the reduced biomolecule mobility inside the hemispherical micropores, explained by their intrinsic porous nature and related polarity. To conclude the present ZnO nanoplatforms have a great potential for biosensing application as their interaction with biomolecules of interest can be easily triggered by proper tuning of the system dimensionality.

References

1. S. Xu and Z.L. Wang, Nano Res. 4 (2011) 1013-1098.
2. S. Baruah and J. Dutta, Sci. Technol. Adv. Mater. 10 (2009) 013001.
3. B. Weintraub, Z. Zhou, Y.Li, Y Deng, Nanoscale 2 (2010) 1573-1587.
4. K. Govender, D.S. Boyle, P.B. Kenway, P. O'Brien, J. Mater. Chem. 14 (2004) 2575-2591.

5. H. Zhang, J. Feng, J. Wang, M. Zhang, Mater. Lett. 61 (2007) 5202-5205.
6. X. Hu, Y. Masuda, T. Ohji, K. Kato, J. Am. Ceram. Soc. 92 (2009) 922-926.
7. L. Vayssieres, K. Keis, S.-E. Lindquist, and A. Hagfeldt, J. Phys. Chem. B 105 (2001) 3350-3352.
8. M. Guo, P. Diao, S. Cai, Appl. Surf. Sci. 249 (2005) 71-75.
9. L.E. Greene, M. Law, J. Goldberger, F. Kim, J. C. Johnson, Y. Zhang, R. J. Saykally and P. Yang, Angew. Chem., Int. Ed. 42 (2003) 3031-3034.
10. Z.R. Tian, J.A. Voigt, J. Liu, B. Mckenzie, M. J. Mcdermott, M. A. Rodriguez, H. Konishi and H. Xu, Nat. Mater. 2 (2003) 821-826.
11. S.-C. Liou, C.-S. Hsiao, S.-Y. Chen, J. Cryst. Growth 274 (2004) 438-446.
12. M. Willander, L.L. Yang, A. Wadeasa, S.U. Ali, M.H. Asif, Q.X. Zhao and O. Nur, J. Mater. Chem. 19 (2009) 1006–1018.
13. T. Ma, M. Guo, M. Zhang, Y. Zhang and X.Wang, Nanotechnology 18 (2007) 035605.
14. L.E. Greene, M. Law, D.H. Tan, M. Montano, J. Goldberger, G. Somorjai, and P. Yang, Nano Lett. 5 (2005) 1231-1236.
15. D. Byrne, E. McGlynn, M.O. Henry, K. Kumar, G. Hughes, Thin Solid Films 518 (2010) 4489-4492.
16. G. Kenanakis, D. Vernardou, E. Koudoumas, N. Katsarakis, J. Cryst. Growth 311 (2009) 4799-4804.
17. S.-H Hu, Y.-C. Chen, C.-C. Hwang, C.-H. Peng, D.-C. Gong, J. Alloys Compd. 500 (2010) L17-L21.
18. C.-C. Ting, C.-H. Li, C.-Y. Kuo, C.-C. Hsu, H.-C. Wang, M.-H. Yang, Thin Solid Films 518 (2010) 4156-4162.
19. Y. Tao, M. Fu, A. Zhao, D. He, Y. Wang, J. Alloys Compd. 489 (2010) 99-102.
20. T. Hamada, A. Ito, E. Fujii, D. Chu, K. Kato, Y. Masuda, J. Cryst. Growth 311 (2009) 3687-3691.
21. C.M. Shin, J.Y. Lee, J.H. Heo, J.H. Park, C.R. Kim, H. Ryu, J.H. Chang, C.S. Son, W.J. Lee, S.T. Tan, J.L. Zhao, X.W. Sun, Appl. Surf. Sci. 255 (2009) 8501-8505.
22. X. Q. Zhao, C.R. Kim, J.Y. Lee, J.H. Heo, C.M. Shin, H.Ryu, J.H. Chang, H.C. Lee, C.S. Son, W.J. Lee, W.G. Jung, S.T. Tan, J.L. Zhao, X.W. Sun, Appl. Surf. Sci. 255 (2009) 4461-4465.

23. D.-F. Zhang, L.-D. Sun, J. Zhang, Z.-G. Yan, and C.-H. Yan, Cryst. Growth Des. 8 (2008) 3609-3615.
24. S.-M. Yang, S.G. Jang, D.-G. Choi, S. Kim, H.K. Yu, Small 2 (2006) 458-475.
25. A. Dorfman, N. Kumar, J.I. Hahm, Langmuir 22 (2006) 4890-4895.
26. M.E.Fragalà, C. Satriano J. Nanosci. Nanotechn. 10 (2010) 5889-5893.
27. W.-Y. Wu, C.-C. Yeh, J.-M. Ting, J. Am. Ceram. Soc. 92 (2009) 2718-2723.
28. J. Song, S. Lim, J. Phys. Chem. C 111 (2007) 596-600.
29. W. Wu, G. Hu, S. Cui, Y. Zhou, H. Wu, Cryst. Growth Des. 8 (2008) 4014-4020.
30. G. Malandrino, M. Blandino, M.E. Fragalà, M. Losurdo, G. Bruno, J. Phys. Chem. C 112 (2008) 9595-9599.
31. Y.-C. Lee, S.-Y. Hu, W. Water, K.-K. Tiong, Z.-C. Feng, Y.-T. Chen, J.-C. Huang, J.-W. Lee, C.-C. Huang, J.-L. Shen, M.-H. Cheng, J. Lumin. 129 (2009) 148-152.
32. L.L. Yang, Q.X. Zhao, M. Willander, J. Alloys Compd. 469 (2009) 623-629.
33. S.-H. Yi, S.-K. Choi, J.-M. Jang, J.-A Kim, W.-Gwang, J. Colloid Interface Sci. 313 (2007) 705-710.
34. J. Zhao, Z.-G. Jin, T. Li, X.-X. Liu, J. Eur. Ceram. Soc. 26 (2006) 2769-2775.
35. R.S. Kumara, P. Sudhagarb, R. Sathyamoorthya, P. Matheswarana, Y.S. Kang, Superlattices Microstruct. 46 (2009) 917-924.
36. G. Malandrino, M. Blandino, L.M.S. Perdicaro, I.L. Fragalà, P. Rossi, P. Dapporto, Inorg. Chem. 44 (2005) 9684-9689.
37. X. Gao, X. Li, W. Yu, J. Phys. Chem. B 109 (2005) 1155-1161.
38. M.E. Fragalà, Y. Aleeva, G. Malandrino, Superlattices Microstruct. 48 (2010) 408-415.
39. Q. Li, J. Bian, J. Sun, J. Wang, Y. Luo, K. Sun, D. Yu, Appl. Surf. Sci. 256 (2010) 1698-1702.
40. M. Kostoglou, N. Andritsos, A.J. Karabelas, Ind. Eng. Chem. Res. 39 (2000) 3272-3283.
41. Y. Masuda, K. Kato, Cryst. Growth Des. 9 (2009) 3083-3088.
42. X. Liu, Z. Jin, S. Bu, J. Zhao, Z. Liu, Mater. Lett. 59 (2005) 3994-3999.

43. M. Ortega-López, A. Avila-García, M.L. Albor-Aguilera, V.M. Sánchez Resendiz, Mater. Res. Bull. 38 (2003) 1241-1248.
44. Z. Yang, Y.-Y. Shi, X.-L. Sun, H.-T. Cao, H.-M. Lu, X.-D. Liu, Mater. Res. Bull. 45 (2010) 474_480.
45. Q. Li,V. Kumar,Y. Li,H. Zhang,T. J. Marks,R. P. H. Chang, Chem. Mater. 17, (2005) 1001-1006.
46. A.B. Djurišic, Y.H. Leung, Small 2 (2006) 944-961
47. P. Jiang, J.J. Zhou, H.F. Fang, C.Y. Wang, Z.L. Wang, S.S. Xie, Adv. Funct. Mater. 17 (2007) 1303-1310.
48. R.A. Laudise, A.A. Ballman, J. Phys. Chem. 64 (1960) 688-691.
49. W.-J. Li, E.-W. Shi, W.-Z. Zhong, Z.-W. Yin, J. Cryst. Growth 203 (1999) 186-196.
50. B.D. Yao, H.Z. Shi, H.J. Bi, L.D. Zhang, J. Phys. Condens. Mater. 12 (2000) 6265-6270.
51. K. Vanheusden, W.L. Warren, C.H. Seager, D.R. Tallant, J.A. Voigt, B.E. Gnade, J.Appl. Phys. 79 (1996) 7983-7990.
52. Y. B. Pyun, J. Yi, D. H. Lee, K. S. Son, G. Liu, D.K. Yi, U. Paikac, W. I. Park, J. Mater. Chem.20 (2010) 5136-5140.
53. [M.E. Fragalà, Y.Aleeva, G.Malandrino, Thin Solid Films 519 (2011) 7694-7701.
54. H.Q. Wang, G.H. Li, L.C. Jia, G.Z. Wang, C.J. Tang, J. Phys. Chem. C 112 (2008) 11738-11743.
55. K.G. Saw, K. Ibrahim , Y.T. Lim, M.K. Chai, Thin Solid Films, 515 (2007) 2879-2884.
56. J.-C. Dupin, D.Gonbeau, P. Vinatierb, A. Levasseurb, Phys. Chem. Chem. Phys. 2 (2000) 1319-1324.
57. Auditore, C. Satriano, U. Coscia, G. Ambrosone, V. Parisi, G. Marletta, Biomol. Eng. 19 (2002) 85-90.
58. G.M.L. Messina, C. Satriano, G.Marletta Colloids Surf., B 70 (2009) 76-83.
59. P. Elter, R. Lange, and U. Beck, Langmuir 27 (2011) 8767-8775.

8. Fabrication of hierarchical core-shell TiO_2-ZnO nanostructures

Introduction

The use of gas and biological sensors represents an emerging market resulting from strategies for intelligent process management, environmental protection and medicinal diagnostics as well as from the domestic, aerospace and automobile sectors. Hence, the development of fast responding, sensitive and especially highly selective gas sensor materials is of major interest.

It is worth noting that the sensitivity of chemical gas sensors is strongly affected by the specific surface of sensing materials. A higher specific surface of a sensing material leads to a higher sensor sensitivity, therefore many techniques have been adopted to increase the specific surface of sensing films with fine structures, especially to form the nanostructures, taking advantage of the large specific surface of nanostructured materials. In particular, recently, heterostructured one-dimensional (1D) nanomaterials have been extensively studied due to their synergetic properties, surface modification, large interfacial area which may give them more versatile functions than nanomaterials that can be used effectively for nanoscale devices. Hierarchical hetero-nanostructures find applications in a variety of fields such as field emission photovoltaics, supercapacitors, photocatalysts, sensors and multifunctional nanocomposites that require high surface areas [1-7].

Core-shell nanomaterials, a type of heterostructured nanomaterial, are currently widely used in the areas of catalysis, drug delivery and sensors, etc [8-10]. In this perspective, it is becoming important to develop new methods of synthesizing a wide variety of core-shell nanomaterials in order to enhance the properties of nanomaterials and therefore device performance significantly. Synthetic routes suited for enhancing robustness and controlling sizes, shapes, and compositions have therefore received increasing attention in recent years. In this scenario, metal oxide semiconductors having dual or multiple morphologies and structures become of interest since they represent a versatile solution for performance enhancement and applications in multifunctional devices [11].

Among semiconductor oxides, oxide-based titania (TiO_2), a native oxygen-deficient metal oxide, with a bandgap of 3.2 eV (anatase) has been undoubtedly proved to be an economically moderate dopant and potential sensing material.

TiO_2 has four major polymorphs: rutile (tetragonal), anatase (tetragonal), brookite (orthorhombic), and TiO_2 (B) (monoclinic). The lattice structure difference of these polymorphs leads to many different physical and physicochemical properties and thus results in different performances in applications. For instance, the band gaps for bulk rutile and anatase are 3.0 and 3.2 eV, respectively. Anatase exhibits higher electron mobility than rutile, which makes it more suitable for the application in solar cells.

Rutile and anatase are the two most important crystal polymorphs of TiO_2, which can be attributed to their relatively higher stability and easier synthesis.

It has been widely demonstrated that the functional properties of the TiO_2 material depend on not only its morphology but also its crystalline structures. It has been found that TiO_2 as an additive could greatly improve the gas-sensing properties of sensors based on SnO_2, WO_3, ZnO, Ba_2O_3, etc. The search for an improved semiconductor-based sensor has expanded into new metal-oxide systems. It has to be reminded that the gas-sensing mechanism of metal oxide materials is based on the reaction between the adsorbed oxygen on the surface of the materials and the gas molecules to be detected. The state and the amount of oxygen on the surface of materials are strongly dependent on the microstructure of the materials, such as specific area, particle size, as well as the film thickness of the sensing film. In order to obtain gas sensors with good performance, the research is actually devoted to nanomaterials because they have high specific area and contain more grain boundaries. The response of semiconductor oxide gas sensor to the presence of a given gas depends on the speed of the chemical reaction on the surface and the speed of diffusion of the gas molecules to that surface which are activation processes, and the activation energy of the chemical reaction is higher.

Great attention has been recently devoted to the fabrication of nanocomposites containing ZnO and TiO_2 [12-15]. ZnO–TiO_2 system materials were first used in the chemical industry as catalysts and color pigments, whereas zinc titanates are good dielectric materials for microwave devices [16]. ZnO-TiO_2 system materials are also reported for H_2S, toluene and ethanol sensing [17].

In fact, implementation of TiO_2 materials with ZnO has often proved to improve the photocatalytic properties of TiO_2 [12,18] and to promote some anatase-to-rutile phase transition [19].

The phase transformation process from anatase to rutile has been widely studied for both scientific and application-driven reasons because the TiO_2 phase is one of the critical factors for many applications. In the calcination process, the transformation from anatase to rutile took place above 600 °C.

Actually, the co-existence of the two phases due to the presence of dopant hetero-atoms [19-21] appears particularly promising since it modifies the spatial charge separation and reduces the recombination efficiency, hence improving the photocatalytic performances [22]. In fact, under illumination of the mixed phase TiO_2, an electron is promoted into the lower energy rutile conduction band and this photogenerated electron is transferred sequentially into trapping sites in the rutile lattice, the anatase lattice the interface between the rutile and anatase and the surface, and this reduces the recombination rate of e^- and h^+ and increases the synergistic effect between the anatase and rutile TiO_2 system.

In addition, ZnO hierarchical nanostructures are excellent sensors (i.e. gas, humidity, UV) due to the enhanced surface interactions depending on a more favorable surface to volume ratio than ZnO bulk and continuous nanostructured films [23-27].

Many methods have been adopted to fabricate ZnO/TiO_2 nanocomposite films and nanostructures [28]. Among them a combination of electrospinning and hydrothermal method approach to synthesize ZnO/TiO_2 hierarchical nanostructures has been recently proposed [29].

Nowadays, electrospinning represents an important edge over other larger-scale nanofibers production methods. It allows the fabrication of nanofibers from synthetic or natural polymers in a controlled manner with dimensions down to a few nanometers, and functionalized by the addition of drugs, or of semiconductor or catalyst nanoparticles. They can be employed in numerous applications with great benefit. In fact, it allows customization of nanofiber assemblies to meet the requirement of specific applications and an performance enhancement. Electrospinning, in fact, represents an important edge over other larger-scale nanofibers production methods [30]. It allows customization of nanofiber assemblies to meet requirements for specific application and performance enhancement.

Nanofibers fabricated via electrospinning have specific surface approximately one to two orders of the magnitude larger than flat films, making them excellent candidates for potential applications in sensors. Therefore, electrospun nanofibers have been recently used as nanoplatforms for gas sensors and several approaches have been adopted for functional activation of their surfaces [28-31]. Therefore, any effort to enhance the working surface area of the multifunctional devices can successfully take advantages of three-dimensional (3-D) nanostructured materials and hierarchical single crystal branches of smaller size represent an effective approach for surface activation.

In this context, in this chapter we report on the successful fabrication and full characterization of Zn doped TiO_2 electrospun nanofibers (herein d:TiO_2) shelled *via* MOCVD deposition with hierarchical ZnO nanostructures. The present approach combines the flexibility of electrospinning to large-scale production of ceramic nanofibers [32] with all the MOCVD benefits associated with high reproducibility, easily controlled growth (largely proven on large scale), short process times, quality grade crystallinity and elemental purity. Presently, this strategy has been successfully tested for the reproducible fabrication of standing alone doped TiO_2 (herein named as d: TiO_2) as well as for d:TiO_2 nanofibers shelled with ZnO hierarchical nanostructures (herein d:TiO_2-ZnO). The particularly favorable surface-to-volume ratio, due in turn to the large density of ZnO single crystalline nanorods/nanoneedles on the shell surface, promotes a remarkable cathodoluminescence emission in the UV and green regions. The obtained nanoarchitectures result quite complex and therefore a careful characterization of the Zn doped TiO_2 core, before and after the ZnO external shell deposition, is also presented.

Main aim of this research field was: i) to find a simple strategy to prepare core-shell TiO_2-ZnO nanofibers; ii) to identify the issues that affect the nanofiber characteristics in terms of structural and compositional properties. In addition, the effect of Zn doping of the TiO_2 core has been investigated both in regard to the ZnO shell growth as well as to study the effect on the anatase to rutile transition and $ZnTiO_3$ formation.

Results and discussion

Uniform one-dimensional (1D) inorganic–organometallic hybrid nanofibers have been fabricated by electrospinning from alcoholic solutions of polyvinylpyrrolidone (PVP) and suitable alcoholic precursors of titanium (IV) and zinc(II) ions, namely Titanium tetraisopropoxide and Zn(tta)2·tmeda (Htta = 2-thenoyl-trifluoroacetone, tmeda=N,N,N',N'-tetramethylethylendiamine) [32]. The relative atomic concentration of the Zn metal-organic precursor has been varied from 3% to 15%.

Electrospun Zn doped TiO_2/PVP nanofibers have been calcined in air at 500 °C for 3 hours to completely remove the polymeric component as well as to promote the complete decomposition of Zn (II) metal-organic precursor inside the nanofibers.

Figure 8.1 shows the SEM image of d:TiO_2 nanofibers, deposited on Si substrate and calcined at 500 °C. It is clear that electrospun annealed material consists of randomly oriented fibres with average diameter of 50 ± 30 nm. Large interconnected voids are present among the fibres, thus resulting in a 3D porous network.

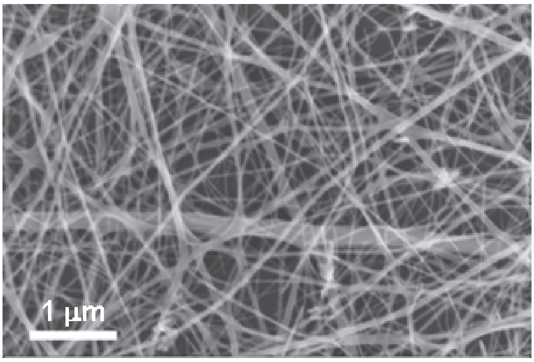

Fig. 8.1: SEM image of the d:TiO_2 (Zn 3%) electrospun nanofibers

The related EDX analyses point to the presence of Zn heteroatoms with a TiO_2/Zn composition in the nanofibers well in agreement with nominal values (Table 8.1).

Table 8.1: EDX analyses of the d:TiO_2 nanofibers

Nominal Zn/Ti%	Zn/Ti at%
3%	3.1
5%	5.4
15%	14.8

The bright field TEM image (Fig. 8.2 (a)) confirms the presence of polycrystalline nanofibers having different size ranging from 20 to 100 nm. The EF-TEM maps provide evidence of a homogeneous chemical distribution of both Ti and Zn ions (Fig. 8.2 (b) and (c)) in agreement with the presence of well distributed Zn dopant without aggregation of ZnO grains.

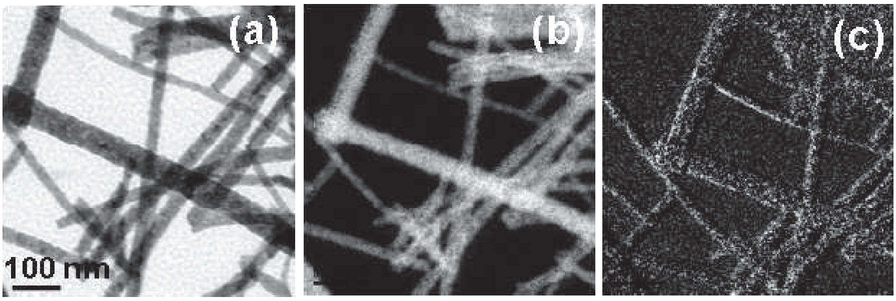

Figure 8.2: Bright field TEM image of the d:TiO_2 (Zn 15%) nanofibers (a); Energy Filtered TEM maps of Ti (b) and Zn (c)

These findings match well XRD data of d:TiO_2 nanofibers (Fig. 8.3). In fact, the obtained patterns show the sequence of broad peaks expected for the pure anatase TiO_2 phase (JCPDS #21-1272) without any evidence of spectral features that might be related to ZnO.

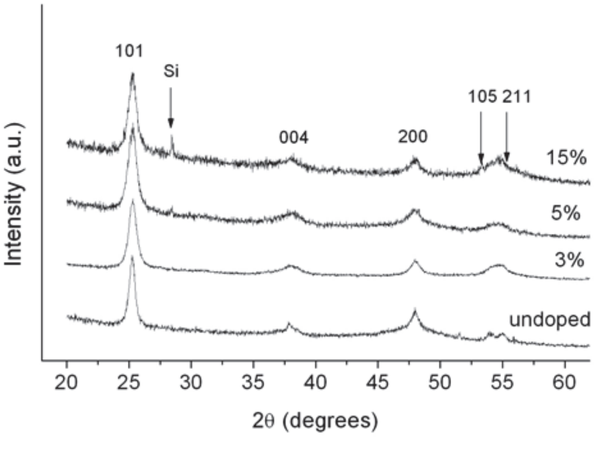

Figure 8.3: XRD patterns of calcined (500 °C, 3 h) undoped TiO_2 and Zn doped TiO_2 electrospun nanofibers

One of the most important issues regarding Zn doping is related to the position of Zn within the TiO_2 structure. Zn^{2+} ion has an ionic radius value (0.74 Å) that is not very different than that of Ti^{4+} (0.68 Å), thus Zn could substitute Ti without producing any important difference in the position of anatase phase peaks in the XRD pattern. This is actually confirmed from Fig. 8.3, which shows the same anatse peak positions for undoped and doped samples, even for the highest dopant concentration (15%). All discussed points to the lack of any crystalline ZnO precipitate inside the TiO_2 nanofibers, even after calcination at 500°C in air.

The XPS survey spectra (Fig. 8.4 (a)) of calcined d:TiO_2 nanofibers show, in addition to Ti, O and C features observed in the undoped reference, the Zn core level peaks. The undoped nanofibers present the Ti 2p doublet (Fig. 8.4 (b)) in the 458.9 – 464.6 eV range, with the spin orbit splitting (5.7 eV) in good agreement with the Ti^{4+} oxidation state [33]. Upon increasing the Zn content in the nanofibers, this feature slightly moves towards lower binding energy [34]. Even more significant modifications are observed in the case of the O 1s peak (Fig. 8.4 (c)). The undoped TiO_2 reference shows an asymmetrical and well discernible broadening toward higher binding energy values that highlights two rather resolved components centered at 530.3 eV and at 532.2 eV, respectively. Literature data suggest that the former component represents the Ti-O bonds while the latter component can be related to hydroxyl groups (OH^-) over the nanofiber surface [35,36]. Upon increasing the Zn content in the nanofibers the relative intensity of the latter feature increases thus pointing to a higher surface hydroxylation [18].

Finally, the Zn 2p region (Fig. 8.4 (a)) shows the expected Zn $2p_{3/2,1/2}$ doublet at 1022.0 eV and 1045.0 eV, respectively. The inferred spin orbit splitting (23 eV) is indicative of a Zn^{2+} ion. Chemical shifts associated with Zn containing compounds are normally spread in a narrow range and therefore, poorly suited for identification of the oxidation state. Nevertheless, the Auger parameter (α) is indicative of chemical state. In the present case, the measured Auger parameter (α = 2010 eV) can be associated with Zn^{2+} on the surface of TiO_2 based nanofibers [37]. It, therefore, transpires that calcination at 500 °C causes an exhaustive decomposition of the Zn precursor.

Table 8.2 collects the Auger parameters and atomic compositional data of calcined d:TiO_2 nanofibers. Analytical data have been evaluated from XPS peak

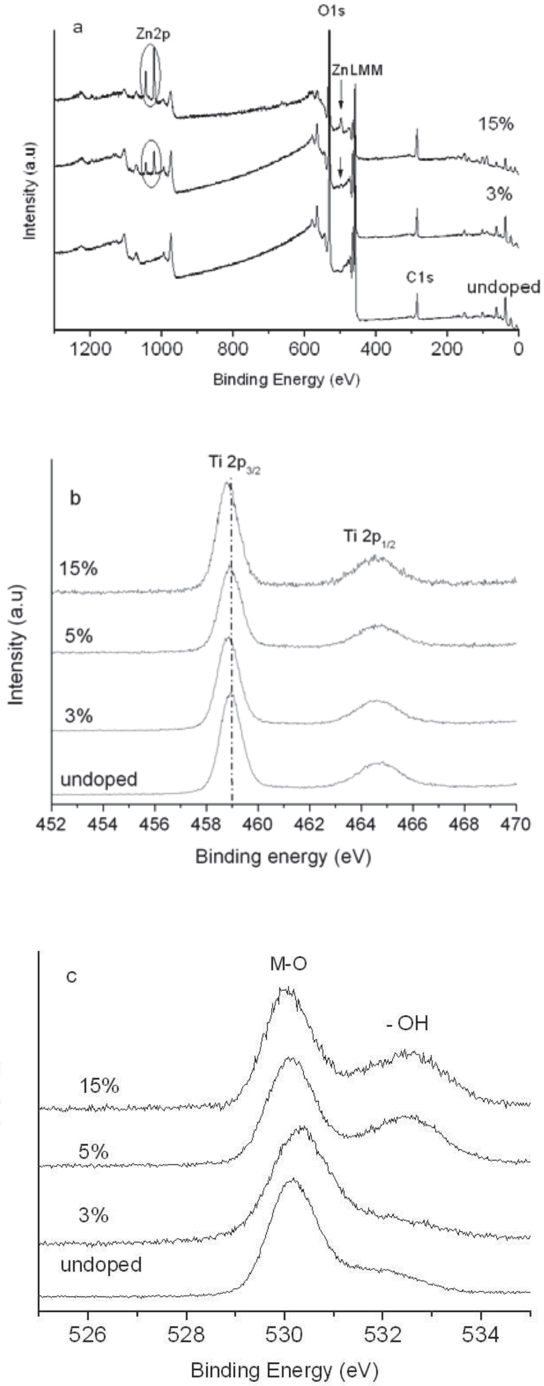

Figure 8.4: XPS surveys of calcined undoped TiO_2 and Zn doped TiO_2 electrospun nanofibers (a); high resolution XPS spectra of Ti 2p (b) and O 1s (c) regions of calcined undoped TiO_2 and Zn doped TiO_2 nanofibers.

areas, corrected for their relative sensitivity factors. It becomes evident that the Zn doping levels obtained from XPS are lower than the nominal values (the latter confirmed by the EDX data, as shown in Table 8.1). Note that XPS results refer to the surface composition and provide an indication of Zn surface segregation inside the TiO_2 nanofibers, while the EDX data relate to the bulk composition. The C content is mainly related to surface contamination that results particularly significant due to the large surface to volume ratio of the present system. In order to avoid any kind of fiber damaging, no sputtering has been performed before XPS analysis. For the sake of completeness, the C content associated with uncomplete precursor decomposition of as spun nanofibers (not shown) is about 60%.

Table 8.2: XPS atomic compositional data of d:TiO_2 nanofibers and Zn Auger parameters

Nominal Zn %	Zn %	Ti %	O %	C %[a]	Zn α parameter (eV)
3	2	20	58	20	2010.1
5	3	20	57	20	2010.3
15	8	16	55	21	2010.2

[*] The XPS spectra were recorded without any sputtering process, thus the C content arises from surface carbon contamination.

Present d:TiO_2 nanofibers have been used as template (thus benefitting of their flexibility, self standing properties and high surface-to-volume ratio) to produce core-shell hierarchical d:TiO_2- ZnO nanoarchitectures *via* MOCVD.

In this perspective, undoped and the d:TiO_2 (Zn 5%) nanofibers have been annealed at 600°C under reduced pressure O_2-Ar atmosphere. XRD studies have given insights on the role played by the dopant on the anatase-to-rutile transition. In Figure 8.5, the XRD diffraction pattern of undoped TiO_2 nanofibers is compared with that of the d:TiO_2 (Zn 5%) sample. The presence of the rutile most abundant peak at $2\theta = 27.48^\circ$ (JCPDS #73-1765) in the d:TiO_2 pattern indicates that Zn doping induces the anatase to rutile transition already at 600 °C. This finding is in accordance with data previously reported which discuss that aliovalent dopants have an important effect on the formation of defect microstructures and metastable phases in titanium dioxide [19,20]. Therefore, the ZnO external shell growth will take place on a two phase anatase-rutile composite nanofibers.

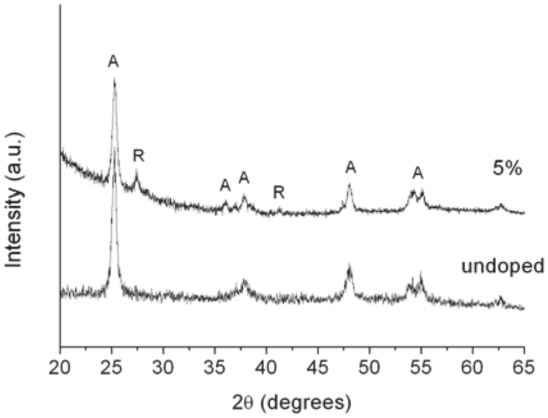

Figure 8.5: XRD patterns of annealed (600°C, 1 h, O_2/Ar) TiO_2 and Zn doped TiO_2 nanofibers

The calcined electrospun d:TiO_2 nanofibers represent suited nanoplatforms for fabrication of hierarchical ZnO nanostructures via MOCVD. The ZnO shell nanostructures have been deposited at 600 °C for 60 min on undoped and d:TiO_2 nanofibers. SEM micrographs (Fig. 8.6 (a-d)) provide evidence of surface hierarchical ZnO nanostructures. Decoration over the nanofibers generally consists of nanograins or shorter nanorods.

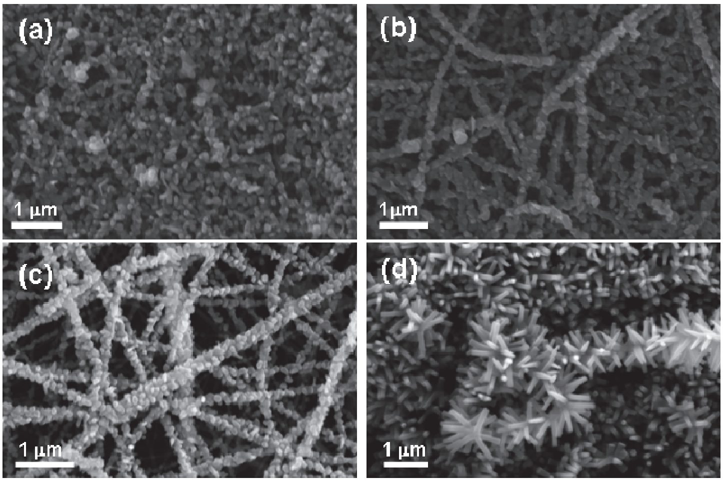

Figure 8.6: SEM images of core-shell TiO_2-ZnO nanofibers (a); d:TiO_2-ZnO nanofibers (Zn 3%) (b); d:TiO_2-ZnO (Zn 5 %) nanofibers (c); d:TiO_2-ZnO nanofibers (Zn 15%) (d). The decorating ZnO shell is deposited by MOCVD at 600°C for 60 min

The XRD patterns (Fig. 8.7) of the d:TiO_2-ZnO core-shell nanofibers provide evidence of formation of polycrystalline ZnO (JCPDS # 36-1451) and, of the anatase to rutile transition promoted by ZnO doping level [18,38]. In addition, interaction of ZnO shell and TiO_2 core gives rise to a sizeable formation of a mixed ZnO-TiO_2 phase (Ecandrewsite JCPDS # 26-1500) and of Zn_2TiO_4 (JCPDS # 25-1164).

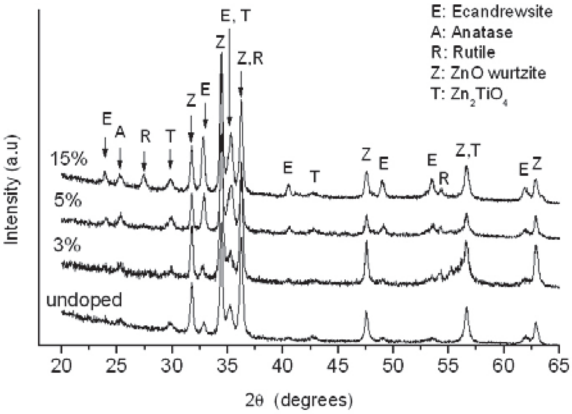

Figure 8.7: XRD patterns of the d:TiO_2-ZnO nanofibers

Longer deposition times (90 vs. 60 minutes) cause the growth of thin and longer nanoneedles (Fig. 8.8).

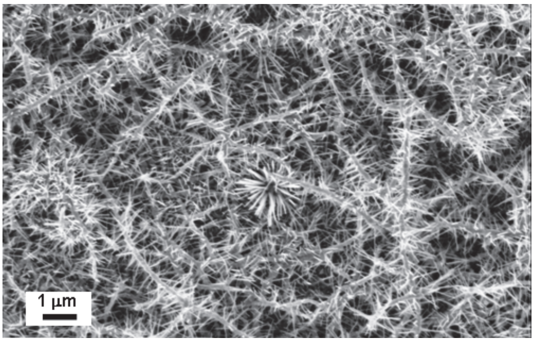

Figure 8.8: SEM images of d:TiO_2-ZnO (Zn 3%) nanofibers. The decorating ZnO shell is deposited by MOCVD at 600°C for 90 min

Both nature and architecture of such nanofibers have been proved by TEM investigation (Fig. 8.9). Contrast evaluation indicates that core nanofibers are certainly polycrystalline in accordance with XRD data with a mean 20 - 30 nm grain size. Hierarchical ZnO nanoneedles are by contrast monocrystalline with tip dimension ranging from 8 to 20 nm. The chemical oxygen map shows a homogeneous intensity distribution. By contrast, the Ti and Zn maps provide clear evidence that the Ti atom is present only on the main body while Zn is distributed on the main nanofiber and the external nanoneedles. It must be noted that the Zn L edge associated with the central nanofiber can be due to both the MOCVD ZnO decoration as well as to the Zn doping of the TiO_2 nanofibers.

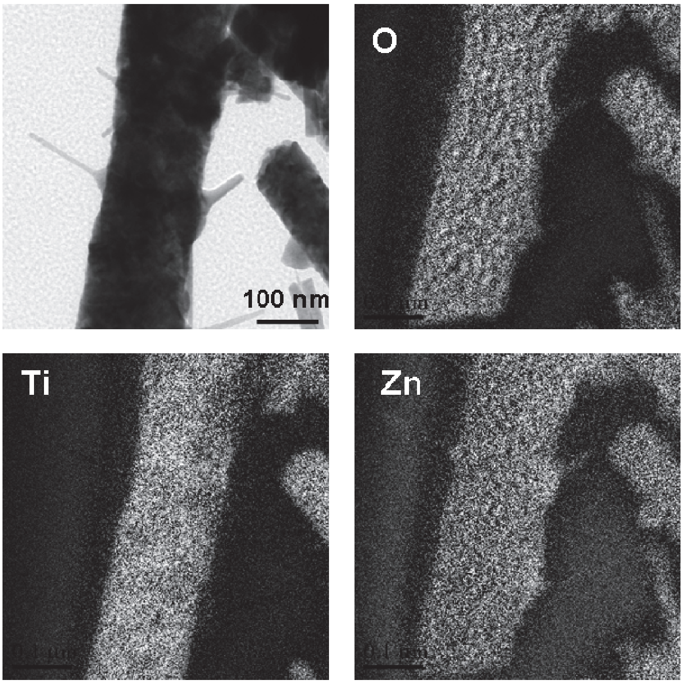

Figure 8.9: Bright field TEM image of core-shell d:TiO_2-ZnO (Zn 3%) nanofibers. The decorating ZnO shell is deposited by MOCVD at 600 °C for 90 min (a); Energy Filtered TEM maps for O, Ti and Zn. Bar is 100 nm

Further insights on the MOCVD deposited ZnO nanoneedles have been obtained by high resolution TEM imaging (Fig. 8.10). The HR-TEM image points to the formation of ZnO single crystal nanoneedles, while the reduced Fast Fourier Transform (FFT) image (inset of Fig. 8.10) shows that the lattice spacing (5.16 Å) along the *c*-axis indicates the [0001] as the direction growth of ZnO nanoneedles.

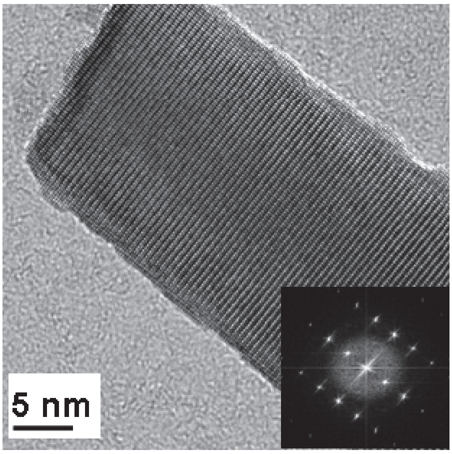

Figure 8.10: High Resolution TEM image of core-shell d:TiO_2-ZnO (Zn 3%) nanofibers and the corresponding reduced FFT image (inset)

Optical properties of the present nanostructures have been also studied by cathodoluminescence. Spectra of the TiO_2 and d:TiO_2 nanofibers, before and after ZnO MOCVD decoration, are reproduced in Figure 8.11. Before ZnO shell deposition, the spectra of the TiO_2 and of d:TiO_2 nanofibers are characterised by the green broad emission band, centered around 550 nm, that relates to surface defects of TiO_2 [39]. This band shifts to 500 nm in the core-shell d:TiO_2-ZnO nanofibers mainly due to ZnO surface intrinsic defects [40,41].

Different mechanisms have been proposed to explain the origin of the ZnO green emission band. In particular, a strong correlation between the green emission, the free-carriers concentration and the density of singly ionized vacancies in commercial ZnO phosphor powders has been often highlighted [42-45]. The green emission in ZnO phosphors is thus resulting from recombination of one electron in singly occupied oxygen vacancies with photoexcited holes in the valence band [46]. Moreover, the cathodoluminescence experiments on core-shell d:TiO_2-ZnO provide evidence of a relatively sharp ultraviolet (UV) emission peak centred at 383 nm, corresponding to the near band edge (NBE) emission of ZnO crystal. This band can be attributed to the recombination of free excitons [47]. It is known that the band edge emission of semiconductors strongly depends on the quality of the crystal. In the present case, this ultraviolet band is present in the spectrum of core-shell d:TiO_2-ZnO hierarchical nanofibers, where the presence of monocrystalline ZnO nanoneedles has been unambiguously confirmed by TEM analysis (Fig. 8.10). The intensity of the UV emission is strongly influenced by the material crystallinity, by the correspondent decrease of impurities and structural defects, as well as by the diameter of emitting nanowires [43, 48-51]. It therefore transpires that the present green emission band intensity observed in the core-shell d:TiO_2-ZnO hierarchical nanofibers, can be correlated to the high surface-to-volume ratio and to the related existence of large quantities of oxygen vacancies within the shelled layers.

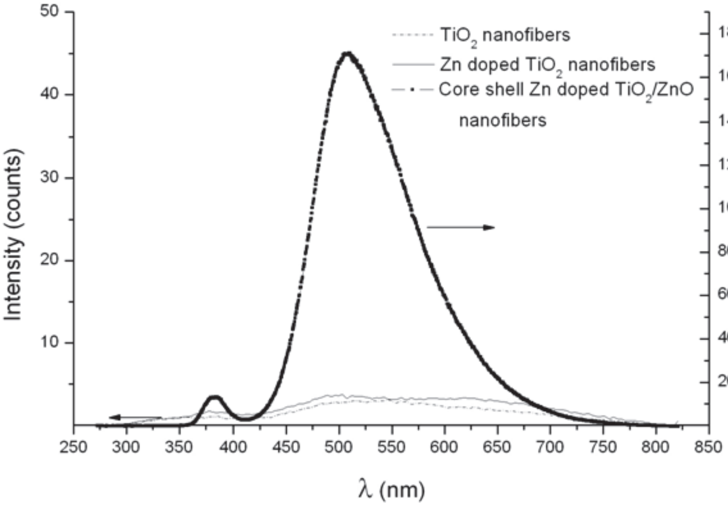

Figure 8.11: Cathodoluminescence spectra of TiO_2 and d:TiO_2 (Zn 3%) electrospun nanofibers compared with the spectrum of core-shell d:TiO_2-ZnO (Zn 3%) nanofibers, obtained by depositing the ZnO external shell by MOCVD at 600°C/90 min

To conclude, Zn doped TiO_2 (d:TiO_2) electrospun nanofibers have been used as template platforms to grow, *via* a MOCVD route, hierarchical ZnO nanoneedles/nanorods. Integration between electrospinnng and MOCVD process has proven a successful new approach to fabricate heterostructures of highly crystalline ZnO nanostructures and d:TiO_2 anatase/rutile nanofibers. It benefits of all the advantages of a robust, well reproducible and easily scalable deposition process. Moreover, the appropriate choice of MOCVD operating conditions allows tailoring of the crystalline and morphological structure of the composite nanofibers, thus promoting the anatase to rutile TiO_2 transition and/or controlling the morphology of the external shells.

The nanostructured d:TiO_2-ZnO nanofibers have an hydroxyl rich surface and show intense emissions in the UV-VIS regions, thus representing a potentially appealing system for a wide variety of technological fields such as photocatalysts, sensing and optical devices. Work is in progress to extend the electrospinning/MOCVD process integration in the perspective of a suited control of process parameters *vs* sensing abilities of these d:TiO_2-ZnO core-shell nanofibers.

References

1. Z.L. Wang, Mater. Sci. Eng., R 64 (2009) 33–71.
2. Z.Z. Ye, F. Yang, Y.F. Lu, M.J. Zhi, H.P. Tang and L.P. Zhu, Solid State Commun. 142 (2007) 425–428.
3. S. Chuangchote, T. Sagawa and S. Yoshikawaa, Appl. Phys. Lett. 93 (2008) 033310.
4. T. Oekermann, T. Yoshida, C. Boeckler, J. Caro and H. Minoura, J. Phys. Chem. B 109 (2005) 12560-12566.
5. J. Jinmyoung, L. Dongkyu, Y. Myungsun and J. Sangmin, Sens. Actuators, B 138 (2009) 485-490.
6. H.Y. Yang, S.F. Yu, S.P. Lau, X. Zhang, D.D. Sun, and G. Ju, Small 5 (2009) 2260–2264.
7. J. Liu, Z. Guo, F. Meng, Y. Jia, T. Luo, M. Li and J. Liu, Cryst. Growth Des. 9 (2009) 1716-1722.
8. J. Ji, P. Zeng, S. Ji, W. Yang, H. Liu, Y. Li, Catal. Today, 158 (2010)305-309.
9. Y. Chen, H. Chen, D. Zeng, Y. Tian, F. Chen, J. Feng, and J. Shi, ACS Nano 4 (2010) 6001–6013.
10. S.-W. Choi, J.Y. Park, S.S. Kim, Nanotechnology 20 (2009) 465603.
11. Z.L. Wang, ACS Nano 2 (2008) 1987–1992.
12. L.S. Wang, M.W. Xiao, X.J. Huang and Y.D. Wu, J. Hazard. Mater. 161 (2009) 49-54.
13. N. Wang, X. Li, Y. Wang, Y. Hou, X. Zou and G. Chen, Mater. Lett. 62 (2008) 3691–3693.
14. P. Charoensirithavorn, Y. Ogomi, T. Sagawa, S. Hayase and S. Yoshikawa, J. Cryst. Growth 311 (2009) 757–759.

15. S.H. Kang, J.-Y. Kim, Y. Kim, H. S. Kim and Y.-E. Sung, J. Phys. Chem. C 111 (2007) 9614-9623.
16. N. Obradović, N. Labus, T. Srećković, D. Minić, M. M. Ristić, Sci. Sintering 37 (2005) 123-129.
17. Y. Zeng, T. Zhang, L. Wang, M. Kang, H. Fan, R. Wang, Y. He, Sens. Actuators, B 140 (2009) 73–78.
18. H. Wang, Z. Wu, Y. Liu and Z. Sheng, J. Mol. Catal. A: Chem. 287 (2008) 176-181.
19. G.B, Song, J.K. Liang, F.S. Liu, T.J. Peng and G.H. Rao, Thin Solid Films, 491 (2005) 110-116.
20. L.G. Devi, N. Kottam and S.G. Kumar, J. Phys. Chem. C 113 (2009) 15593-15601.
21. G. Li and K. A. Gray, Chem. Mater. 19 (2007) 1143-1146.
22. T. Miyagi, M. Kamei, T. Mitsuhashi, T. Ishigaki and A. Yamazaki, Chem. Phys. Lett. 390 (2004) 399-402.
23. M.C. Carotta, A. Cervi, V. di Natale, S. Gherardi, A. Giberti, V. Guidi, D. Puzzovio, B. Vendemiati, G. Martinelli, M. Sacerdoti, D. Calestani, A. Zappettini, M. Zha and L. Zanotti, Sens. Actuators, B 137 (2009) 164–169.
24. Y. Zhang, J. Xu, Q. Xiang, H. Li, Q. Pan and P. Xu, J. Phys. Chem. C 113 (2009) 3430–3435.
25. E. Oh, H-Y. Choi, S-H. Jung, S. Cho, J.C. Kim, K-H. Lee, S-W. Kang, J. Kim, J-Y.Yun and S-H. Jeong, Sens. Actuators, A 141 (2009) 239-243.
26. Y. Feng, S. Wang, B. Feng, R. Wang, Y. He and T. Zhang, Sens. Actuators, A 152 (2009) 104-109.
27. F. Fang, J. Futter, A. Markwitz and J. Kennedy, Nanotechnology 20 (2009) 245502-245508.
28. J.Y. Park, S-W. Choi, J-W. Lee, C. Lee and S.S. Kim, J. Am. Ceram. Soc. 92 (2009) 2551-2554.
29. W. Wang, H. Huang, Z. Li, H. Zhang, Y. Wang, W. Zheng and C. Wang, J. Am. Ceram. Soc. 91 (2008) 3817–3819.
30. E. Formo, E. Lee, D. Campbell and Y. Xia, Nano Lett. 8 (2008) 668-672.
31. N. Wang, C. Sun, Y. Zhao, S. Zhou, P. Chena and L. Jiang, J. Mater. Chem. 18 (2008) 3909–3911.
32. W. Sigmund, J. Yuh, H. Park, V. Maneeratana, G. Pyrgiotakis, T. J. Daga and J.C. Nino, J. Am. Ceram. Soc. 89 (2006) 395–407.

33. G. Malandrino, M. Blandino, L.M.S. Perdicaro, I. L. Fragala, P. Rossi, and P. Dapporto, Inorg. Chem. 44 (2005) 9684-9689.
34. B. Erdem, R.A. Hunsicker, G.W. Simmons, E.D. Sudol, V.L. Dimonie and M.S. El-Aasser, Langmuir 17 (2001) 2664-2669.
35. C.-T. Wang and J.-C. Lin, Appl. Surf. Sci. 254 (2008) 4500–4507.
36. J-C. Dupin, D. Gonbeau, P. Vinatier and A. Levasseur, Phys. Chem. Chem. Phys. 2 (2000) 1319-1324.
37. K. Kotsis and V. Staemmler, Phys. Chem. Chem. Phys. 8 (2006) 1490–1498.
38. D. Barreca, E. Comini, A.P. Ferrucci, A. Gasparotto, C. Maccato, C. Maragno, G. Sberveglieri and E. Tondello, Chem. Mater. 19 (2007) 5642-5649.
39. J. Zhao, C. Jia, H. Duan, H. Li and E. Xie, J. Alloys Compd. 461 (2008) 447–450.
40. M. Foley, C. Ton-That and M.R. Phillips, Appl. Phys. Lett. 93 (2008) 243104.
41. R.C. Wang, C.P. Liu and J. L. Huang, Appl. Phys. Lett, 86 (2005) 251104.
42. W. Lehmann, J. Electrochem. Soc. 115 (1968) 538-540.
43. K. Vanheusden, W. L. Warren, C.H. Seager, D.R. Tallant, J.A. Voigt and B.E. Gnade, J. Appl. Phys. 79 (1996) 7983-7990.
44. K. Vanheusden, W.L. Warren, C.H. Seager, D.R. Tallant, J. Caruso, M.J. Hampden-Smith and T. T. Kodas, Mater. Res. Soc. Symp. Proc. 424 (1997) 433.
45. K. Vanheusden, C.H. Seager, W.L. Warren, D.R. Tallant and J. A. Voigt, Appl. Phys. Lett. 68 (1996) 403-405.
46. A. van Dijken, J. Makkinje and A. Meijerink, J. Lumin. 92 (2001) 323–328.
47. A. van Dijken, E.A. Meulenkamp, D. Vanmaekelbergh and A. Meijerink, J. Phys. Chem. B 104 (2000) 1715-1723.
48. D. Banerjee, J.Y. Lao, D.Z. Wang, J.Y. Huang, D. Steeves, B. Kimball and Z.F. Ren, Nanotechnology 15 (2004) 404–409.
49. A.L. Pan, R.B. Liu, S.Q. Wang, Z.Y. Wu, L. Cao, S.S. Xie and B.S. Zou, J. Cryst. Growth 282 (2005) 125-130.
50. M.H. Huang, Y.Y. Wu, N.T. Feick, E. Weber and P.D. Yang, Adv. Mater. 13 (2001) 113-116.
51. B.D. Yao, Y.F. Chan and N. Wang, Appl. Phys. Lett. 2002, 81 ,757-759.

9. Concluding remarks

The controlled synthesis of nanostructured materials with synthetically tuned structure, size, and morphology represents a significant advance towards the understanding of the fundamental physics and chemistry of nanoscale materials as well as practical applications.

ZnO nanostructures have provided significant insight into the world of nanoscience and nanotechnology. In particular, one-dimensional ZnO nanostructures have great potential applications in many advanced nano-technological fields and thus it is very important to realize the controllable growth of one-dimensional ZnO nanostructures and investigate their properties. More specifically, the nanoscale science and engineering have found great promise in the fabrication of novel nano-biosensors with faster response and higher sensitivity than of planar sensor configurations. Therefore, one of this thesis aim is devoted to synthesis and characterization of ZnO nanostructures for the detection of chemical/biological species.

Specially nanowires/nanorods and due to their small dimensions combined with dramatically increased contact surface and strong binding with biological and chemical reagents will have important applications in biological and biochemical research. ZnO nanostructures have unique advantages including high surface to volume ratio, nontoxicity, chemical stability and more specifically, due to their low solubility at biological pH-values represent a valid example of biocompatible inorganic surface.

The main points of this thesis are not only to successfully realize the controllable growth of ZnO nanorods, nanoplatforms and TiO_2/ZnO heterostructures, but also investigate the structure, optical properties and sensing properties by means of scanning electron microscope (SEM), transmission electron microscope (TEM), photoluminescence (PL), X-ray photoelectron spectroscopy (XPS), X-ray Diffraction (XRD), Atomic Force Microscopy (AFM) and confocal microscopy.

Depending on the growth strategy chosen, i.e. Metal-Organic Chemical Vapor Deposition, Chemical bath deposition or hybrid integrated approaches with Nanosphere Colloidal Lithography and Electrospinning, nanostructured films, nanorods, nanowires, patterned ordered arrays and hierarchical nanostructures have been grown on various substrates including Si (100), glass and quartz substrates. It is demonstrated that rational tailoring of deposition procedure may lead to optimal growth and crystallinity.

It is established that the growth of ZnO nanostructures can be controlled by various parameters including time and temperature. It is shown that the growth temperature, herein ranging from 70 °C to 700 °C according to the chosen synthetic strategy, is crucial to control the ZnO nanostructure crystallinity and morphology. MOCVD growth at temperatures above 600 °C leads to the formation of short nanorods. Metal-organic silver catalyst has been proven effective to promote a 30-fold enhancement of growth rate at higher temperature (from nanostructured film to nanobundles) and a more limited growth at temperature $\leq$ 400 °C. The use of mild deposition conditions is indicated for an effective integration with colloidal lithography to obtain ZnO/SiO_2 nanoplatforms. However, this strategy results in complex procedure with many parameters to control (catalyst concentration, annealing condition, catalyst deposition strategy and ZnO growth process parameters) in order to obtain uniform patterned array. Therefore, catalyst-free low temperature (300 - 400 °C) MOCVD growth was developed.

Chemical bath deposition was chosen as an alternative approach to MOCVD technique allowing drastically decrease deposition temperature to 70 °C. In our study we found that seed layers deposited at 500 °C/30 min to be the best optimum growth conditions to promote nucleation and growth of ZnO nanostructures in solution with preffered c-axis orientation. To note, one of the major drawbacks is that the solution growth requires highly crystalline seeds often produces by vapor phase growth which prevents it to be used in flexible device technologies. Although it is demonstrated that highly oriented ordered ZnO nanorod arrays were fabricated on MOCVD-grown seed layers, the “solution” approach might benefit from use of seed layers obtained from solution approaches (i.e. Zn acetate hydrolysis and low temperature annealing) to promote the growth.

We achieved the fabrication of hybrid ZnO nanohole arrays combining CBD method with soft lithographic approach, where ZnO nanotubes and nanorods forming “nanobowl” were grown on the ZnO seed layer.

Combination of ZnO deposition approaches (MOCVD, CBD and hybrid MOCVD-CBD process) with colloidal lithography results in high surface areas hybrid nanoplatforms whose chemical and/or topographical patterning strongly affects the interaction with model biomolecules (proteins).

Part of the thesis, in fact relates specifically to biosensor technology and pertains more particularly to novel biosensors based on multifunctional ZnO nanorods for biological, biochemical and chemical applications. The presented approach appears to be very promising for biomolecular detection applications (based on fluorescence enhancement). Additionally, the morphological/chemical patterning of these ZnO–SiO_2 nanoplatforms can be easily tailored by sizing of the 2D vs. 3D patterning design, which in turn is accomplished by the fine tuning of the integrated colloidal lithography–chemical vapor deposition/chemical bath deposition processes.

Finally, it has been shown how the development of high surface area nanostructures would also benefit from merging electrospinning technique with commonly used ZnO growth strategies. Zn doped TiO_2 nanofibers shelled with ZnO hierarchical nanoarchitectures have been fabricated combining electrospinning of TiO_2 (anatase) nanofibers and metal-organic chemical vapor deposition (MOCVD) of ZnO. The proposed hybrid approach has proven suited for tailoring both the morphology of the ZnO external shell as well as the crystal structure of the d:TiO_2 core.

During the core-shell d:TiO_2–ZnO nanofibers fabrication, the presence of Zn dopant promotes the anatase to rutile phase transformation. The relative anatase/rutile ratio depends upon Zn content inside the anatase nanofibers. The structural characterization shows in addition to the presence of anatase, rutile and ZnO features, peaks arising from a TiO_2-ZnO phase (ecandrewsite) and Zn_2TiO_4, thus resulting in a nanocomposite architecture. These hierarchical nanoarchitectures exhibit a marked CL phenomenon of UV and visible emission. The obtained results are, thus, encouraging to propose the present approach as effective strategy to fabricate multiphase core-shell TiO_2-ZnO nanofibers that may represent promising materials for sensing applications.

To conclude, understanding of physical and chemical mechanisms of the growth will benefit the development of multifunctional material. Furthermore, there is much more to understand regarding ZnO-protein interaction, such as adsorption mechanism, orientation of the protein on the surface, use of other bio-analyte systems and integration challenges into commercial devices. However, despite the remaining questions, ZnO nanostructures due to its ease of fabrication in various shapes, reduced dimensionality, high aspect ratio, chemical stability and biocompatibility can become an essential component in commercial device applications, especially as sensing material for biological and chemical sensing devices.

Acknowledgements

I would like to express my gratitude to all those who gave me the possibility to complete this thesis. First of all, I would like to thank my supervisor Dr. M. E. Fragalà to whom I owe considerable gratitude for her constant patience and abundant assistance, and whose guidance, help and encouragement helped me in all the time of the research and writing up this thesis.

I count myself very lucky to have met and worked with so many incredible people in my research group, especially Prof. Graziella Malandrino and Prof. Guglielmo Condorelli. I would also like to thank Maria Rita Catalano and Cristina Tudisco for providing a wonderful working environment and solving many difficult equations. I thank my office mate Emanuele Smecca for his assistance and Dr. Alessandro Motta and Dr. Fabio Lupo for their help with X-ray photoelectron spectroscopy analysis and interesting discussions.

I would like to express my appreciation to Dr. Cristina Satriano for providing templates patterned via nanosphere colloidal lithography, and confocal microscopy and fluorescence recovery after photobleaching study of protein-ZnO interactions, Prof. Riccardo Reitano for photoluminescence analysis, Dr. Raffaela Lo Nigro for TEM measurements.

I would also like to thank Dr. Ilaria Cacciotti for her assistance with electrospinning technique and fabrication of titanium dioxide nanofibers.

I would like to thank the Head of the research group Prof. I.L. Fragalà for taking a chance on me as a student, for providing me the opportunity, means, space, direction, and encouragement to do my work, and helping me to achieve my personal and professional goals.

With regards to Scuola Superiore di Catania, I would like to thank Dr. B. Immè and Dr. M. Sanfilippo for their assistance without whose my stay here certainly would have been very different.

Finally, I would like to thank my boyfriend Giovanni and my family for their love, encouragement, dedication, and support.